	ESA Climate Change Initiative (CCI)		Page 1
	Climate Assessment Report (CAR)		
	for the Essential Climate Variable (ECV) Greenhouse Gases (GHG)		Version 4 (final)
			28 March 2017

ESA Climate Change Initiative (CCI)

Climate Assessment Report (CAR)

for Climate Research Data Package No. 4 (CRDP#4)

of the Essential Climate Variable (ECV)

Greenhouse Gases (GHG)

Frédéric Chevallier^a, Peter Bergamaschi^b, Liang Feng^c, Sander Houweling^d,
Thomas Kaminski^e, Wolfgang Knorr^f, Julia Marshall^g, Paul I. Palmer^c, S.
Pandey^d, Maximilian Reuter^h, Marko Scholze^f and Michael Voßbeck^e

^a Laboratoire des Sciences du Climat et de l'Environnement (LSCE), Gif-sur-Yvette, France

^b European Commission Joint Research Centre (EC-JRC), Air and Climate Unit, Ispra, Italy

^c University of Edinburgh, Edinburgh, United Kingdom


^d SRON Netherlands Institute for Space Research, Utrecht, Netherlands

^e The Inversion Lab, Hamburg, Germany

^f Lund University, Lund, Sweden

^g Max-Planck-Institute for Biogeochemistry (MPI-BGC), Jena, Germany

^h Institute of Environmental Physics, University of Bremen, Germany

	ESA Climate Change Initiative (CCI) Climate Assessment Report (CAR) for the Essential Climate Variable (ECV) Greenhouse Gases (GHG)	Page 2
		Version 4 (final)
		28 March 2017

Change log:

Version Nr.	Date	Status	Reason for change
Version 4, draft 1	17 February 2017	Version circulated internally before ARM3	Contributions from LSCE, iLab, SRON, MPI, and JRC integrated
Version 4, final	28 March 2017	Final version	Contribution from UoE and IUP added, and minor corrections to the others

This document should be cited as:

Chevallier, F., P. Bergamaschi, D. Brunner, L. Feng, S. Houweling, T. Kaminski, W. Knorr, J. Marshall, P. I. Palmer, S. Pandey, M. Reuter, M. Scholze, and M. Voßbeck, Climate Assessment Report for the GHG-CCI project of ESA's Climate Change Initiative, pp. 96, version 4, 28 March 2017, 2017.




	ESA Climate Change Initiative (CCI)	Page 3
	Climate Assessment Report (CAR)	
	for the Essential Climate Variable (ECV) Greenhouse Gases (GHG)	Version 4 (final)
		28 March 2017

Table of content

1. Executive summary	5
2. User related aspects discussed in the peer-reviewed literature	10
3. Assessment of satellite-derived XCO₂ ECA products	14
3.1. Introduction	14
3.2. Comparisons with model simulations	14
3.2.1. Method	14
3.2.2. Results.....	15
3.2.3. Conclusions	18
3.3. Inversion experiments with the LSCE system	18
3.3.1. Method	18
3.3.2. Global annual atmospheric growth rates	19
3.3.3. Maps of annual budgets.....	20
3.3.4. Seasonal cycles.....	21
3.3.5. Annual regional budgets	23
3.3.6. Conclusions	26
3.4. Inversion experiments with the Jena system	26
3.4.1. Method	26
3.4.2. Results.....	27
3.4.2.1. Global annual growth rate.....	27
3.4.2.2. Pixel-based total annual fluxes.....	29
3.4.2.3. Seasonal cycle on a regional scale	32
3.4.2.4. Regional annual budgets	35
3.4.2.4. Conclusions	36
3.5. Inversion experiments with the SRON system	36
3.5.1. Method	36
3.5.2. Global annual growth rate	38
3.5.3. Maps of annual budgets.....	39
3.5.4. Seasonal cycles.....	40
3.5.5. Annual regional budgets	42
3.5.6. Inter Annual Variability	43

	ESA Climate Change Initiative (CCI)		Page 4
	Climate Assessment Report (CAR)		
	for the Essential Climate Variable (ECV) Greenhouse Gases (GHG)		Version 4 (final)
			28 March 2017

3.5.7.	Conclusions	44
3.6.	Inversion experiments with the IUP system.....	45
3.6.1.	The regional flux inversion system used by IUP	45
3.6.2.	European fluxes derived from CRDP#4 data sets.....	46
3.6.3.	Conclusions	48
3.7.	Assimilation of XCO ₂ into a terrestrial vegetation model by iLab.....	48
3.7.1.	Introduction	48
3.7.2.	Method	49
3.7.3.	Preparation of observational data sets and setup.....	50
3.7.4.	Evaluation	51
3.7.5.	Conclusions	60
4.	Assessment of satellite-derived XCH ₄ ECA data products	60
4.1.	Introduction	60
4.2.	Assessment of XCH ₄ ECA products using the JRC inverse modelling system	61
4.2.1.	Method	61
4.2.2.	Comparison of CRDP#4 XCH ₄ products with atmospheric inversions based on surface observations.....	62
4.2.3.	CH ₄ flux inversions: assimilated XCH ₄	63
4.2.4.	CH ₄ flux inversions: derived CH ₄ fluxes.....	64
4.2.5.	Conclusions	75
4.3.	CH ₄ fluxes inferred from GOSAT proxy XCH ₄ :XCO ₂ retrievals with the UoE system.....	76
4.3.1.	Method	76
4.3.2.	Results.....	77
4.3.2.1.	Annual flux maps.....	77
4.3.2.2.	Regional annual emissions	79
4.3.3.	Conclusions	82
	Acknowledgements.....	83
	References	83

	ESA Climate Change Initiative (CCI) Climate Assessment Report (CAR) for the Essential Climate Variable (ECV) Greenhouse Gases (GHG)	Page 5
		Version 4 (final)
		28 March 2017

1. Executive summary

This report describes the **assessment of the Essential Climate Variable core products of the fourth release of the GHG-CCI Climate Research Data Package** (CRDP#4, http://www.esa-ghg-cci.org/sites/default/files/documents/public/documents/GHG-CCI_DATA.html) by the Climate Research Group (CRG) of GHG-CCI (Buchwitz et al. 2015, 2017b). These products are CO₂ and CH₄ column retrievals (XCO₂ and XCH₄) from current (TANSO) and past (SCIAMACHY) satellite instruments made by three different groups (University of Bremen, University of Leicester and SRON/KIT/JPL). Climate researchers may find interest in these products for various reasons like evaluating climate models, estimating the uncertain parameters of these climate models, studying the variability of CO₂ and CH₄ in the atmosphere, studying wildfire or fossil fuel emission plumes, or quantifying the surface fluxes of these gases.

By producing retrievals of the CO₂ and CH₄ columns for two satellites, CRDP has given a **unique**, though heterogeneous, **climate record from space covering now more than ten years** of the two major greenhouse gases of anthropogenic origin. **This length opens the possibility to characterize emission trends, as was already demonstrated by a series of CRDP-based studies for CH₄** (Bergamaschi et al. 2013) **and for CO₂** (Ross et al. 2013, Schneising et al. 2013a, 2013b, Reuter et al. 2014b, Detmers et al. 2015).

The pioneering character of these new climate records is deliberately acknowledged through the use of an ensemble of retrieval products covering several sensors and multiple retrieval algorithms. **This ensemble approach allows a more comprehensive assessment of the product uncertainty than just the typical uncertainty characterisation of each product through internal uncertainty propagation.** Reuter et al. (2013, 2014a) well illustrated this capability.

CRDP, together with satellite retrievals made outside Europe, has already served to **quantify regional carbon budgets** (e.g., Basu et al. 2013, Bergamaschi et al. 2013, Fraser et al. 2013, Monteil et al. 2013, Cressot et al. 2013) and more specifically (for CO₂) Canada and Siberian forests (Schneising et al. 2011), Eurasia (Guerlet et al. 2013a), Tropical Asia (Basu et al. 2014), Amazonia (Parazoo et al. 2013) and Europe (Reuter et al. 2014a). However, for CO₂, there remain considerable discrepancies with bottom up estimates or flux inversions based on atmospheric in-situ observations (Chevallier et al. 2014a, Feng et al. 2016a, Reuter et al. 2016c). These discrepancies were also highlighted in Versions 1, 2 and 3 of the CAR (Chevallier et al. 2013, 2015, 2016). For CH₄ it has been clearly demonstrated that the SCIAMACHY retrievals and the GOSAT retrievals provide important information on regional methane emissions (e.g., Bergamaschi et al. 2013, Fraser et al. 2013, Alexe et al. 2015).

Each application of the CRDP has specific user requirements and it is not possible to exhaustively cover them in the CRG. Instead, the CRG has focussed on source-sink inversion from several viewpoints.

For CO₂, the starting point of this report is the comparison between the SCIAMACHY and GOSAT CRDP products with the independent CAMS v15r4 transport model simulation (with surface fluxes inferred through inversion of high precision measurements of atmospheric CO₂ in situ samples). The satellite retrievals fit the independent CAMS simulation over land within 1.6-3.2 ppm RMS over land and 1.2-2.1 ppm RMS over ocean (GOSAT products only). The overall quality of the XCO₂_GOS_OCFP retrievals over the oceans seems to have degraded compared to CRDP#3, likely due to the absence of a bias-correction or to a loose quality control for this version of the product. XCO₂_GOS_OCFP consequently overestimates its precision skill over ocean (i.e. report too large uncertainty values), while the other algorithms and XCO₂_GOS_OCFP over land report adequate values. Additionally, limited correlations of the retrieval errors are seen both in space and in time for each product: they reflect other error sources than just the instrument, like possible errors in the radiative transfer models; they complicate the interpretation of the space-time variations of the retrievals.

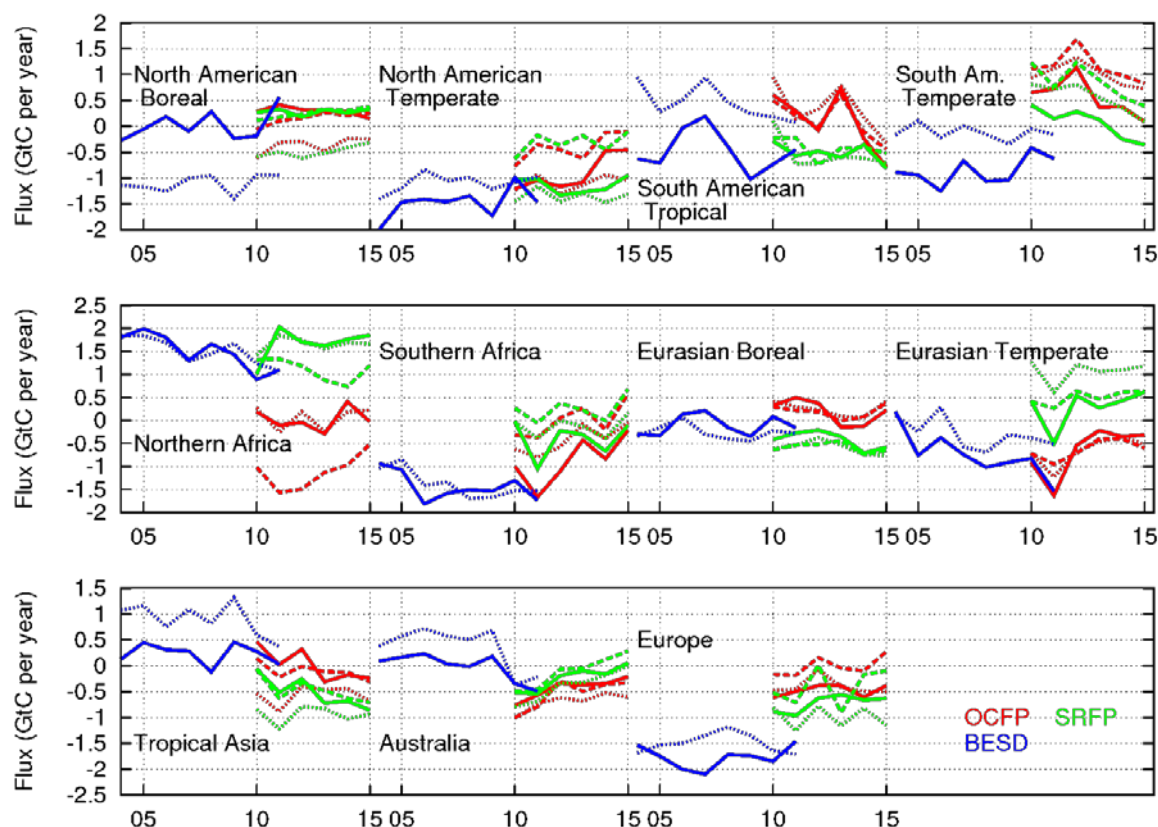


Figure 1. Inferred natural CO₂ annual flux (without fossil fuel emissions) from XCO₂_SCI_BESD, XCO₂_GOS_OCFP and XCO₂_GOS_SRFP averaged over the TransCom3 land regions. Dotted, dashed and continuous lines correspond to the MPI-BGC, the SRON and the LSCE inversion system, respectively. In the sign convention, positive fluxes correspond to a net carbon source into the atmosphere.

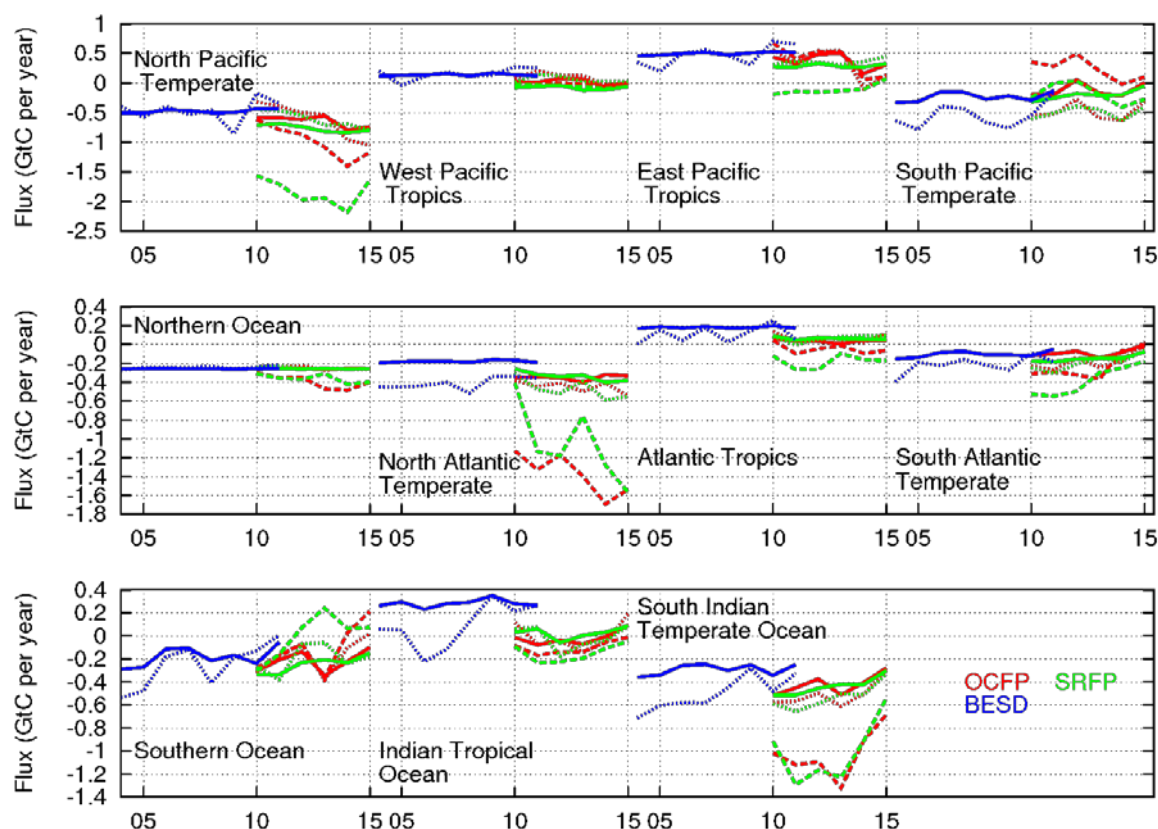



Figure 2. Same as Figure 1, but for the TransCom3 ocean regions.

XCO2_SCI_BESD, XCO2_GOS_OCFP and XCO2_GOS_SRFP are tested within the global atmospheric inversion systems of LSCE, MPI-BGC and SRON. The result spread from one system to the next is quite large, over land as over ocean (Figure 1 and Figure 2), which illustrates the fact that **inversion results depend not only on retrieval errors but also on errors of the underlying transport and uncertainty models**. For instance the lower quality of the first three months of XCO2_SCI_BESD corrupts the whole 9-year inversion when using the LSCE systems, but apparently not when using the MPI-BGC system. However, increasing the spatial resolution in the MPI-BGC transport model leads to negligible impact for the GOSAT inversions, which suggests that changing to higher spatial resolutions will not be a panacea leading to convergence between the surface- and satellite-derived fluxes. For a given system, large **differences are still seen between some CO₂ regional budgets inferred through transport inversion and (imperfect) current knowledge** (as presented for instance in the Regional Carbon Cycle Assessment and Processes of the Global Carbon Project, www.biogeosciences.net/special_issue107.html). However, compared to the CRDP#3 version of these retrieval products, **there is no region any more where satellite-based inversions are all inconsistent with current knowledge** (Figure 1 and Figure 2). For instance, all GOSAT inversions now infer a sink in Europe which is less than 1 GtC/yr and, for most of them, is even smaller than the corresponding surface-based inversion (Figure 1). Only the XCO2_SCI_BESD inversions show a significantly larger sink. Some of the GOSAT inversions now also infer a neutral budget in Northern

	ESA Climate Change Initiative (CCI)	Page 8
	Climate Assessment Report (CAR)	
	for the Essential Climate Variable (ECV) Greenhouse Gases (GHG)	Version 4 (final)
		28 March 2017


Africa. We also note some remarkable convergence of the results from the retrievals and from other data sources in some regions, most prominently in Australia. These results suggest that some of the regional signals of the retrievals are robust and reliable.

The reliability of global inversion results using the CRDP#4 data has increased and may allow scientifically-useful inversion results regionally, but still seems to be lower than with the surface air sample network overall, at least in terms of flux amplitude. It is therefore required to evaluate each new finding carefully, for instance by comparison with complementary data or with sensitivity studies. We also note that the above assessments are preliminary in the sense that posterior uncertainty analyses have not been completed yet.

Results from the IUP regional ensemble inversion comprising eleven years (2003-2013), three retrieval algorithms (XCO₂_SCI_BESD, XCO₂_GOS_SRFP and XCO₂_GOS_OCFP), two CO₂ prior flux types (CT2016, CAMS v15r4), and two meteorological data sources (NCEP, ERA Interim) suggest that the terrestrial European biosphere takes up $0.84 \pm 0.55 \text{ GtC/yr}$. Compared to the previous results of Reuter et al. (2014), the ensemble spread has increased which can in large parts be attributed to the considerable differences between CT2016 and CAMS v15r4 fluxes especially during the dormant season. Additionally to this, the inversion results seem to vary more from one algorithm to another which was not expected because the CRDP#4 validation activities and results from XCO₂_EMMA (Buchwitz et al., 2017a) suggest that all retrieval algorithms improved and somewhat converged.


A further CRG assessment activity, complementing the atmospheric inversions, is **the assimilation of XCO₂_SCI_BESD and XCO₂_EMMA from CRDP#4 into a global terrestrial biosphere model by iLab**, under the assumption of perfect terrestrial and transport models. It results in a dynamically consistent surface flux product. The most prominent feature in the posterior net flux is the tropical source of CO₂ inferred from both products. However, for XCO₂_EMMA this source is much more pronounced than for XCO₂_SCI_BESD, especially over South America with values of $300 \text{ gC/m}^2/\text{year}$ and higher. This high tropical source confirms the results of the intercomparison study of Houweling et al. (2015), which was based on transport inversions using GOSAT data. The CCDAS attributes the larger net flux to increased heterotrophic respiration. This CCDAS comprises a validation framework that compares the atmospheric carbon dioxide concentration observed at flask sampling sites against transport model simulations based on the posterior flux fields. For both BESD and EMMA this provides a reasonable overall agreement for the seven sites from the SIO network covering a latitudinal range from 82.5°N to the South Pole. Last, it is found that assumptions on XCO₂ uncertainty correlation have a considerable impact on the inferred flux fields ($\sim 60 \text{ gC/m}^2/\text{year}$), stressing the importance of documented uncertainty correlation in XCO₂ products.

For CH₄, we first compare the inversion results from the various CRDP#4 XCH₄ products, based on the JRC inversion system. Compared to CRDP#3, **the CH₄_SCI_IMAP product has been significantly improved** regarding the consistency of the time series, but the longitudinal average of these retrievals still show a likely effect of the instrument pixel degradation end of 2005. For CH₄_SCI_WFMD, the impact of the **pixel degradation** is even larger. Compared to the two SCIAMACHY products, the four GOSAT products have significantly better quality, with annual

	ESA Climate Change Initiative (CCI)		Page 9
	Climate Assessment Report (CAR)		
	for the Essential Climate Variable (ECV) Greenhouse Gases (GHG)		Version 4 (final)
			28 March 2017

standard deviations between retrievals and model simulations in the range of 12-16 ppb, while the annual standard deviations are in the range 30-50 ppb for CH₄_SCI_IMAP v7.2 and 27-80 ppb for CH₄_SCI_WFMD v4.0. **The four GOSAT XCH₄ products show an overall good consistency regarding their spatial XCH₄ patterns and the use of these four products in the TM5-4DVAR inverse modelling system results in qualitatively similar spatial distributions of the posteriori CH₄ fluxes (average 2010-2015). There remains however quantitative differences in the derived regional fluxes which need to be further analyzed. An important issue remains also the bias correction, which is still required for the simultaneous assimilation of the satellite retrievals and the NOAA surface observations. Our analysis suggests that the calculated bias correction reflects a combination of model errors (especially the vertical CH₄ gradient in the stratosphere at mid to high latitudes) and remaining systematic errors in the XCH₄ retrievals. For CH₄_GOS_OCFP, we identified a significant time dependent bias, which is apparent (1) from the comparison with the surface observation based inversion, and (2) from the significant changes of the required bias correction over time, when inverting this product (together with the surface measurements). CH₄_GOS_SRFP shows overall good consistency with the two GOSAT proxy retrievals. Despite the lower number of valid pixels, the full physics retrievals are considered as very valuable because they are independent from CO₂ model fields.**

We then compare inversion results from GOSAT proxy XCH₄:XCO₂ retrievals, based on the UoE inversion system. **The in-situ and proxy ratio data all result in similar global annual CH₄ emission totals, but the ratio data have lower emissions from temperate regions and higher emissions from the tropics.** These results are broadly consistent with the results of CARv3, and also agree with the inversions that use full-physics or proxy XCH₄ retrievals. We also find that assimilating the XCH₄:XCO₂ proxy data leads to larger seasonal cycles over tropical regions. Broadly, the two proxy datasets are consistent but we find differences at their resulting seasonal cycles over some northern regions such as Temperate Northern America. The differences are caused by different observation coverage as a result of different data filtering applied by the retrieval teams. This is also reflected in the year-to-year variations over geographical regions but in general **the flux estimates inferred from the two GOSAT proxy datasets are more consistent with each other than the fluxes inferred from the in situ data.**


	ESA Climate Change Initiative (CCI)	Page 10
	Climate Assessment Report (CAR)	
	for the Essential Climate Variable (ECV) Greenhouse Gases (GHG)	Version 4 (final)
		28 March 2017

2. User related aspects discussed in the peer-reviewed literature

The GHG-CCI project primarily aims at bringing new knowledge about the sources and sinks of CO₂ and CH₄ based on satellite-derived data products. Since the start of Phase 1 of this project, this aspect has been addressed in a series of publications, which are shortly summarised in the following. They usefully provide the background for the new studies that have been performed specifically for this report and that will be described next.

We start with the publications related to natural CO₂ fluxes.

- Using global GOSAT XCO₂ retrievals, Basu et al. (2013) presented first global CO₂ surface flux inverse modelling results for various regions. Their analysis suggested a reduced global land sink and a shift of the carbon uptake from the tropics to the extra-tropics. In particular, their results suggested that Europe is a stronger carbon sink than expected, but this feature was not further discussed in this paper.
- Chevallier et al. (2014a) analysed an ensemble of global inversion results assimilating two GOSAT XCO₂ retrieval products. They found hemispheric and regional differences in posterior flux estimates that are beyond 1 sigma uncertainties. They too found a significantly larger European carbon sink or a larger North African emission than expected. They concluded to the existence of significant flaws in all main components of the inversions: the transport model, the prior error statistics and the retrievals.
- Houweling et al. (2015) presented the outcome of a large inverse modelling intercomparison experiment on the use of GOSAT retrievals. The ensemble of results confirmed the large latitudinal shift in carbon uptake, but they showed that the reduced gradient degrades the agreement with background aircraft and surface measurements.
- Reuter et al. (2014a) investigated the European carbon sink further with another ensemble of GOSAT XCO₂ products, a SCIAMACHY XCO₂ product and a new inversion method which is less sensitive to some of the issues discussed in Chevallier et al. (2014a). Reuter et al. (2014a) only used satellite XCO₂ retrievals over Europe to rule out that non-European satellite data adversely influence the European results and they also only used short-term (days) transport modelling to avoid long-range transport errors. Based on an extensive analysis they concluded: "We show that the satellite-derived European terrestrial carbon sink is indeed much larger (1.02 ± 0.30 GtC/year in 2010) than previously expected". The value they derived is significantly larger compared to bottom-up estimates (not based on atmospheric measurements) of 0.235 ± 0.05 GtC/year for 2001-2004 (Schulze et al, 2009).
- The findings of Reuter et al. (2014a) stimulated additional research (Feng et al. 2016a, Reuter et al. 2016c).
- Detmers et al. (2015) analyzed GOSAT XCO₂ retrievals to detect and quantify anomalously large carbon uptake in Australia during a strong La Niña episode.
- For flux inversions not only the retrieved greenhouse gas values are relevant but also their error statistics, in particular the reported uncertainties. Chevallier and O'Dell (2013) analyzed this aspect in the context of CO₂ flux inversions using GOSAT XCO₂ retrievals. For CH₄, Cressot et al. (2013, 2016) studied the uncertainty of flux inversions assimilating SCIAMACHY, GOSAT or IASI XCH₄ retrievals.
- Focussing on Canadian and Siberian boreal forests, Schneising et al. (2011) computed longitudinal XCO₂ gradients from SCIAMACHY XCO₂ retrievals during the vegetation growing season over Canadian and Siberian boreal forests and compared the gradients with outputs from NOAA's CO₂ assimilation system CarbonTracker (Peters et al. 2007). They found good agreement for the total boreal region and for inter-annual variations. For the individual regions, however, they found


	ESA Climate Change Initiative (CCI)	Page 11
	Climate Assessment Report (CAR)	
	for the Essential Climate Variable (ECV) Greenhouse Gases (GHG)	Version 4 (final)
		28 March 2017

systematic differences suggesting a stronger Canadian boreal forest growing season CO₂ uptake and a weaker Siberian forest uptake compared to CarbonTracker.

- Focussing on hemispheric data and on carbon-climate feedbacks, Schneising et al. (2014a) used SCIAMACHY XCO₂ to study aspects related to the terrestrial carbon sink by looking at co-variations of XCO₂ growth rates and seasonal cycle amplitudes with near-surface temperature. They found XCO₂ growth rate changes of 1.25 ± 0.32 ppm/year/K (approximately 2.7 ± 0.7 GtC/year/K; indicating less carbon uptake in warmer years, i.e., a positive carbon-climate feedback) for the Northern Hemisphere in good agreement with CarbonTracker.
- Reuter et al. (2013) computed CO₂ seasonal cycle amplitudes using various satellite XCO₂ data products (using GHG-CCI products but also GOSAT XCO₂ products generated in Japan at NIES (Yoshida et al. 2013, Oshchepkov et al. 2013) and the NASA ACOS product (O'Dell et al. 2012) and compared the amplitudes with TCCON and CarbonTracker. They found that the satellite products typically agree well with TCCON but they found significantly lower amplitudes for CarbonTracker suggesting that CarbonTracker underestimates the CO₂ seasonal cycle amplitude by approx. 1.5 ± 0.5 ppm (see also Buchwitz et al., 2015, for a discussion of these findings).
- Lindquist et al. (2015) compared satellite XCO₂ retrievals, surface XCO₂ retrievals and atmospheric model simulations in terms of XCO₂ seasonal cycle. They found that the satellite retrieval algorithms performed qualitatively similarly but showed notable scatter at most validation sites. None of the tested algorithm clearly outperformed another. They showed that the XCO₂ seasonal cycle depends on longitude especially at the mid-latitudes, which was only partially shown by the models. They also found that model-to-model differences could be larger than GOSAT-to-model differences.
- Guerlet et al. (2013a) analyzed GOSAT XCO₂ retrievals focusing on the Northern Hemisphere. They identified a reduced carbon uptake in the summer of 2010 and found that this is most likely due to the heat wave in Eurasia driving biospheric fluxes and fire emissions. Using a joint inversion of GOSAT and surface data, they estimated an integrated biospheric and fire emission anomaly in April–September of 0.89 ± 0.20 PgC over Eurasia. They found that inversions of surface measurements alone fail to replicate the observed XCO₂ inter-annual variability (IAV) and underestimate emission IAV over Eurasia. They highlighted the value of GOSAT XCO₂ in constraining the response of land-atmosphere exchange of CO₂ to climate events.
- Basu et al. (2014) studied seasonal variation of CO₂ fluxes during 2009–2011 over Tropical Asia using GOSAT, CONTRAIL and IASI data. They found an enhanced source for 2010 and concluded that this is likely due to biosphere response to above-average temperatures in 2010 and unlikely due to biomass burning emissions.
- Parazoo et al. (2013) used GOSAT XCO₂ and solar induced chlorophyll fluorescence (SIF) retrievals to better understand the carbon balance of southern Amazonia.
- Ross et al. (2013) used GOSAT data to obtain information on wildfire CH₄:CO₂ emission ratios.

Despite the fact that none of the existing satellite missions has been optimized to obtain information on anthropogenic CO₂ emissions, this important aspect has been addressed in several recent publications using existing satellite XCO₂ products.

- Schneising et al. (2013) presented an assessment of the satellite data over major anthropogenic CO₂ source regions. They used a multi-year SCIAMACHY XCO₂ data set and compared the regional XCO₂ enhancements and trends with the emission inventory EDGAR v4.2 (Olivier et al. 2012). They found no significant trend for the Rhine-Ruhr area in central Europe and the US East Coast but a significant


	ESA Climate Change Initiative (CCI)	Page 12
	Climate Assessment Report (CAR)	
	for the Essential Climate Variable (ECV) Greenhouse Gases (GHG)	Version 4 (final)
		28 March 2017

increasing trend for the Yangtze River Delta in China of about $13 \pm 8\%$ /year, in agreement with EDGAR ($10 \pm 1\%$ /year).

- Reuter et al. (2014b) studied co-located SCIAMACHY XCO₂ and NO₂ retrievals over major anthropogenic source regions. For East Asia they found increasing emissions of NO_x (+5.8%/year) and CO₂ (+9.8%/year), i.e., decreasing emissions of NO_x relative to CO₂ indicating that the recently installed and renewed technology in East Asia, such as power plants and transportation, is cleaner in terms of NO_x emissions than the old infrastructure, and roughly matches relative emission levels in North America and Europe.

A series of studies also addressed methane emissions.

- SCIAMACHY data have already been extensively used to improve our knowledge on regional methane emissions prior to the start of the GHG-CCI project (e.g., Bergamaschi et al. 2009). A more recent research focus was to shed light on the unexpected renewed atmospheric methane increase during 2007 and later years using ground-based and satellite data (e.g., Rigby et al. 2008, Dlugokencky et al. 2009, Bergamaschi et al. 2009, 2013, Schneising et al. 2011, Frankenberg et al. 2011, Sussmann et al. 2012, Crevoisier et al. 2013). Based on an analysis of SCIAMACHY year 2003-2009 retrievals an increase of 7-9 ppb/year (0.4-0.5%/year) has been found with the largest increases in the tropics and northern mid latitudes (Schneising et al. 2011) but a particular region responsible for the increase has not been identified (Schneising et al. 2011; Frankenberg et al. 2011). Bergamaschi et al. (2013) used SCIAMACHY retrievals and NOAA surface data for 2003-2010 and inverse modelling in order to attribute the observed increase of atmospheric concentrations to changes in emissions. They concluded that most of this increase is due to emissions in the Tropics and the mid-latitudes of the northern hemisphere, while no significant trend was derived for Arctic latitudes. The increase is mainly attributed to anthropogenic sources, superimposed with significant inter-annual variations of emissions from wetlands and biomass burning.
- Methane emissions have also been obtained from GOSAT, as presented in a number of publications as shown in, e.g., Fraser et al. (2013, 2014), Monteil et al. (2013), Cressot et al. (2014), Alexe et al. (2015), Turner et al. (2015) and Pandey et al. (2016). Note that for these studies often CH₄ retrievals from several satellites have been used (as well as NOAA data), e.g., Monteil et al. (2013), and Alexe et al. (2015) used SCIAMACHY and GOSAT retrievals and Cressot et al. (2014, 2016) used GOSAT, SCIAMACHY and IASI. Alexe et al. (2015) showed that the different satellite products resulted in relatively consistent spatial flux adjustment patterns, particularly across equatorial Africa and North America. Over North America, the satellite inversions result in a significant redistribution of emissions from North-East to South-Central USA, most likely due to natural gas production facilities.
- Several publications focused on (relatively localized) methane sources in the United States: For example, Schneising et al. (2014b) analyzed SCIAMACHY data over major US “fracking” areas and quantified methane emissions and leakage rates. For two of the fastest growing production regions in the US, the Bakken and Eagle Ford formations, they estimated that emissions increased by 990 ± 650 ktCH₄/year and 530 ± 330 ktCH₄/year between the periods 2006–2008 and 2009–2011. Relative to the respective increases in oil and gas production, these emission estimates correspond to leakages of $10.1\% \pm 7.3\%$ and $9.1\% \pm 6.2\%$ in terms of energy content, calling immediate climate benefit into question and indicating that current inventories likely underestimate the fugitive emissions from Bakken and Eagle Ford. Others also used SCIAMACHY data over the US to identify and quantify localized anthropogenic methane emission sources (Kort et al. 2014, Wecht et al. 2014). Last, Turner et al. (2015) used GOSAT retrievals within a meso-scale inversion system for the US.

	ESA Climate Change Initiative (CCI)		Page 13
	Climate Assessment Report (CAR)		
	for the Essential Climate Variable (ECV) Greenhouse Gases (GHG)		Version 4 (final)
			28 March 2017

The SCIAMACHY XCH₄ retrievals have also been used to improve chemistry-climate models (Shindell et al. 2013, Hayman et al. 2014).

3. Assessment of satellite-derived XCO₂ ECA products

3.1. Introduction

The five ECV core algorithm products of the GHG-CCI Climate Research Data Package (CRDP#4, http://www.esa-ghg-cci.org/sites/default/files/documents/public/documents/GHG-CCI_DATA.html) are evaluated in the following. They are listed in Table 1 below. The official bias-corrected products have been processed by the three CRG inversion partners (LSCE, MPI-BGC and SRON), by IUP and by the CCDAS partner (iLab).


Product ID	Instrument	Algorithm	Data provider	Period available	Evaluators (sections)
XCO2_SCI_BESD	SCIAMACHY	BESD, v02.01.02	IUP, Univ. Bremen	01/2003-03/2012	LSCE (3.2, 3.3), MPI-BGC (3.4), IUP (3.6), iLab (3.7)
XCO2_SCI_WFMD	SCIAMACHY	WFMD, v4.0	IUP, Univ. Bremen	10/2002-04/2012	LSCE (3.2)
XCO2_GOS_OCFP	TANSO	UoL-FP, v7.0	University Leicester	04/2009-12/2015	LSCE (3.2, 3.3), MPI-BGC (3.4), SRON (3.5), IUP (3.6)
XCO2_GOS_SRF	TANSO	RemoteC, v2.3.8	SRON/KIT	04/2009-12/2015	LSCE (3.2, 3.3), MPI-BGC (3.4), SRON (3.5), IUP (3.6)
XCO2_EMMA	SCIA+TANSO	EMMA, v2.2c	IUP, Univ. Bremen	06/2009-05/2014	MPI-BGC (3.4), iLab (3.7)

Table 1. XCO₂ products evaluated in this report.

3.2. Comparisons with model simulations

3.2.1. Method

In this section, we compare XCO₂_SCI_BESD, XCO₂_GOS_OCFP and XCO₂_GOS_SRF with a forward simulation of the LMDZ transport model (Hourdin et al. 2006) using surface fluxes from a classical atmospheric inversion that assimilated surface air-sample measurements. The simulation accounts for the prior profiles and averaging kernels of each individual retrieval. Chevallier and O'Dell (2013) showed that the uncertainty of such simulated XCO₂ field is very small (standard deviation is less than 0.85 ppm) compared to XCO₂ retrieval errors from GOSAT, even over Tropical lands, so that the model-minus-retrieval departures are marginally larger than the retrieval errors. Computing the departures therefore allows evaluating the realism of the product retrieval errors that are an integral

	ESA Climate Change Initiative (CCI)	Page 15
	Climate Assessment Report (CAR)	
	for the Essential Climate Variable (ECV) Greenhouse Gases (GHG)	Version 4 (final)
		28 March 2017

part of the L2 retrieval process. We refer to Chevallier and O'Dell (2013) for more background about the underlying principles.

Our forward simulation comes from the CAMS CO₂ inversion product (version 15r4, <http://www.copernicus-atmosphere.eu/>), an earlier version of which was described by Chevallier et al. (2010a). It uses the LMDZ transport model with 39 vertical layers and a horizontal resolution of 3.75 longitude degrees by 1.9 latitude degrees.

3.2.2. Results

Multiyear-results are summarized in Figure 3. Distinction is made between the lands and the oceans north of 20°N (respectively referred to as LN20N and SN20N, in the following), the lands and the oceans south of 20°S (called LS20S and SS20N, respectively), the lands and the oceans between 20°S and 20°N (LTrop and STrop). Since we have no way to distinguish between random errors and systematic ones in the retrieval products and in the forward simulation, and following the usual practice (e.g., Desroziers et al. 2005), we use the root mean square (RMS) to characterize the statistics of the model-minus-observation departures, rather than the standard deviation.

The number of data feeding the statistics (the pink bars in Figure 3) varies for each product, depending on its instrument sounding density (more data from SCIAMACHY than from GOSAT) and on the input/output screening performed in the corresponding retrieval algorithm (no ocean data for SCIAMACHY). The RMS departures (the orange disks in Figure 3) are about 2.1 ppm for LN20N and LTrop for XCO₂_SCI_BESD and XCO₂_GOS_SRFP. They are smaller (~1.8 ppm) for XCO₂_GOS_OCFP and larger (~2.9 ppm) for XCO₂_SCI_WFMD. The two GOSAT-based products show smaller RMS for LS20S (~1.6 ppm) while XCO₂_SCIA_BESD is about 2 ppm there and XCO₂_SCI_WFMD about 2.4 ppm. Over the oceans, the statistics for XCO₂_GOS_SRFP are about 1.4 ppm, but are much worse for XCO₂_GOS_OCFP (it is about 2.1 ppm with a negligible bias). The misfits for the CRDP#3 version of XCO₂_GOS_OCFP were smaller (Chevallier et al. 2016), but the ocean (glint) retrievals of XCO₂_GOS_OCFP are bias-corrected in #3 but not in #4 (Hewson 2016, Somkuti 2017). Ocean glint retrievals of XCO₂_GOS_SRFP are bias-corrected. Also, there are many more glint data in XCO₂_GOS_OCFP than in XCO₂_GOS_SRFP, and in XCO₂_GOS_OCFP from CRDP#4 than from CRDP#3, which suggests that the quality control is not strict enough. The precision and bias of the CRDP#4 products have been assessed independently (Table 3.2.8.1 in Product Validation and Intercomparison Report, PVIR, version 5.0, Buchwitz et al. 2017a) based on TCCON measurements (Wunch et al. 2011). The scatter of the retrieval misfits to TCCON is overall similar to the scatter of the retrieval misfits to the model, but the relatively large errors of XCO₂_GOS_OCFP over the ocean is not seen when looking at the TCCON sites in PVIR. Note that the TCCON data are not independent from the retrievals since they serve to bias-correct them. In the study by Chevallier and O'Dell (2013), such model-data misfits were computed with the bias-corrected ACOS product of GOSAT (version 2.10, O'Dell et al. 2012) and a previous less accurate forward simulation of the LMDZ model. These authors showed better error statistics (the RMS are typically about 1.4 ppm) than those of Figure 3.

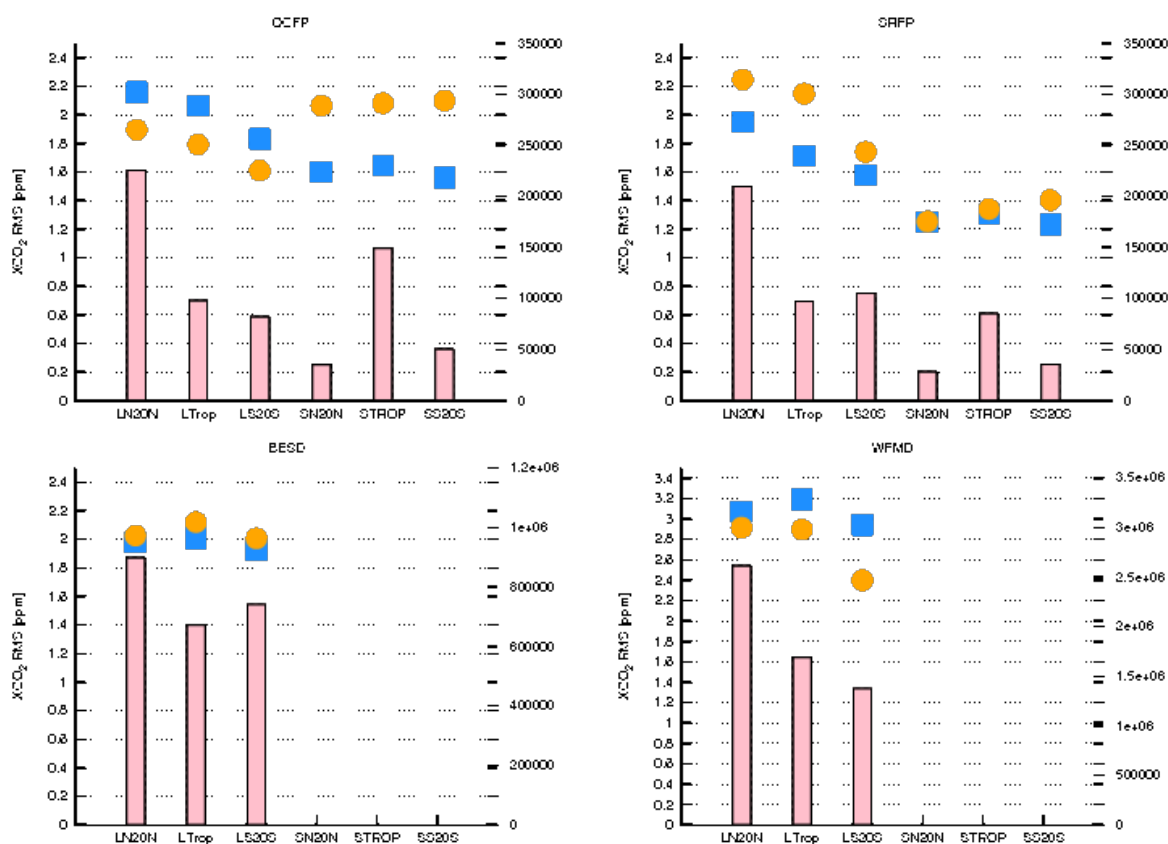


Figure 3. The orange disks show the Root Mean Squared values (RMS) of the misfits between the three CRDP#4 products and the reference CAMS simulation for the full period covered by each retrieval product. The blue squares represent the root mean square of the sum of the CAMS simulation error variances and of the retrieval error variances. The globe is divided in three latitude bands for land and ocean separately. The number of data included in the statistics is reported as vertical pink bars.

We now look at the retrieval error statistics provided by each product (the blue squares in Figure 3). In the study by Chevallier and O'Dell (2013), the model-data misfits with ACOS showed good consistency with the documented retrieval errors, to the point that the theoretical error reduction brought by the surface measurements on the simulation of the GOSAT total column measurements (15%) corresponded to the actual reduction seen over the mid-latitude and Tropical lands and over the Tropical oceans. The retrieval errors reported in the XCO₂_SCI_BESD, XCO₂_SCI_WFMD and XCO₂_GOS_SRFP products appear to be fairly estimated (the products may have actually be tuned for this; see, e.g., Somkuti 2017), consistent with the TCCON-based PVIR analysis (Buchwitz et al. 2017a, their Table 3.2.8.1). This is also the case for XCO₂_GOS_OCFP over land, but over the ocean this product is overconfident.

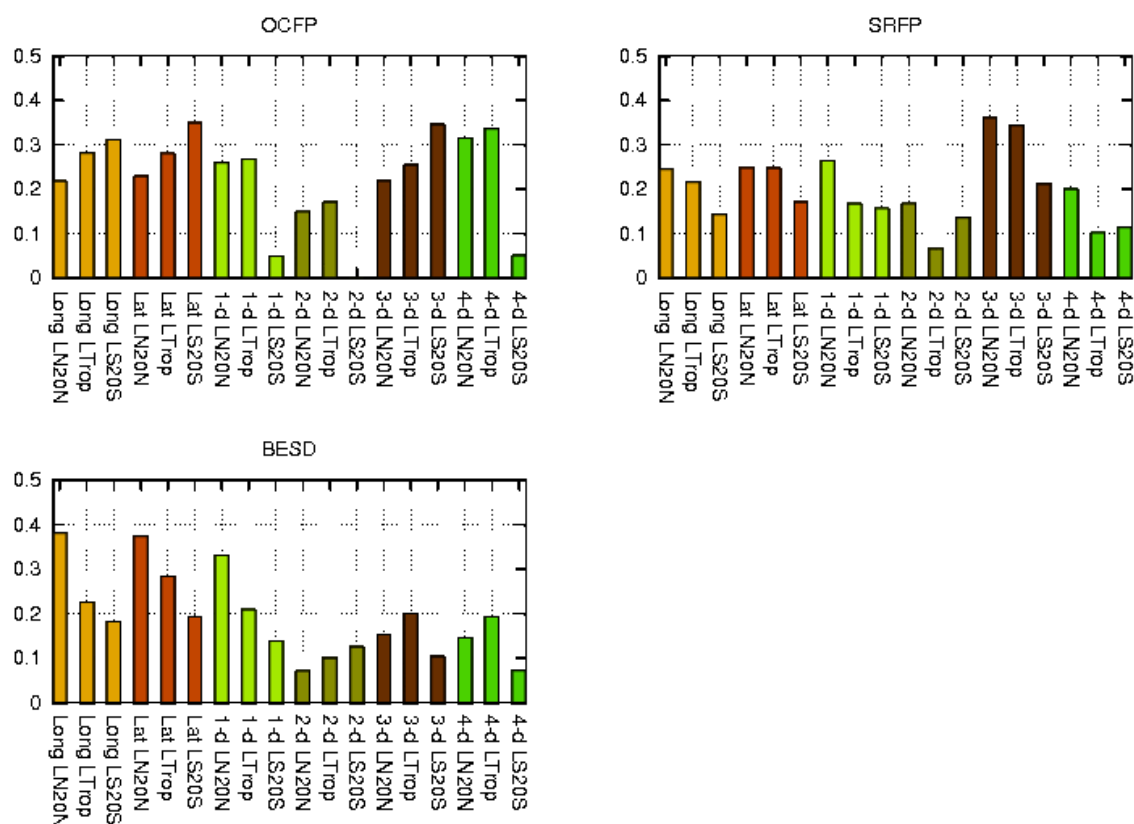



Figure 4. From left to right in each sub-figure, for May-June 2010 over land: correlations in the three latitude bands between pairs of model-data misfits taken at the same time at the same latitude and distant by one model grid point (Long), correlations between pairs of model-data misfits taken at the same time at the same longitude and distant by one model grid point (Lat), autocorrelations between the model-data misfits (lags between 1 and 4 days).

Finally, we look at the correlation of the misfits for XCO₂_GOS_OCFP, XCO₂_GOS_SRFP and XCO₂_SCI_BESD (XCO₂_SCI_WFMD is not studied here because of its large RMS misfits shown above). This correlation should be similar to the correlation of the retrieval errors, with only a marginal contribution from the model errors. The spatial correlations over land during May-June 2010 are illustrated in the 6 left-most columns of each panel of Figure 4. The correlations are computed for pairs of land data located at the same latitude or at the same longitude and distant by one model grid point ($3.75^{\circ} \times 1.9^{\circ}$). The spatial correlations are seen to be less than 0.4 for the three products. They are about the same along longitudes than along latitudes. For XCO₂_GOS_SRFP and XCO₂_SCI_BESD, they are mostly larger in LN20N than in LTrop and LS20S, but the situation is opposite for XCO₂_GOS_OCFP, likely related to the worse performance of this product over the ocean. The temporal correlations over land during May-June 2010 are shown in the 12 right-most columns of the same figure at four lags: 1, 2, 3 and 4 days. They are larger in the northern hemisphere and do not always decrease within the first few days, due to the specific orbit and swath of each instrument (for instance, the orbit pattern of GOSAT repeats every three days). XCO₂_SCI_BESD has the smallest temporal correlations (< 0.2).

	ESA Climate Change Initiative (CCI)	Page 18
	Climate Assessment Report (CAR)	
	for the Essential Climate Variable (ECV) Greenhouse Gases (GHG)	Version 4 (final)
		28 March 2017

These error correlations in space and time indicate some limited redundancy in the data that may slightly degrade the quality of flux inversions if not accounted for. Chevallier (2007) studied the impact of hypothetical observation error correlations of 0.5 in neighbouring observations. He showed very limited impact on the accuracy of the inferred fluxes when they were correctly taken into account, which is technically challenging for large-dimension inversion systems. When they were ignored, the uncertainty reduction on weekly fluxes was degraded by up to about 0.1 (unitless) over both land and ocean.

3.2.3. Conclusions

The retrievals fit the independent CAMS simulation over land within 1.6-3.2 ppm RMS over land and 1.2-2.1 ppm RMS over ocean (GOSAT products only). The quality of the XCO₂_GOS_OCFP retrievals over the oceans seems to have degraded compared to CRDP#3, likely due to the absence of a bias-correction or to a loose quality control for this version of the product. XCO₂_GOS_OCFP consequently overestimates its precision skill over ocean (i.e. report too large uncertainty values), while the other algorithms and XCO₂_GOS_OCFP over land report adequate values. Additionally, limited correlations of the retrieval errors are seen both in space and in time for each product.

3.3. Inversion experiments with the LSCE system

3.3.1. Method

In this section, we go one step further in the evaluation of XCO₂_SCI_BESD, XCO₂_GOS_OCFP and XCO₂_GOS_SRFP with the LSCE system by interpreting in terms of surface fluxes the model-data misfits shown in Section 3.2. The satellite data are assimilated alone, without combining them with other measurements, in order to focus on their own signals. We use the products candidly, i.e. without modifying the retrieval values and their associated uncertainty. However, if several retrievals of a same product and of a same orbit fall within the same model grid box, we inflate the variance of the retrieval errors by the number of concerned retrievals, in order to avoid likely local error correlations (at least from the transport model). As in the previous section, we use the retrieval averaging kernels and prior profiles when assimilating them.

The inferred fluxes from the three CRDP#4 products are compared to one benchmark inversion: the CAMS official inversion product v15r4 that exclusively assimilates about 130 sites of surface air sample measurements from the Global Atmosphere Watch programme.

The inversion system works at the grid-point weekly scale and generates a large volume of data. The present comparison focuses on a few key quantities: (i) the global annual growth rate that is well known from the NOAA marine surface data (Conway et al. 1994, <http://www.esrl.noaa.gov/gmd/ccgg/trends/global.html>), (ii) the grid-point annual-total fluxes, (iii) the flux seasonal cycle at regional scale, and (iv) the regional annual CO₂ budgets.



We use the full multi-year series of the three CRDP#4 products studied here, which is long enough to provide ample spin-up and spin-down periods. However, we only use XCO₂_SCI_BESD from April 2003 onwards because including the first three months of 2003 corrupts the whole inversion. The Product User Guide (Reuter 2016a) simply says that this early data “is less reliable”, but the deficiency is actually fatal for the LSCE inversion system.

3.3.2. Global annual atmospheric growth rates

Figure 5 shows the time series of the global annual growth rates from NOAA, from the CAMS inversion and from the three CRDP inversions. Note that the NOAA estimate and the CAMS one are not independent since CAMS assimilates the individual NOAA measurements. Their difference has a standard deviation of 0.17 ppm and a bias of 0.02 ppm (based on 37 yearly values). The misfit between the growth rate from the XCO₂_GOS_SRFP-inversion and the NOAA estimate shows qualitatively similar statistics (based on 6 values): a bias of 0.02 ppm and a standard deviation of 0.17 ppm. They are larger for the XCO₂_GOS_OCFP-inversion: a bias of 0.10 ppm and a standard deviation of 0.29 ppm, based on 6 values. For the XCO₂_SCI_BESD inversion, the bias and the standard deviation are 0.01 and 0.32 ppm, based on 8 values. Note that the quality of the growth rate of the retrievals themselves may be much better (Schneising et al. 2013), but since they do not cover the full globe all the time the inversion system, informed by the transport model (hard constraint), may generate very different XCO₂ between the retrievals, for instance to fit small spurious retrieval signals.

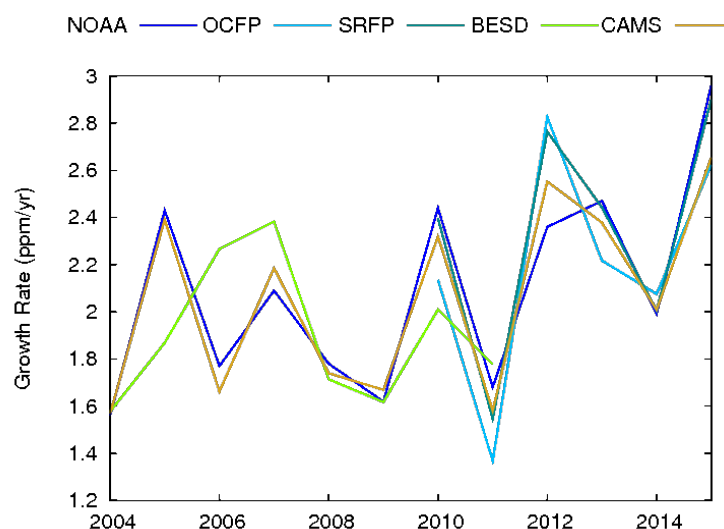


Figure 5. Global annual atmospheric growth rate from NOAA
(ftp://aftp.cmdl.noaa.gov/products/trends/co2/co2_gr_gl.txt, accessed 6 January 2017) between years 2004 and 2015, from the CAMS inversion and from each CRDP-based inversion.

3.3.3. Maps of annual budgets

Figure 6 displays the maps of the inferred annual budgets of natural CO₂ for the year 2010, which is common to all observation system.

Similarities (e.g., in Australia or over most oceans) and dissimilarities (e.g., in South America or in Russia) can be seen in the budget patterns. This is not surprising because the location, type of data (column vs. point wise) and assigned observation errors vary for each case. A striking difference is the smaller amplitude of the surface-air-sample budgets compared to the satellite ones. It illustrates the large observational constraint from the satellites. The three CRDP inversions diagnose carbon uptake over the temperate land ecosystems and carbon release to the atmosphere on average over the tropical land ecosystems.

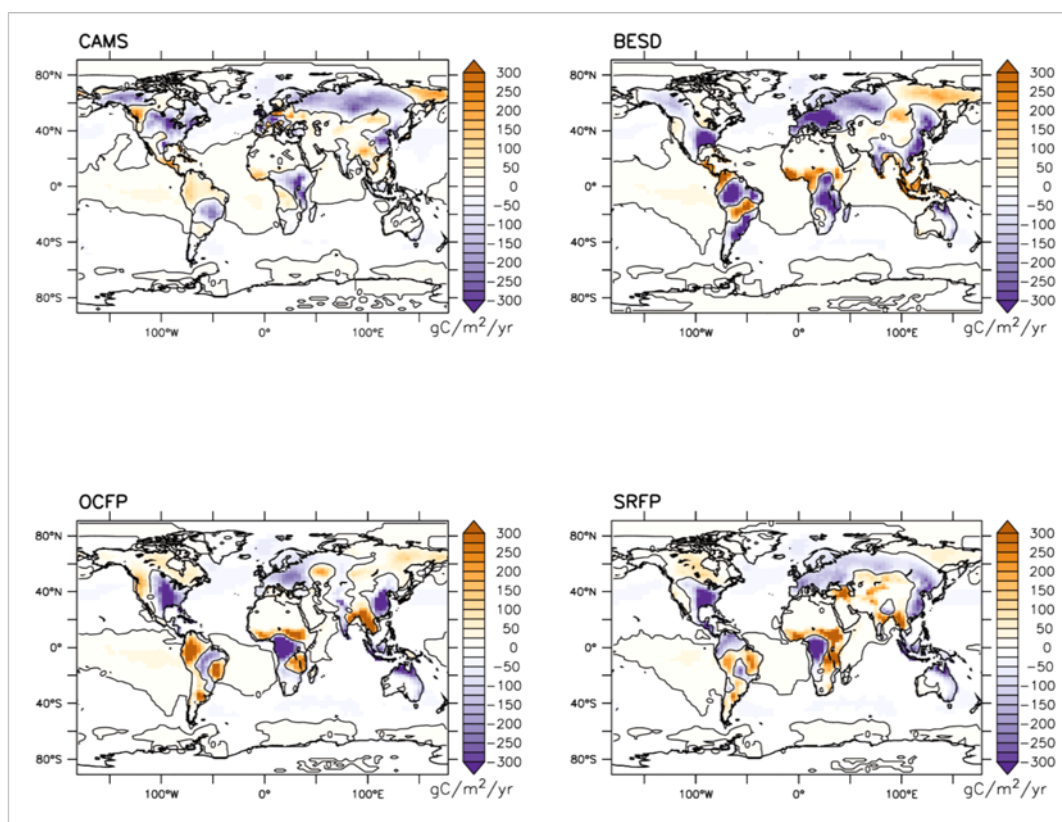


Figure 6. Grid-point budget of the natural CO₂ fluxes for the year 2010 and for the inversions performed with the surface air-sample measurements (CAMS) and the CRDP#4 products. In the sign convention, positive fluxes correspond to a net carbon source into the atmosphere.

3.3.4. Seasonal cycles

Figure 8 shows the inferred seasonal cycle of natural CO₂ fluxes over land for the same year (2010) at the coarser spatial resolution of the Transcom3 tiling (Figure 7). The broad shapes (phase and amplitude) of the curves are fairly consistent with each other. Differences are mainly in the amplitude, like over Northern Africa. The differences are more pronounced over ocean (Figure 9) where the variations are smaller and where no satellite data are assimilated for XCO₂_SCI_BESD (the information about the inferred ocean fluxes is provided by the land retrievals through the atmospheric transport model sensitivities).

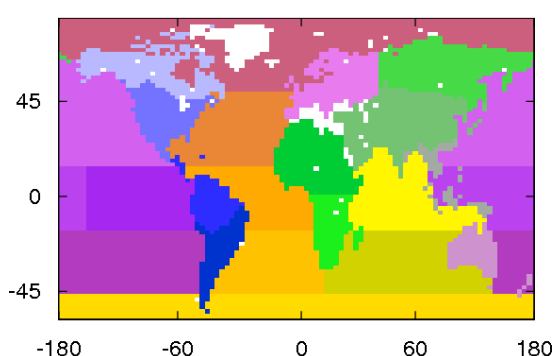


Figure 7. Transcom regions from Gurney et al. (2002).

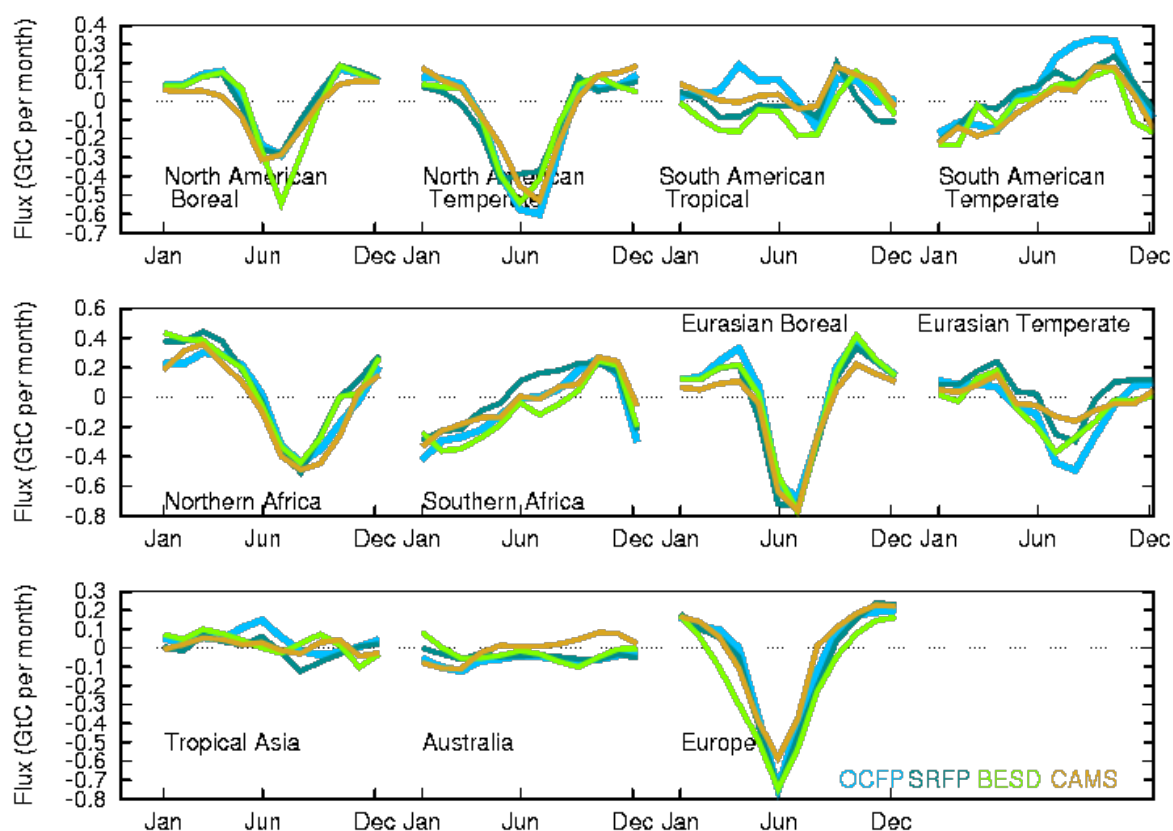


Figure 8. Seasonal cycle of the inferred natural CO₂ fluxes (without fossil fuel fluxes) over the 11 TransCom3 land regions for 2010. In the sign convention, positive fluxes correspond to a net carbon source into the atmosphere.

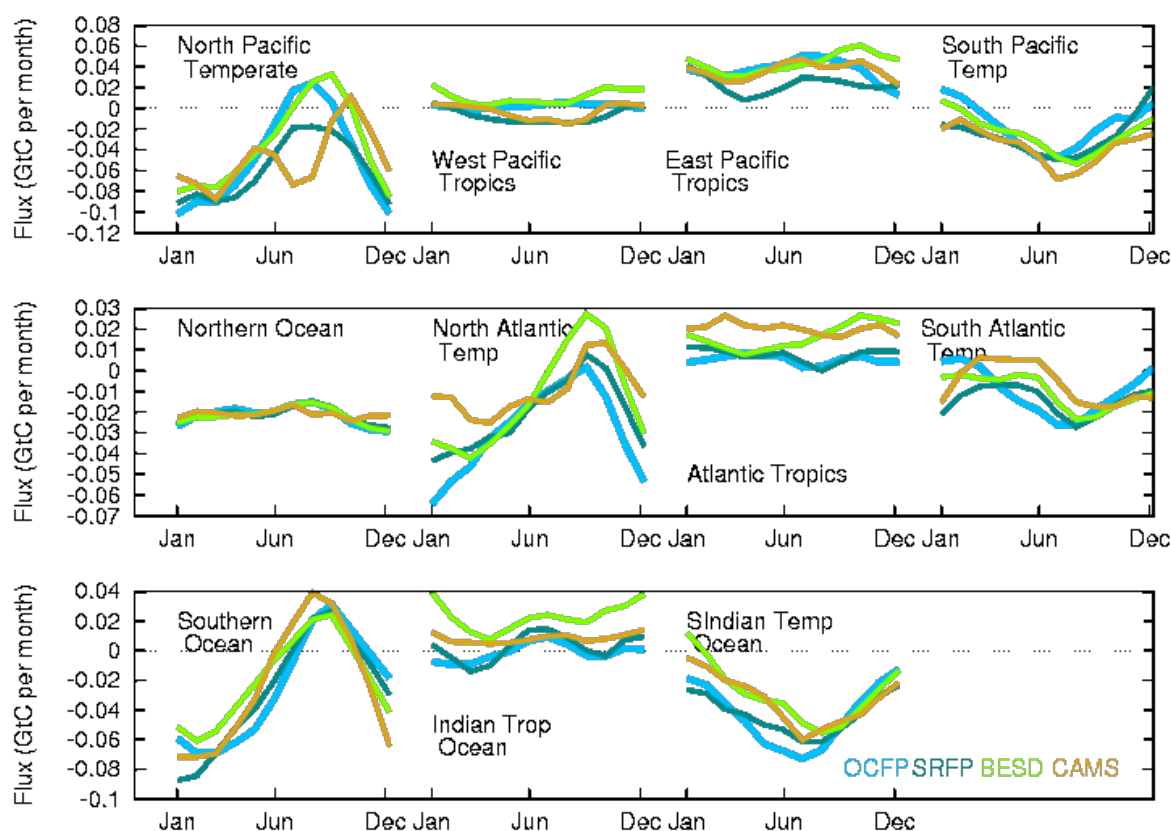


Figure 9. Same as Figure 8 but for the ocean regions.

3.3.5. Annual regional budgets

The time series of the annual regional budgets of the inferred natural fluxes over land are synthesised in Figure 10.

The satellite-based inversions are consistent with each other for boreal Northern America and Australia. For boreal North America, the source of 0.3 GtC/yr inferred by the SCIAMACHY inversion for some years and by the two GOSAT inversions contrasts with bottom-up studies (Pan et al. 2011). For Australia, the fact that the large uptake in 2010 and 2011 found by all GOSAT inversions is not inferred by the surface-based one is expected. Indeed, atmospheric air sample measurements in Australia are taken under baseline conditions, which are designed to avoid sampling air that has recently crossed the Australian continent (Haverd et al. 2013): the small yellow error bar of the surface inversion is likely much underestimated. The satellite-inferred sink of 0.6 GtC/yr for Australia in 2011 is actually consistent with the independent study of Poulter et al. (2014) that highlighted the role of precipitation in this anomaly. It was also reported in CRDP#2 and #3, but with slightly larger amplitude (Chevallier et al. 2015, 2016). See also Detmers et al. (2015) and Ma et al. (2016).

We also note some similarities, in terms of amplitude, trend and year-to-year variability, between the 8-year long time series of XCO₂_SCI_BESD and the surface air-sample inversion in Tropical Asia

and temperate Eurasia. This agreement on some patterns is driven by the measurements themselves since the CAMS prior natural fluxes have no interannual variability.

For Europe, only the XCO₂_SCI_BESD inversion suggests an uptake larger than 1 GtC/yr. This contrasts with previous studies (CRDP#2 and #3, Basu et al. 2013, Chevallier et al. 2014a and Reuter et al. 2014a), that systematically found a large uptake in Europe from satellite XCO₂ retrievals. Reuter et al. (2014a) interpreted this large uptake as a physical signal while Chevallier et al. (2014) interpreted it as an artefact. Without closing this debate, we note that the CRDP#4 GOSAT inversions here are more in line with the bottom-up inventories for this region (0.3 GtC/yr on average for 2002-2005, Schulze et al. 2009); they show an even smaller sink that the CAMS surface-based inversion after year 2011. Only the SCIAMACHY inversion shows an “unexpectedly large sink” anymore.

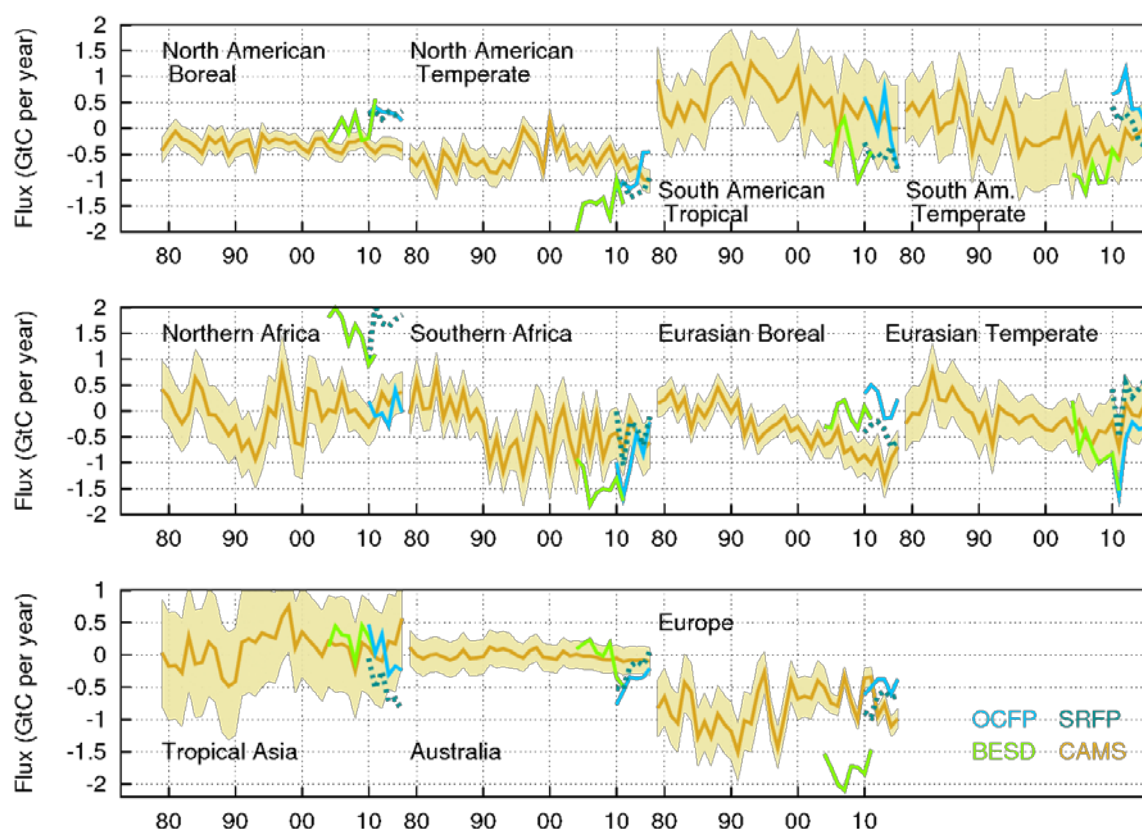


Figure 10. Inferred natural CO₂ annual flux (without fossil fuel emissions) averaged over the TransCom3 land regions and over the globe. The gold curve corresponds to the CAMS product with its 1-sigma Bayesian uncertainty. In the sign convention, positive fluxes correspond to a net carbon source into the atmosphere.

In Northern Africa, the XCO₂_SCI_BESD and XCO₂_GOS_SRFP inversions consistently suggest a stronger source compared to the surface inversion, between 1 and 2 GtC/yr, but the XCO₂_GOS_OCFP and the surface inversion agree about a neutral budget. The large emissions inferred in Northern Africa by two of the inversions do not seem to be consistent with the fact that

fire emissions alone likely amount to less than 0.7 GtC/yr there (van der Werf et al. 2010) despite their significant role in the African carbon budget.

In Temperate North America, the uptake inferred by the satellite inversions (> 1 GtC/yr) is much larger than the surface-based inversion and than the reference multiyear estimate of Crevoisier et al. (2010).

The inferred ocean budgets have much less variability and are not markedly different from the prior at basin scale (Figure 9). The ocean global budget for XCO₂_GOS_OCFP and XCO₂_GOS_SRFP (a mean natural uptake of 1.7 and 2.1 GtC/yr, respectively, for 2010-2015) is rather consistent with current knowledge (Wanninkopf et al. 2013). In the case of XCO₂_SCI_BESD the mean natural uptake for 2004-2011 is 0.7 GtC/yr only but this result may be caused by the absence of SCIAMACHY retrievals over the ocean that leaves oceans unobserved directly. Basin-scale results are shown in Figure 11.

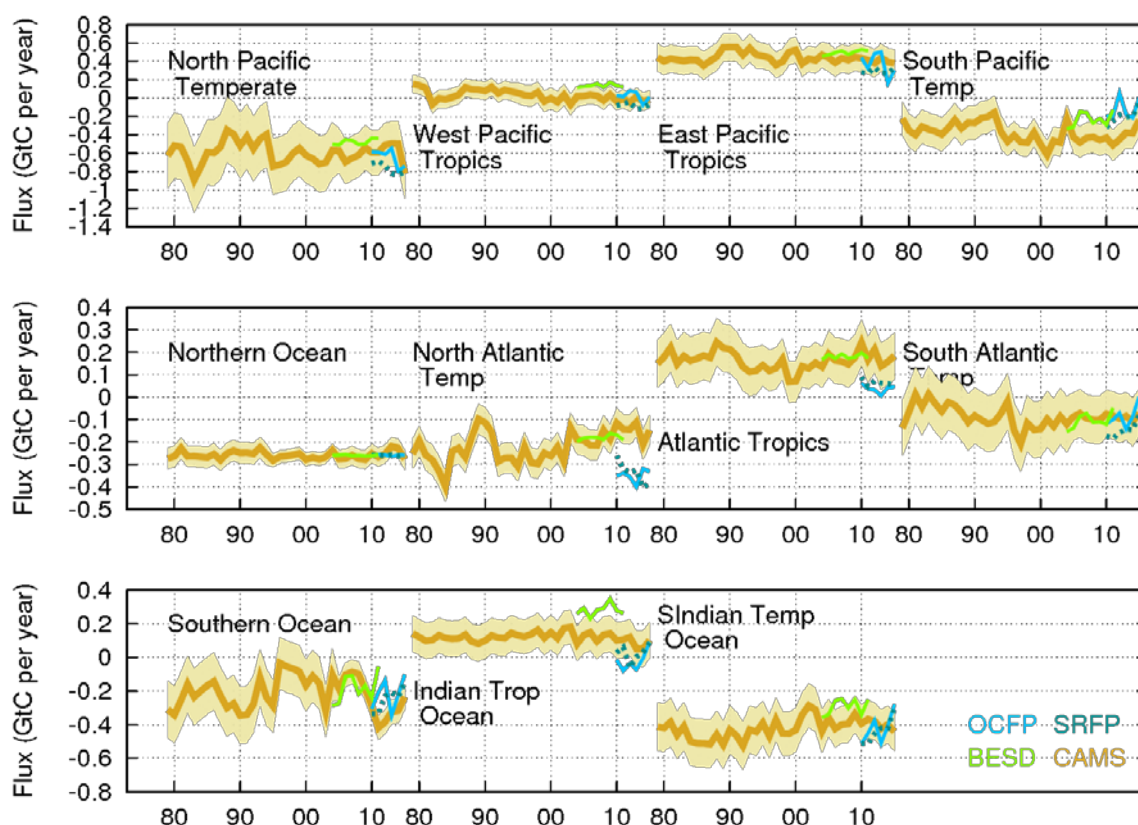



Figure 11. Same as Figure 10, but for the ocean basins.

In summary, the CO₂ flux inversions based on the analysed satellite retrievals (different sensors, different algorithms) still show large differences with the surface inversion and with some bottom-up studies in some regions, but this is less the case for the GOSAT –based inversions compared to CRDP#3, in particular for Europe.

	ESA Climate Change Initiative (CCI)	Page 26
	Climate Assessment Report (CAR)	
	for the Essential Climate Variable (ECV) Greenhouse Gases (GHG)	Version 4 (final)
		28 March 2017

3.3.6. Conclusions

XCO₂_SCI_BESD, XCO₂_GOS_OCFP and XCO₂_GOS_SRFP have been tested within the LSCE inversion system and the results have been compared to a reference surface air-sample inversion (CAMS v15.4). The large increments brought by the inversion on the prior surface fluxes confirm that the satellite data bring a strong constraint on the inferred fluxes, arguably stronger than the surface data. The quality of this constraint, that merges information from the retrievals themselves and information from transport and error modelling, does not appear to be fully satisfactory. However, compared to the CRDP#3 version of these retrieval products, that were evaluated with the LSCE system as well, there is no region any more where satellite-based inversions are all inconsistent with current knowledge, apart from boreal North America. For instance, the two GOSAT inversions now infer a sink in Europe even smaller than the surface-based inversion, and one of the GOSAT inversions infers a neutral budget in Northern Africa. We also note some remarkable convergence of the results from the retrievals and from other data sources in some regions, like Southern Africa, temperate Eurasia, Tropical Asia or Australia. We note, however, that the first three months of XCO₂_SCI_BESD could not be used in the atmospheric inversion. Remaining inconsistency of each inversion with current knowledge in some regions still suggest that satellite-based inversion results should be interpreted particularly cautiously.

3.4. Inversion experiments with the Jena system

3.4.1. Method

The Jena Inversion (MPI-BGC) uses the TM3 transport model and its adjoint. The simulations presented here were carried out at two different spatial resolutions: the base case of 3.8×5 degrees² with 26 vertical levels, and a higher resolution case of 1.875×1.875 degrees² with 32 vertical levels. The higher resolution runs were added to this version of the CAR to determine the effect of model resolution. Meteorological inputs (winds, pressure, specific humidity, temperature) are 3-hourly from the ERA-interim reanalysis. For a full description of the TM3 transport model, please see Heimann and Körner (2003).

A flux model based on various frequency components is used, as described in Rödenbeck (2005). The resultant optimized fluxes are at a daily time resolution. The biospheric prior flux has spatial structure based on a process-based model but is flat in time, meaning that the full seasonal cycle and interannual variability are induced only from the observational data. Furthermore, the ocean fluxes are tightly restricted, with the long-term prior of the ocean fluxes based on an ocean interior carbon inversion, using the sum of the pre-industrial air-sea fluxes from Mikaloff-Fletcher et al. (2007), the ocean uptake flux induced by the anthropogenic perturbation from Mikaloff-Fletcher et al. (2006), and the riverine fluxes of Jacobson et al. (2007). The seasonality of the fluxes is taken from Takahashi et al. (2002). Only the interannual component of the ocean flux model is adjustable, resulting in a more restricted prior. The fossil fuel emissions are pre-subtracted and not adjusted. This flux is taken

from EDGAR 4.2, using the Fast Track 2010 product for 2009 and 2010, with extrapolation based on BP global totals for 2011 through 2013, and a 2% annual increase assumed for subsequent years. All EDGAR 4.2 categories are used except for biomass burning.

The following inversions are presented in this section:

Dataset name	Version	Availability of measurements	Simulation period	Short name
CO2_SCI_BESD	v02.01.02	01.2003-03.2012	2003-2012	BESD
CO2_GOS_OCFP	V7.0	04.2009-12.2014	2009-2015	OCFP
CO2_GOS_SRF	v2.3.8	06.2009-12.2014	2009-2015	SRFP
CO2_EMMA	v2.2b	06.2009-03.2012	2009-2012	EMMA
M96n (49 stations)	N/A	1996-present	2002-2015	M96n

Table 2: Datasets and simulations using the Jena inversion system considered in this section.

For all the inversions, the error provided in CRDP#4 was used, and was combined in quadrature with a model error of 3 ppm on the column. Only measurements with a “good” data flag were used. The inversion period was chosen so as to include the full data record for each product, i.e. 2003-2012 inclusive for SCIAMACHY BESD retrievals, 2009-2015 inclusive for GOSAT retrievals, and 2009-2012 for EMMA.

The final simulation shown in the table (M96n) is based on a selection of surface stations, as well as one regular aircraft profile in Siberia. The data were chosen for their consistent record over a long period, from 1996 to present, in this case. No gap-filled or smoothed data products (like GLOBALVIEW) were used. In order to balance the different sampling of continuous and flask measurements, a temporal deweighting is applied to the surface-based measurements, dividing by the number of measurements at each station in a three-week period (Rödenbeck et al., 2005). No temporal deweighting is applied to the satellite measurements.

3.4.2. Results

The comparison focuses on the following four quantities:

- Global annual growth rate,
- Pixel-based annual-total fluxes,
- Seasonal cycle on a regional scale,
- Regional annual CO₂ budgets.

3.4.2.1. Global annual growth rate

The first of these, the global annual growth rate, is the most robust constraint. This is well-defined by a network of marine surface stations operated by NOAA. The monthly global atmospheric abundance of CO₂ is regularly calculated and published online. These monthly data were retrieved from ftp://aftp.cmdl.noaa.gov/products/trends/co2/co2_mm_gl.txt, and the annual growth rate was

calculated by taking the difference between two months separated by one year. The values are plotted according to the beginning of the 12-month period used for the calculation.

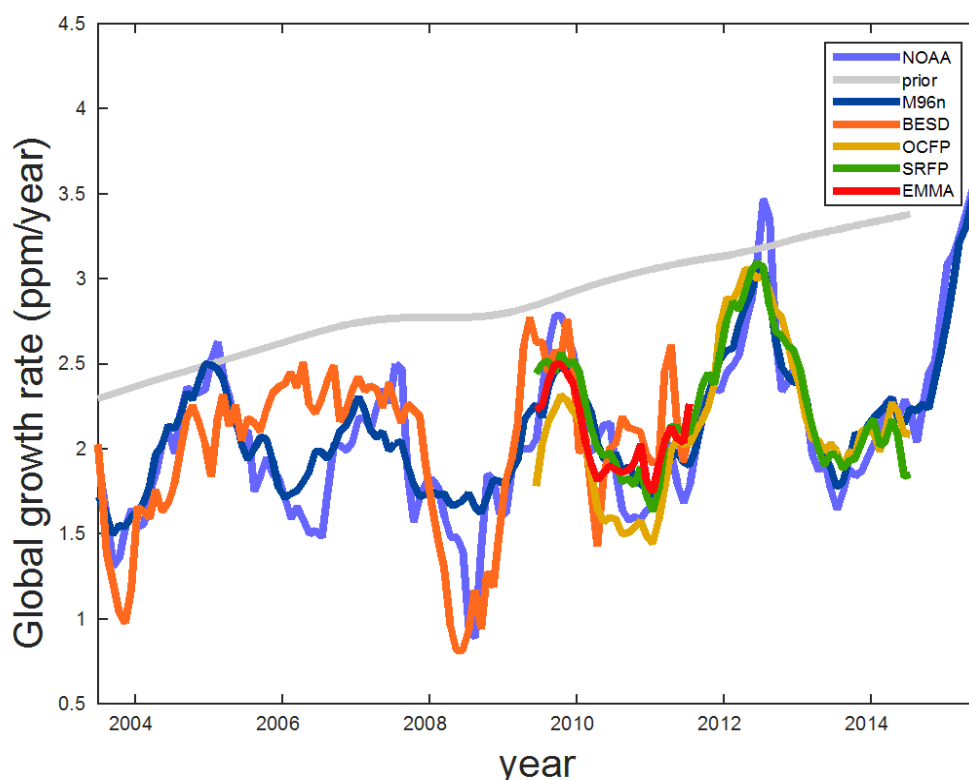



Figure 12: Global atmospheric growth rate of carbon dioxide, as measured by NOAA's marine measurement network (in pale blue) and as deduced from the inverted fluxes. The growth rates inferred from the satellite-based simulations are only available for a subset of the time series. The values along the x-axis correspond to the beginning of the 12-month period over which the growth rate is calculated.

Likewise, the global annual growth rate was calculated for each of the inversions given in Table 2. In this case, the net flux, including the fossil fuel component, was summed over a year, and this change in mass was converted to a growth rate in ppm/year. The results of this intercomparison are shown in Figure 12. All the satellite products produce fluxes that correlate with the growth rate measured by NOAA. The surface network matches quite well, as would be expected, as it is based largely on overlapping data series. The M96m fluxes produce a growth rate with a correlation coefficient with the NOAA value of 0.90, a mean bias of 0.05 ppm/year, and the difference between the two has a standard deviation of 0.20 ppm/year over the period plotted. The BESD-inversion-based growth rate, compared with the NOAA values from mid-2003 through mid-2011, has a correlation coefficient of 0.59, a bias of 0.08 ppm/year, and the difference has a standard deviation of 0.38 ppm/year. The GOSAT data records are significantly shorter, and are only compared from 2010 through 2014.5, but show a very good correlation with the NOAA baseline. The OCFP-based growth rate has a correlation coefficient of 0.83 when compared to the NOAA values, a mean bias of 0.01 ppm/year, and the difference has a standard deviation of 0.25 ppm/year, while the SRFP-based growth rate has a

	ESA Climate Change Initiative (CCI)	Page 29
	Climate Assessment Report (CAR)	
	for the Essential Climate Variable (ECV) Greenhouse Gases (GHG)	Version 4 (final)
		28 March 2017

correlation coefficient of 0.87, a mean bias of 0.07 ppm/year, and a standard deviation of 0.21 ppm/year. The strong disagreement found for SRFP in CAR#3 at the end of the record has fully disappeared, confirming that it most likely was, as postulated, an edge effect. The growth rate inferred from the EMMA inversion was not analyzed in this way, as the short inversion period did not allow for a sufficient comparison. Nonetheless, it can be seen that the agreement seems comparable to that of the other satellite products, as would be expected.

3.4.2.2. Pixel-based total annual fluxes

For the comparison of the spatial distribution of annual fluxes, the time period 2010-2011 was chosen, as both sensors were active during this period and for a time afterwards. This ensures that the analysis period is not overly influenced by spin-up or edge effects. Figure 13 shows the pixel-based annual fluxes for each of the simulations given in the table at the base resolution. The time period from 2010-2011 was plotted, as these two years have full data coverage for both sensors.

In general Figure 13 shows more intense flux patterns for satellite products compared to the M96m inversion based on the surface-based measurement network, likely as a result of the increased measurement density.

The satellite-based simulations (BESD, OCFP, SRFP, EMMA) agree in some broad features: the increased amplitude of positive fluxes from the tropics, and an increased extratropical sink in North America and western Eurasia, as has been reported in the literature (Basu et al., 2013; Chevallier et al., 2014a; Reuter et al., 2014a). On finer scales the fluxes are less congruous: Australia, on the other hand, is seen as a significant sink in the SRFP-based inversion, consistent with the greening that has been reported there during this period (Poulter et al., 2014; Detmers et al., 2015), whereas the fluxes in the OCFP inversion show only a relatively small sink. The BESD-inferred fluxes continue to display a strong sink along the eastern half of Australia and a source in the western half, as in the analysis of CRDP#3.

Compared to the previous CRDP version, the resultant fluxes show a reduction in the North Africa source in both the OCFP and the SRFP version, with the former showing also a significantly stronger sink in tropical Africa. The OCFP- and SRFP-derived fluxes also seem to show a less pronounced sink in Europe, with the latter showing particularly a reduction in Eastern Europe. The SRFP fluxes also seem to have a less pronounced sink in Australia. For all products the South American flux patterns is more or less consistent in terms of spatial pattern with that retrieved from the same product in the previous CAR, but there are significant differences between them in this poorly constrained region. An example is the region around Colombia, which ranges from a strong source (in the BESD and EMMA inversions) to a strong sink (in the SRFP inversion) to nearly neutral (the surface-based and OCFP inversions, as well as the prior).

Climate Assessment Report (CAR)

for the Essential Climate Variable (ECV)
Greenhouse Gases (GHG)

Version 4
(final)

28 March 2017

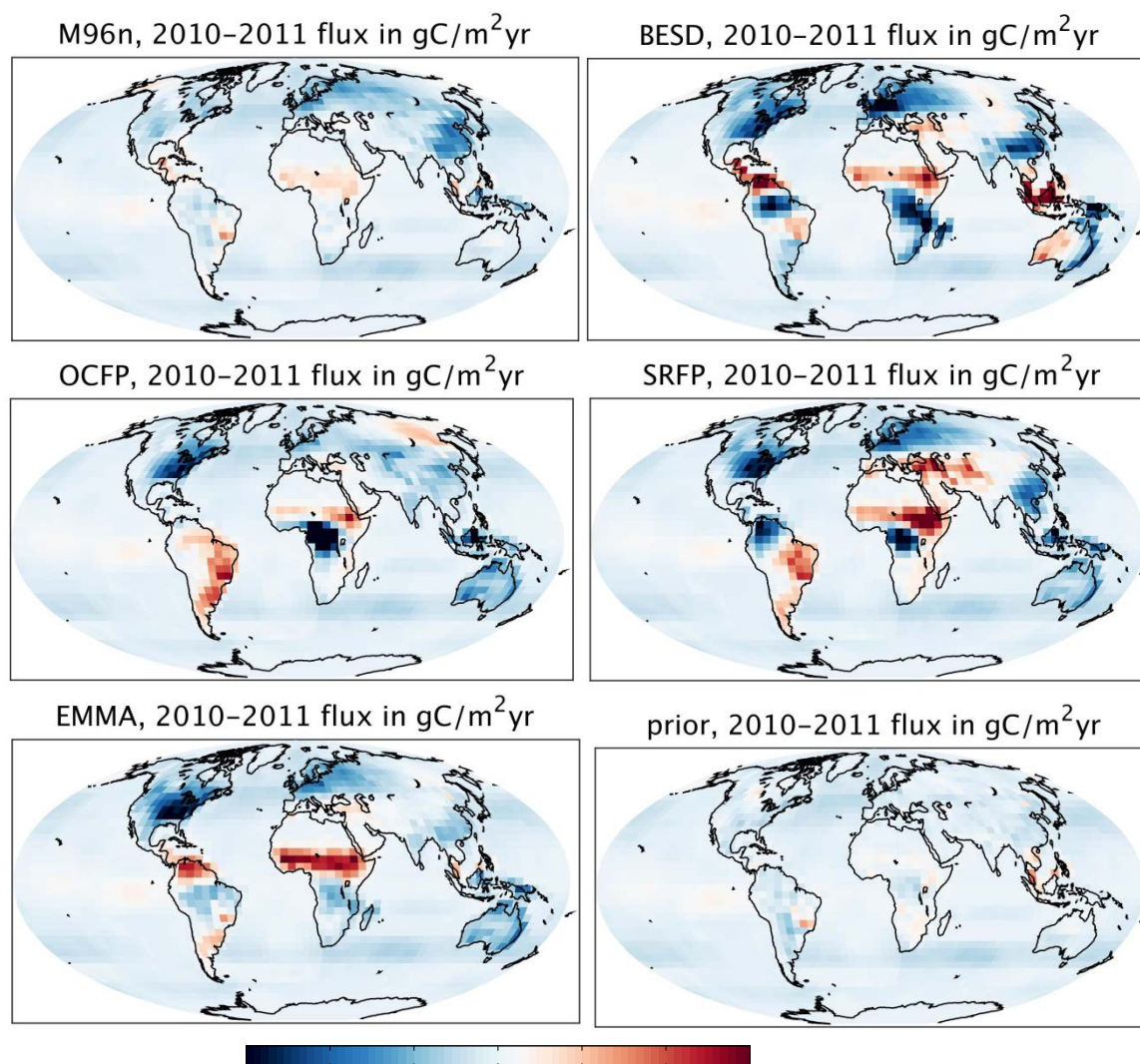


Figure 13: The natural fluxes averaged over the years 2010 and 2011 for inversions based on a variety of retrievals and data products, as labelled.

It has been suggested that the spatial discrepancies between the surface-based and satellite inversions might be resolved through the improvements in transport brought about by a higher spatial resolution. In an effort to test this hypothesis, the same setup was used with the higher resolution of the TM3 model, the results of which are shown in Figure 14. Remarkably, the spatial patterns for the OCFP, SRFP, and EMMA inversions are close to identical. The spatial pattern for the BESD inversion is roughly similar, but grossly exaggerated, leading to flux gradients more extreme than one would expect. The inversion based on the surface measurements also results in unrealistic spatial gradients, especially across the tropics, which are very poorly constrained by surface measurements here. Interestingly, the higher spatial resolution pushes the surface-based inversion to have a larger sink in Eastern Europe, but not too much should be read into this given the general unrealistic nature of the result. It may be that the surface measurement network is unable to constrain the larger number of degrees of freedom resulting from the higher spatial resolution.

Climate Assessment Report (CAR)

for the Essential Climate Variable (ECV)
Greenhouse Gases (GHG)

Version 4
(final)

28 March 2017

Although the spatial correlation lengths are the same as that used in the coarser TM3 inversion, the smaller grid size still clearly has an effect. This seems to result in some instability in the inversions based on both the relatively sparse surface data and the noisier SCIAMACHY measurements.

This result suggests that moving to a smaller spatial resolution is not going to have a significant effect on the regional carbon fluxes derived from the relatively good spatial coverage and low noise of GOSAT measurements, however might require an adjustment to the setup for the surface-based inversion. Despite their unphysical nature, the results have been included here as they are to illustrate the complexity of the problem of improving transport-related errors.

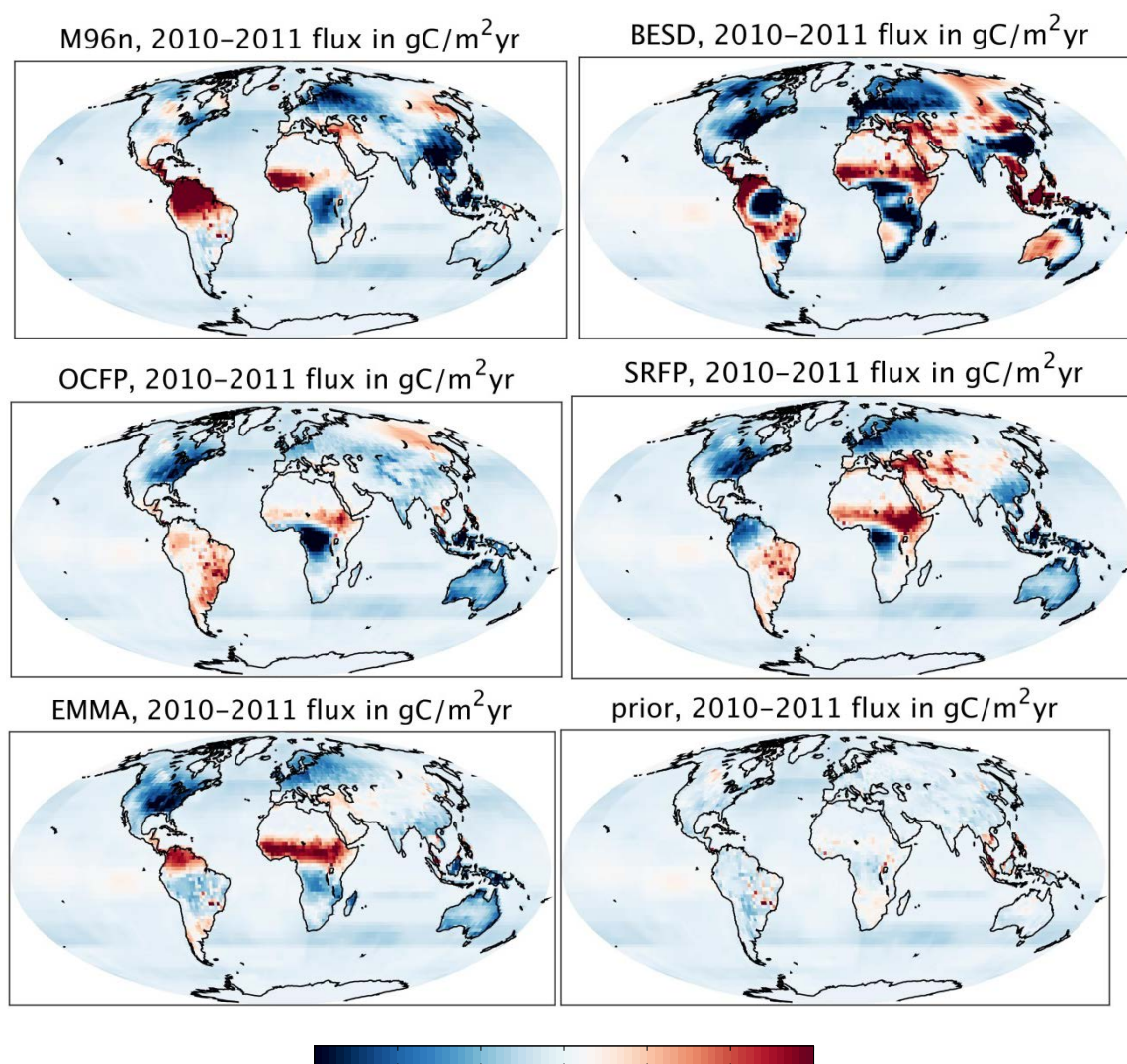



Figure 14: As for Figure 13, but at a higher spatial resolution (1.875×1.875 degrees²) instead of the standard TM3 resolution used in previous CARs (3.8×5 degrees²).

	ESA Climate Change Initiative (CCI)	Page 32
	Climate Assessment Report (CAR)	
	for the Essential Climate Variable (ECV) Greenhouse Gases (GHG)	Version 4 (final)
		28 March 2017

3.4.2.3. Seasonal cycle on a regional scale

The seasonal cycle for the full calendar years 2010 and 2011 are plotted for the 22 TransCom regions of Figure 7 in **Figure 15** (for land) and Figure 16 (for ocean).

For the land regions, the various inversions generally agree about at least the phase of the seasonal cycle. Because the prior for land biosphere fluxes is flat in time in this inversion (shown in grey on the plots), this is not given, and implies that the data constraint is consistent across retrievals. The BESD fluxes are notably noisier than those retrieved from the surface-based measurements or the GOSAT retrievals. In particular, the BESD fluxes do not resolve much of a seasonal cycle for the South American Temperate land region, in contrast to the other inversions. On the other hand, all inversions manage to capture the anomalous seasonal cycle for the South American Tropical region, agreeing upon the higher than usual release of carbon in the second half of 2010, corresponding to droughts in that region. This is consistent with the findings of Gatti et al. (2014), who found the Amazon to be a source of 0.48 PgC during 2010, while remaining carbon neutral in 2011. This is encouraging, as the tropical land regions are notoriously poorly constrained by all data streams.

Although less pronounced than in earlier data versions, differences remain in the North African fluxes, where the satellite-based inversions show larger amplitude for the seasonal cycle. Even the OCFP inversion, which is essentially carbon neutral, exhibits a stronger drawdown and release than that inferred from the surface measurements. The Eurasian Temperate region continues to display significant differences in the shape and a slight offset in the phasing of the seasonal cycle when constrained by the surface-based network rather than the satellite data, with the surface-constrained fluxes showing an earlier and more sharply defined drawdown. As in previous data versions, Australia shows significant differences depending on the data source, which was already implied by the graphs in Figure 14. The surface-based inversion suggests a much smaller seasonal cycle here as well. This finding is consistent with the work of Detmers et al. (2015).

The lack of data to constrain the fluxes in the wintertime at high latitudes can be seen in some of the satellite-based fluxes, with the model even suggesting a wintertime *sink* at times, which is inconsistent with process understanding. This is seen most often in the oscillations of the significantly noisier BESD-based fluxes, however, and is likely an artifact.

In Figure 16, the ocean fluxes also generally show that the BESD-based inversion is rather noisier than the others. However the scale on these figures is significantly smaller than that of the land regions in Figure 15, and this small variability should not be over-interpreted. Compared to the results from CRDP#3 (Chevallier et al. 2016), the SRFP fluxes are much less variable, more in keeping from the results from CAR#2, and closer to what is expected. In the Indian Tropical Ocean region, all the satellite-based inversions exhibit a larger seasonal cycle than that in the prior or surface-based inversions, with more uptake in the first few months of the year. As explained previously, this inversion set-up has a very tightly constrained ocean prior with a seasonal cycle.

Climate Assessment Report (CAR)

for the Essential Climate Variable (ECV)
Greenhouse Gases (GHG)

Version 4
(final)

28 March 2017

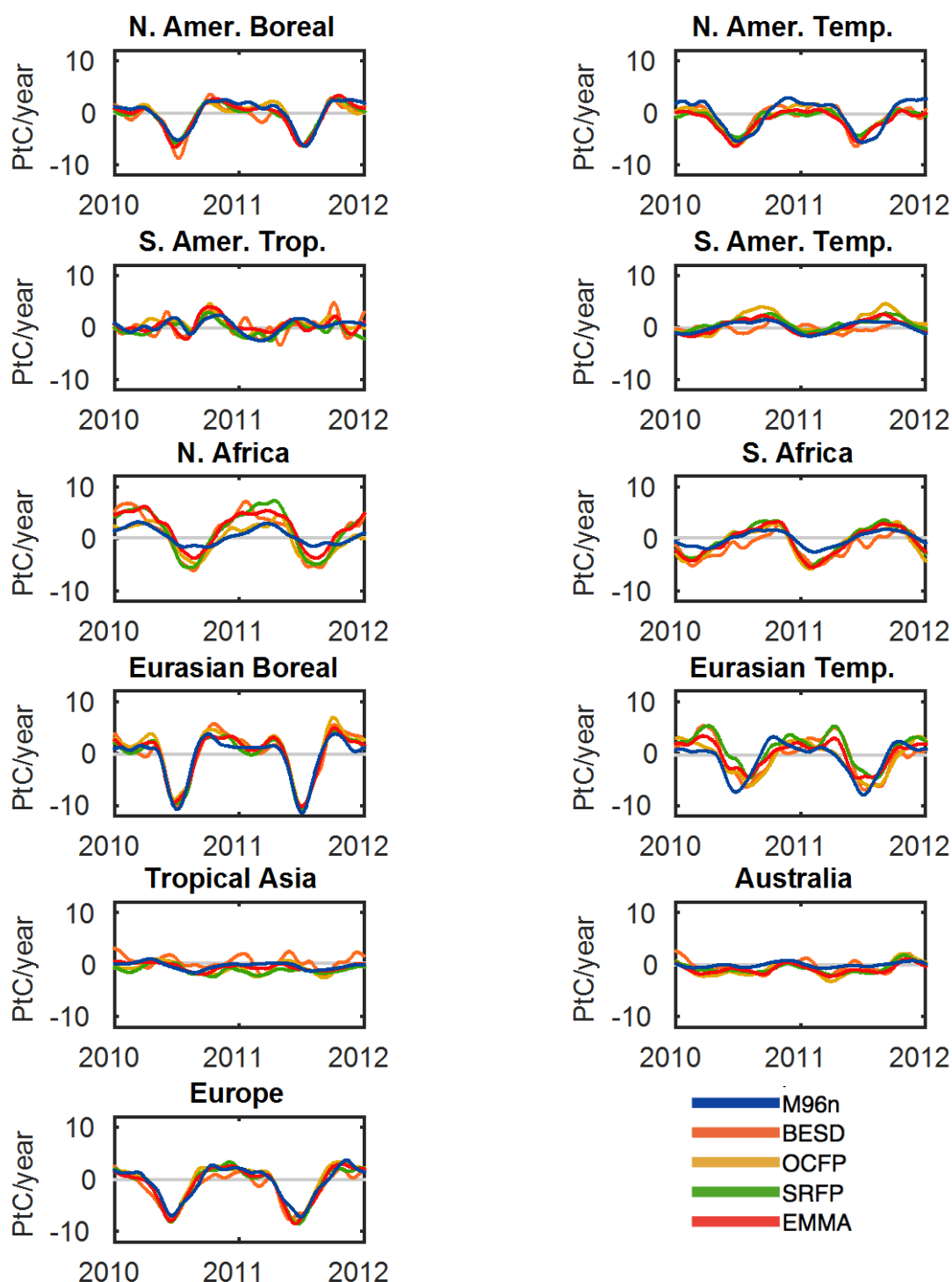


Figure 15: The seasonal cycle of fluxes for the 11 TransCom land regions of Figure 7 are plotted here for the years 2010 and 2011.

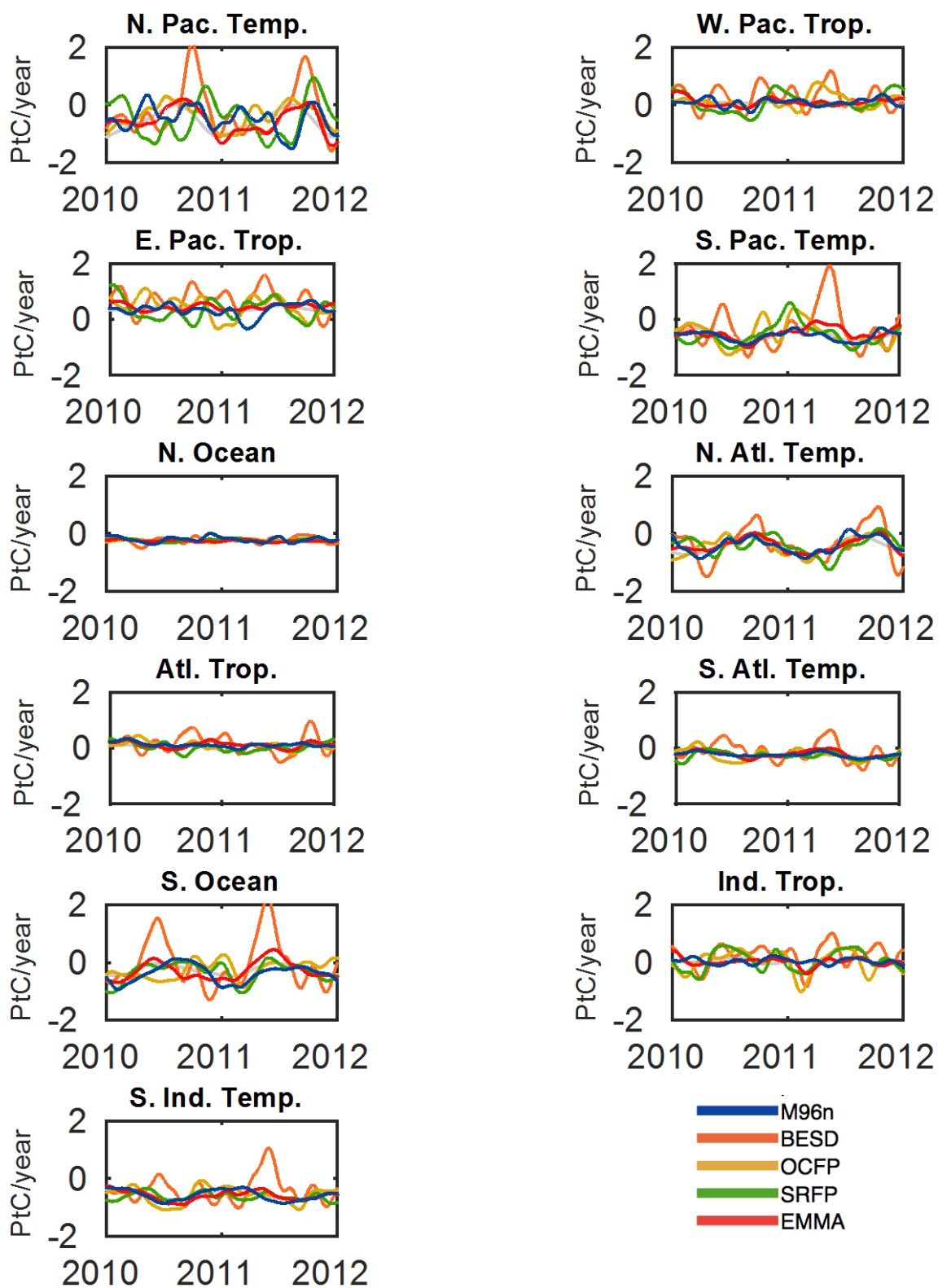


Figure 16: As for Figure 15, but for the ocean regions.

3.4.2.4. Regional annual budgets

Figure 17 shows the mean annual CO₂ budget for the 22 TransCom regions of Figure 7, averaged over the period 2010-2011. As previously explained, the ocean regions have quite a tight prior constraint, and as such most of the significant divergence between the various inverted fluxes is seen in the land regions. In general, the BESD inversion shows the most deviation from the other results for the ocean fluxes. There seems to be some discrepancy across the models with the partitioning of the fluxes in the northern and Tropical Pacific regions, but the integrated result across the basins is consistent.

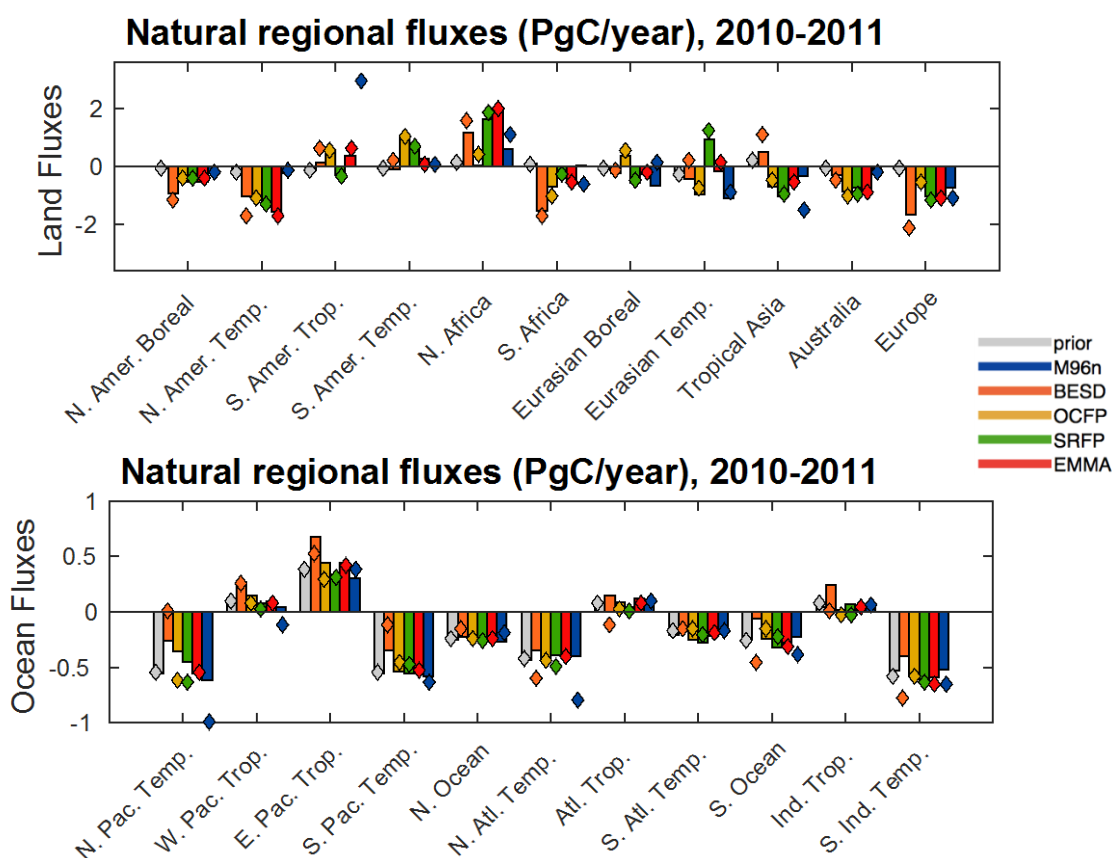



Figure 17: Mean annual fluxes per TransCom region of of Figure 7 for the years 2010 and 2011 based on a range of inversions, coded by colour. The upper panel displays the fluxes for land regions, while the lower panel shows the ocean fluxes. The values derived for the higher resolution simulations are plotted as coloured diamonds on top.

The previously familiar land-based disagreement, with the satellite-based inversions suggesting larger sources over North Africa and larger sinks over the terrestrial extratropics, is less pronounced in this version of the CRDP. While most satellite-based inversions still show a general consensus that the net North American uptake is stronger than what is derived from the surface-based network, in Europe the OCFP inversion now even shows a *smaller* European sink than what is derived from the surface-based network. The anomalously high North African fluxes have been somewhat reduced in

	ESA Climate Change Initiative (CCI)	Page 36
	Climate Assessment Report (CAR)	
	for the Essential Climate Variable (ECV) Greenhouse Gases (GHG)	Version 4 (final)
		28 March 2017

the SRFP- and BESD-derived fluxes, and the OCFP fluxes are further reduced, resulting in zero net carbon fluxes for North Africa over this time period.

The results from the higher resolution inversions are also included in Figure 17, shown as diamonds. It can be seen that for the GOSAT-constrained fluxes (OCFP, SRFP, EMMA), the difference is generally negligible. An exception to this is the North Pacific Temperate region, which gives a result significantly closer to the prior for the higher resolution simulation, resulting in a larger sink. Interestingly, this does not seem to be offset by adjustments to the adjacent land or ocean regions. For the surface-based and BESD-based inversions the results are less comparable, as was already clear from Figure 14. For the surface-based inversions a systematically better agreement between the fluxes at the two spatial resolutions is found for those regions containing multiple measurements sites, whereas the poorly constrained tropics vary considerably, resulting in an exceptionally high source in Tropical South America that is balanced by large sinks in Tropical Asia and the temperate basins of the Atlantic and Pacific.

3.4.2.4. Conclusions

The disagreement in the European fluxes between the satellite- and surface-derived values has been significantly reduced in the results from the CRDP#4, with only the SCIAMACHY BESD retrieval showing a significantly larger source. The tendency towards a larger northern hemisphere sink is however maintained, dominated by the North American Temperate region. This sink may be a result of the need for mass balance, given the larger North African source still derived from all satellite products but OCFP.

On the most stable and reliable metric, the estimation of the global growth rate, the GOSAT-based inversions performed well, with the SRFP fluxes matching the NOAA growth rate slightly better than the OCFP fluxes, a reversal of the conclusions from the TM3 analysis in CAR#3.

An effort was made to test the impact of using higher spatial resolution in the transport model, and the effect was found to be negligible for the GOSAT-constrained inversions (including EMMA), but led to significantly noisier and less realistic flux patterns for the surface-based and BESD inversions. This results requires follow-up study to fully understand the implications for surface-based inversions, but suggests that changing to higher spatial resolutions will not be a panacea leading to convergence between the surface- and satellite-derived fluxes.

3.5. Inversion experiments with the SRON system

3.5.1. Method

Here we present optimized global source-sink estimates of CO₂ using GOSAT XCO₂ observations and surface flask measurements of CO₂ over 84 months from 1 January 2009 to 30 December 2015. Both GOSAT and surface observations were assimilated in the TM5-4DVAR system, using a set-up that

closely follows the framework described in Meirink et al. (2008) and Basu et al. (2013). We refer the reader to the latter paper for a more detailed description of our assimilation setup.

A priori estimates of fluxes from the terrestrial biosphere, biomass burning and land-use change were taken from SiBCASA-GFED4 (van der Werf, 2010; van der Velde, 2014). For ocean flux estimates we used an ocean interior inversion described in Jacobson et al. (2007). A priori fossil fuel emissions were taken from the CARBONES project (<http://www.carbones.eu/wcmqs/>), constructed by USTUTT/IER. The global total fossil fuel emissions for 2010-2015 were scaled to the global totals used in the Global Carbon Budget 2015. We ran our inversions at a monthly temporal and $3^\circ \times 2^\circ$ spatial resolution. The transport model has 25 layers in the vertical. To start with an initial concentration field consistent with the state of the atmosphere, we do a surface data inversion at $6^\circ \times 4^\circ$. The optimized initial concentrations from this inversion were then intrapolated to $3^\circ \times 2^\circ$ spatial resolution.

The following CO₂ products were assimilated in the inversions performed:

- XCO₂_GOS_SRFP v2.3.8, including satellite retrievals over the ocean (*srfp*)
- XCO₂_GOS_OCFP v7.01, including satellite retrievals over the ocean (*ocfp*)
- Observations from 83 NOAA flask sites (*flask*)
- XCO₂_GOS_SRFP v2.3.8 & flask inversion (*joint*)
- XCO₂_GOS_SRFP v2.3.8 & flask inversion, including a land-ocean bias optimization as described by Basu et al. (2013) (*joint_bo*)

We primarily look at the results for September 2009 - September 2015, and thus account for a spin-up period of 9 months, with the first 3 months assimilating only surface data and remaining 6 months assimilating GOSAT XCO₂. The final 3 months are excluded from the analysis (inversion spin down).

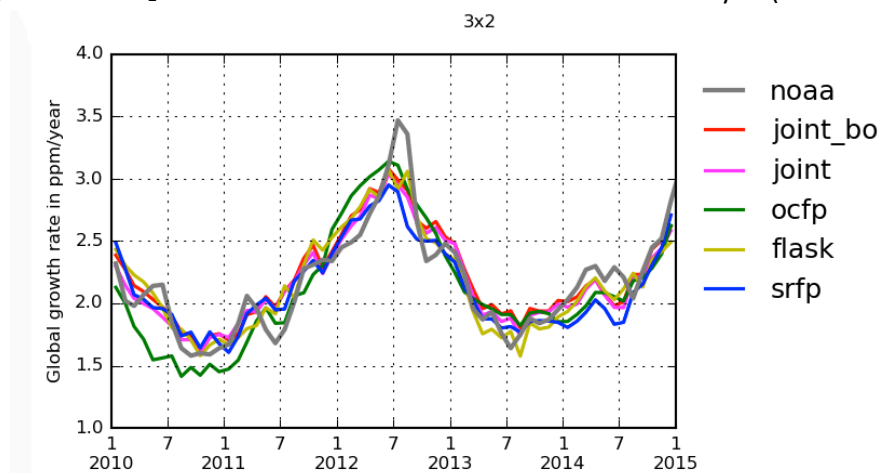



Figure 18. Global atmospheric growth rate of CO₂, as measured by NOAA's marine measurement network (in grey) and as deduced from the inferred fluxes. The values along the x-axis correspond to the beginning of the 12-month period over which the growth rate is calculated. Curve "joint_bo" sometimes overlaps with curve "joint" and hides it.

	ESA Climate Change Initiative (CCI)	Page 38
	Climate Assessment Report (CAR)	
	for the Essential Climate Variable (ECV) Greenhouse Gases (GHG)	Version 4 (final)
		28 March 2017

3.5.2. Global annual growth rate

Monthly CO₂ data from a network of NOAA surface stations

(ftp://aftp.cmdl.noaa.gov/products/trends/co2/co2_mm_gl.txt) were used to calculate a global annual growth rate, defined by the difference between two months separated by one year. To calculate a global annual growth rate for the different inversions, we summed the net flux (biosphere, biomass burning, ocean, and fossil fuel) over a year, and converted this change in mass to a growth rate in ppm year⁻¹. The results for the years 2010-2015 are shown in **Figure 18**, and values are plotted according to the beginning of the 12-month period used for the calculation (so the value of January 2010 represents the growth rate over the January 2010 – January 2011 period). In general, the growth rates of the different inversions compare well to the growth rate measured by NOAA. Pierson correlation coefficients (r) for growth rates from NOAA and the inversions are all above 0.85. The *flask*, *joint* and *joint_bo* inversions had equal and highest correlation (r= 0.92). In comparison, a lower correlation of 0.88 was found for both the *srfp* and *ocfp* inversions.

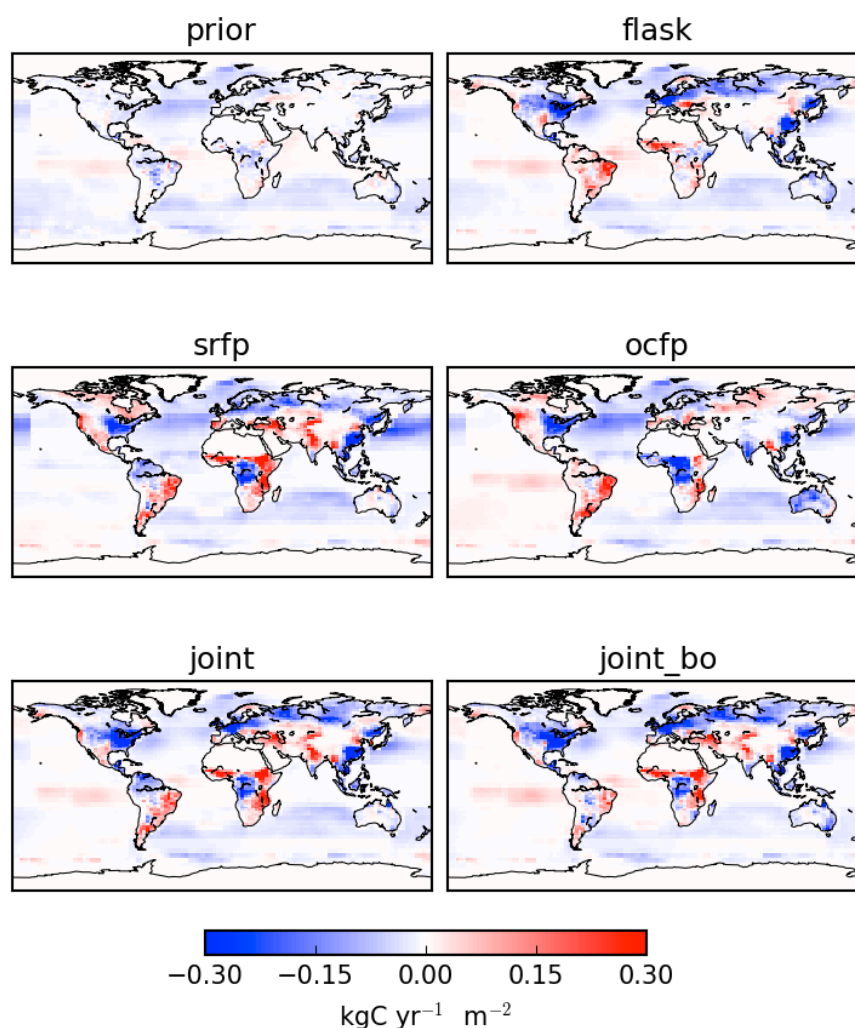


Figure 19. Grid point budgets of the natural CO₂ fluxes (without fossil fuel fluxes) for the prior (top left) and the different inversions performed with TM5-4dvar. An annual average is shown for September 2009 to September 2015. In the sign convention, positive fluxes correspond to a net carbon source into the atmosphere.

3.5.3. Maps of annual budgets

Spatial patterns of annual budgets (mean for September 2009 – September 2015) of natural CO₂ fluxes (excluding fossil fuel emissions) are shown in Figure 19 for the different inversions. Differences between the budgets of those inversions and the prior are displayed in Figure 20. In general, similarities can be found for North America, Europe and Eurasia in all inversions, except for the *ocfp* inversion. In all these regions the inversions point towards a carbon sink that is on average substantially stronger than the a priori estimates.

All GOSAT products (*srfp*, *ocfp*, *joint*, and *joint_bo*) show a carbon sink in western Central Africa (10N-15S, 10E-25E). The inversions assimilating XCO₂_GOS_SRFP also show a source in the eastern Central

Africa (10N-15S, 25E-40E). This spatial pattern is opposite and less pronounced for the *flask* inversion. The *ocfp* Inversion shows substantial disagreements with inversions assimilating XCO₂_GOS_SRFP throughout the World: 1) The *ocfp* inversion shows India as a natural CO₂ sink; 2) The sink over Australia is more pronounced and significantly shifted spatially; 3) The source over Western Africa is diminished.

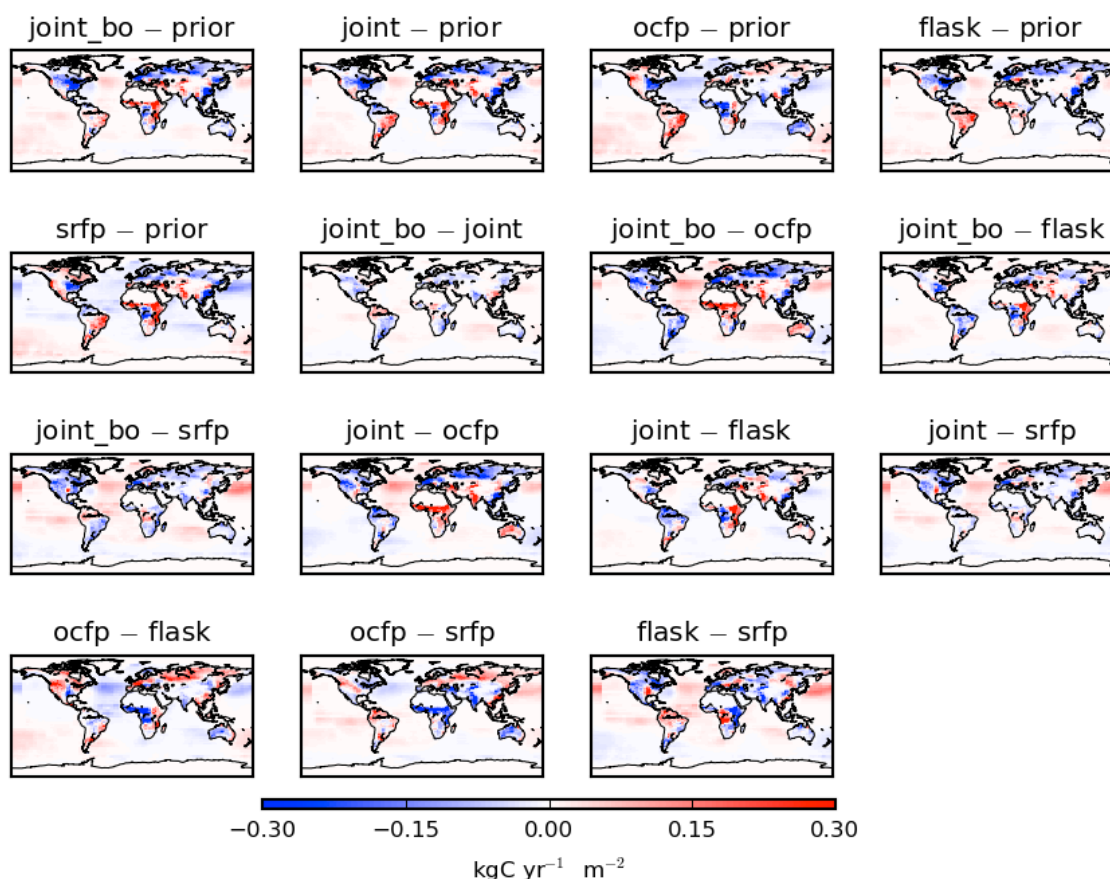


Figure 20. Same as Figure 19, but the differences between the inversions and prior are shown.

3.5.4. Seasonal cycles

To reveal information on temporal variations through the season, the inferred seasonal cycle of natural CO₂ fluxes (average for September 2009 – September 2015) is shown for TransCom land (Figure 21) and ocean (Figure 22) regions. In general, for land regions, most of the shapes (phase and amplitude) correspond well, although for certain regions some interesting differences can be found. For example, the inversions assimilating flask data show North America Temperate as a smaller source compared to rest of the inversions in the winter season. Inversion assimilating XCO₂_GOS_SRFP show a weaker carbon sink compared to other inversions over Eurasian Temperate. Over Europe, all the inversions show a weaker source than the prior in the January-March period. Over Eurasian boreal the carbon sink seems to be underestimated by the prior, because all inversions point to a substantially larger sink in the June-August period.

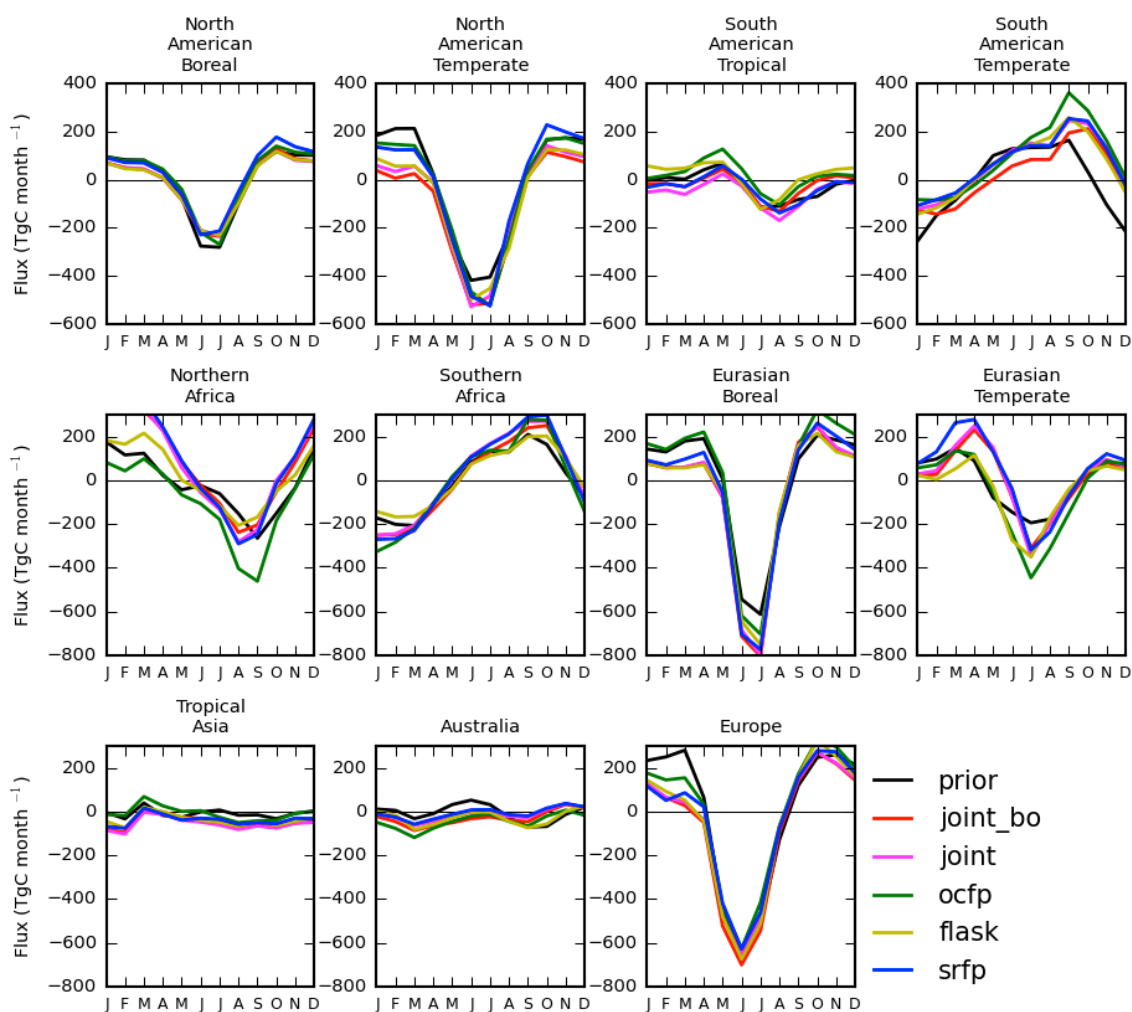


Figure 21. Seasonal cycle of inferred natural CO₂ fluxes (without fossil fuel fluxes) over the 11 TransCom land regions of Figure 7. An annual average for the September 2009 – September 2015 period is shown. In the sign convention, positive fluxes correspond to a net carbon source into the atmosphere.

Over the ocean regions larger discrepancies were found between the inversions. The inversions assimilating flask data show significant differences in seasonal cycle over North Pacific Temperate compared with the *srfp*, *ocfp* inversions, and prior. The *srfp* inversion shows a significantly stronger sink over the region throughout the year. In other regions, compared to the prior, the largest discrepancies (phase and amplitude) are generally found for the *srfp* and *ocfp* inversions, e.g. over South Pacific Temperate and North Atlantic Temperate and the Southern Ocean.

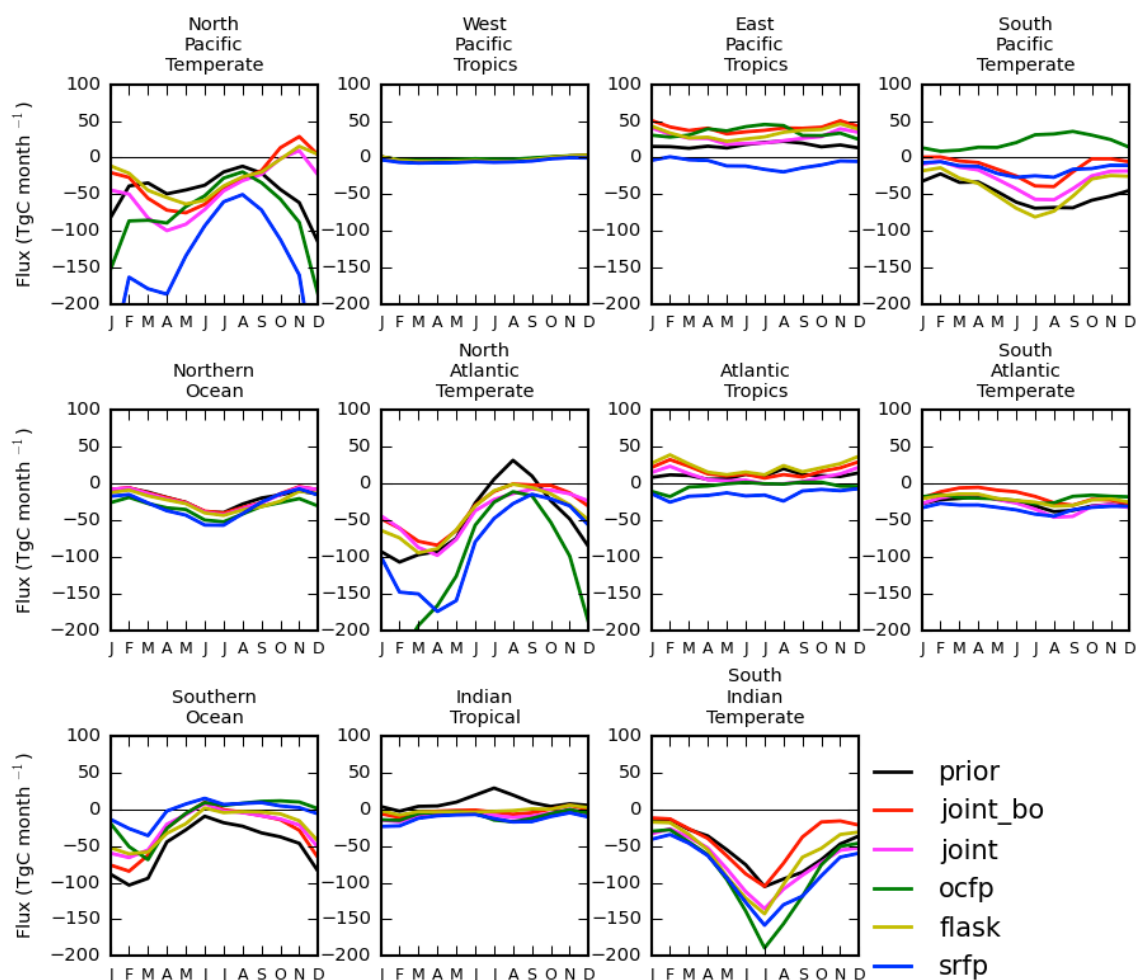


Figure 22. Same as Figure 18, but for ocean regions.

3.5.5. Annual regional budgets

Annual regional TransCom budgets of natural CO₂ fluxes are synthesized for the 5 inversions in Figure 23 (land regions) and Figure 24 (ocean regions). Although for certain ocean regions like South Atlantic Temperate and South Indian Temperate the inversions are generally consistent, the North Pacific Temperate region shows large differences; for the *srfp* inversion a sink of $\sim 1.8 \text{ Pg C yr}^{-1}$ was found, which is a factor ~ 5 larger than the *flask* inversion. Due to this large sink for North Pacific Temperate, total ocean annual flux for *srfp* showed a sink of $\sim 3.5 \text{ Pg C yr}^{-1}$, which is substantially higher compared to the *flask* inversions ($\sim 1.9 \text{ PgC yr}^{-1}$) and results of studies like Chevallier et al. (2011). The *joint* is more in line with the *flask* inversion, pointing towards a sink of 2.1 Pg C yr^{-1} . For most land regions, substantial discrepancies are found as well:

- North American Temperate: All inversions suggest a stronger sink than the prior sink estimate of only $\sim 0.1 \text{ Pg C yr}^{-1}$, with inversions assimilating flask data showing the largest disagreement.

- **South American Tropical:** The *flask* and *ocfp* inversions suggest a source of $\sim 0.15 \text{ Pg C yr}^{-1}$, while the other inversions point towards a sink that is in better agreement with prior flux ($\sim 0.2 \text{ Pg C yr}^{-1}$)
- **South American Temperate:** *ocfp* inversions suggest a stronger source ($\sim 1.1 \text{ Pg C yr}^{-1}$) compared to the *flask* and *srfp* inversion. In contrast, the prior estimates a sink of 0.1 Pg C yr^{-1} .
- **Northern Africa:** While the *srfp* based inversions show a carbon source ranging from 0.8 (*joint_bo*) to 1.1 Pg C yr^{-1} (*srfp*), both prior ($\sim -0.1 \text{ Pg C yr}^{-1}$) and the *ocfp* inversion ($\sim -1 \text{ Pg C yr}^{-1}$) estimate the region as a sink.
- **Europe:** All inversions assimilating XCO₂_GOS_SRFP and/or *flask* show a stronger sink compared to the prior. Surprisingly, the *ocfp* inversion shows the region as carbon neutral. For *joint_bo* this sink is the highest ($\sim 0.9 \text{ Pg C yr}^{-1}$).

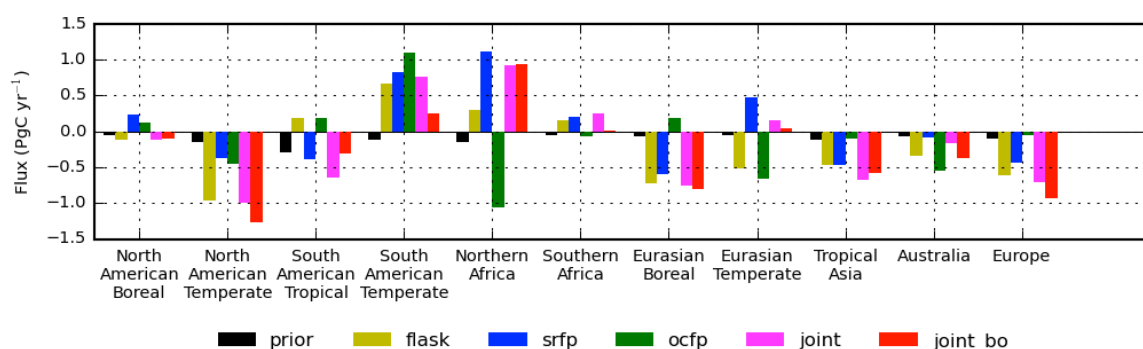


Figure 23. Inferred natural CO₂ annual flux (without fossil fuel emissions) averaged over the TransCom land regions of Figure 7. An average for the years September 2009 to September 2015 is shown. In the sign convention, positive fluxes correspond to a net carbon source into the atmosphere.

3.5.6. Inter annual variability

To reveal information on how the carbon balance is changing over the years, the inter-annual variability (IAV) is plotted in Figure 25 for 4 different TransCom land regions of interest. The IAV is calculated by subtracting the average monthly flux over the September 2009 – September 2015 period from the monthly values. Over South America Tropical the different inversions (except for *flask*) show higher values for the year 2010, which may be the result of the severe drought in the Amazon that caused a source of CO₂ (Gatti et al. 2014). Inverted *srfp* fluxes over 'Northern Africa' for the September 2009 – March 2012 period show on average a stronger source compared to the 2012–2014 period. The same pattern was found for the IAV over the continent of Australia, although the inversions now point towards a strong sink instead of source in the 2010–2011 period. Over Australia the timing of this enhanced sink coincides with a strong La Niña episode, accompanied by record-breaking amounts of precipitation, and in line with recent findings from Bastos et al. (2013), Poulter et al. (2014), and Detmers et al. (2015).

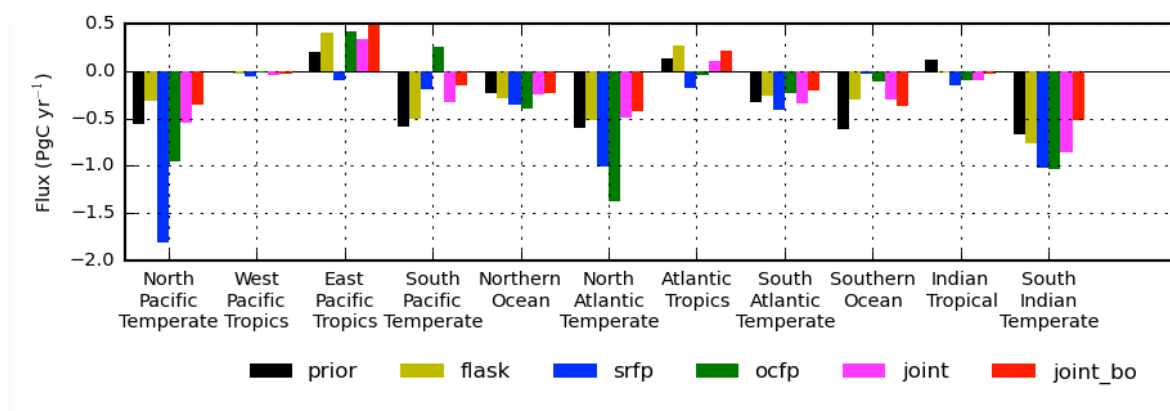


Figure 24. Same as Figure 20, but for ocean regions

3.5.7. Conclusions

Two CO₂ datasets of CRDP#4 have been tested within the TM5-4DVAR inversion system. For most land regions, the seasonal cycle was captured well by all inversions, e.g. patterns of inter annual variability were in line with findings in literature: over ‘South America Tropical’ a carbon source was found by the GOSAT inversions for the year 2010. This variation can likely be explained by the severe drought that took place over the Amazon (Gatti et al., 2010). Over Australia an enhanced sink was found by the inversions for the years 2010 and 2011, coinciding with La Niña conditions and in line with recent findings from e.g. Bastos et al. (2013) and Detmers et al. (2015).

However, for other important land regions from a carbon perspective, like e.g. ‘North America Temperate’ and ‘South America Temperate’, sometimes large discrepancies were found between inversions assimilating different datasets. In general, inversions assimilating XCO₂_GOS_SRFP and XCO₂_GOS_OCFP showed significant differences from each other. For example, the *srfp*, and also the *flask* inversion, lead to an annual natural sink over Europe in range of 0.5-0.9 PgC, however, the *ocfp* inversions finds the region carbon neutral. Simultaneously, the *ocfp* inversion finds Northern Africa as a significant sink of 1 PgC yr⁻¹, while inversions XCO₂_GOS_SRFP product show the region as a source of ~ 1 PgC yr⁻¹. The same counts for North Pacific Temperate, where XCO₂_GOS_SRFP showed a sink of 1.8 PgC yr⁻¹ that is a factor ~5 larger than the *flask* inversion results. Average total ocean flux for XCO₂_GOS_SRFP resulted in a sink of ~3.5 Pg C yr⁻¹, which is very high compared to the flask inversions (~1.9 Pg C yr⁻¹) and not consistent with current knowledge. Interestingly, the application of bias correction in the *joint_bo* inversion leads to a ocean sink of 1.1 Pg C yr⁻¹, which is not in between the *srfp* and *flask* inversion, as one would expect.

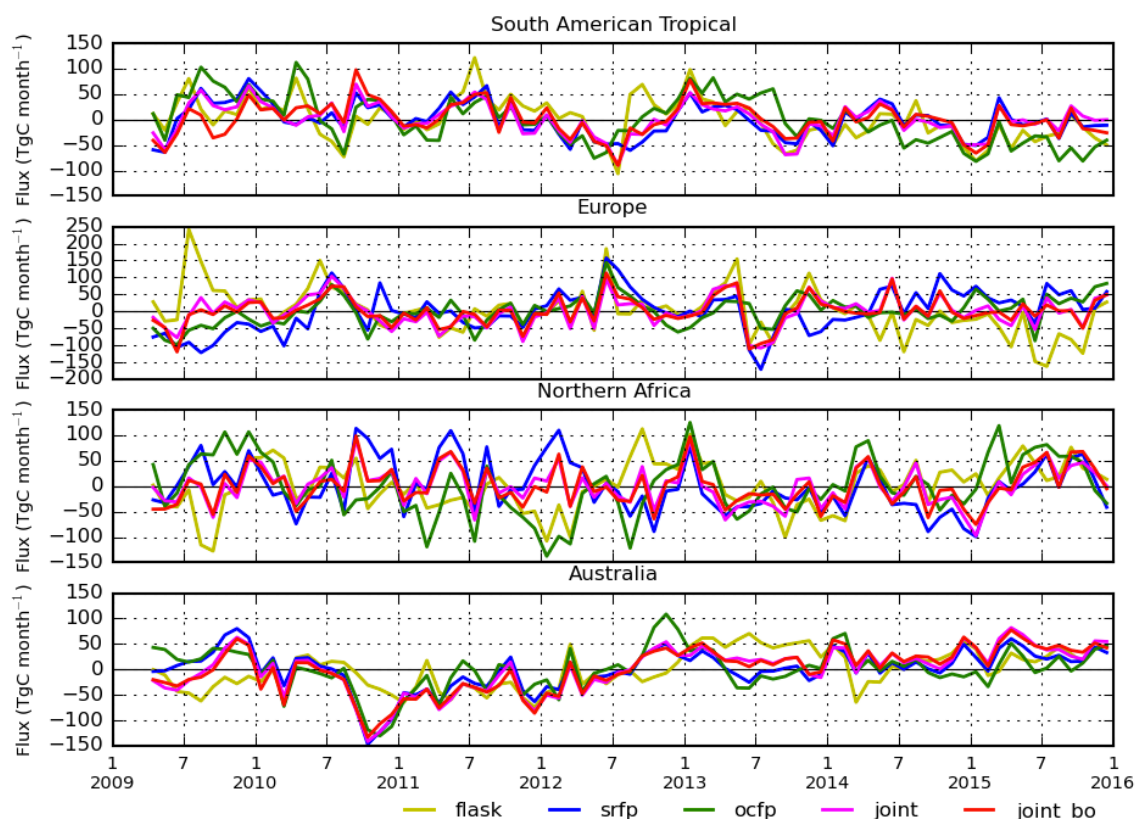



Figure 25. Inter Annual Variability (IAV) of inferred natural CO₂ fluxes for 5 different TransCom land regions. The IAV is calculated by subtracting the average monthly flux over the September 2009 – September 2015 period from monthly values. In the sign convention, positive fluxes correspond to a higher net carbon source into the atmosphere compared to the rest of the period.

Due to these findings, we conclude that *at current stage* the reliability of our absolute inverted fluxes using the XCO₂_GOS_OCFP and XCO₂_GOS_SRFP data is rather low. Reliability of absolute fluxes improves for the joint inversions, combining XCO₂_GOS_SRFP satellite data and surface flask measurements with (*joint bo*) and without (*joint*) a bias optimization. While the interpretation of absolute fluxes are sometimes problematic, some of the inter annual and inter seasonal signals found in the inverted fluxes are more robust and provide interesting findings with respect to the carbon cycle that are in line with several recent studies (e.g. Gatti et al., 2014; Poulter et al., 2014).

3.6. Inversion experiments with the IUP system

3.6.1. The regional flux inversion system used by IUP

The following short description of the inversion system has been adapted from Reuter et al. (2014). The IUP regional surface flux inversion system uses only satellite measurements within the European Transcom3 region (from the Atlantic to the Urals, area = 10¹³m²), thus ensuring that any potential

	ESA Climate Change Initiative (CCI)	Page 46
	Climate Assessment Report (CAR)	
	for the Essential Climate Variable (ECV) Greenhouse Gases (GHG)	Version 4 (final)
		28 March 2017

retrieval biases in other regions do not impact on the results. Taking a transport model and the retrieval averaging kernels into account, we analyze the differences between some prior flux field (from CarbonTracker CT2016, Peters et al. 2007, or CAMS v15r4) and XCO₂ retrieved from the satellite radiances. For each sounding, we compute the accumulated European surface influence function (Jacobian) by using the Stochastic Time-Inverted Lagrangian Transport model (STILT, Gerbig et al. 2003). Potential issues arising from long-range transport are reduced because air masses leave the analysis region typically within a few days. If the XCO₂ difference to the background model depends on the European surface influence, we infer by how much the background model fluxes (being the basis for its concentrations) would have to be modified in order to bring measurement and model in better agreement. As an example, if the XCO₂ difference (satellite minus model) decreases with increasing surface influence, the model fluxes can be assumed to be too large. A systematic offset is interpreted as retrieval (or model) bias. This results in the inversion being solely dependent on regional (medium-scale) gradients, which could be a strength of the satellite retrievals. The inversion yields monthly optimized fluxes and utilizes the optimal estimation formalism with the background model fluxes as a priori and first guess. As the used prior fluxes assimilated surface in situ measurements, the IUP regional inversion can be considered to be a simplified stepwise inversion of satellite and surface in situ measurements. For more details, see Appendix A of Reuter et al. (2014).

3.6.2. European fluxes derived from CRDP#4 data sets

Analogously to the analyses of Reuter et al. (2014), an ensemble of inversion experiments has been set up for XCO₂_SCI_BESD, XCO₂_GOS_SRFP, and XCO₂_GOS_OCFP. These authors identified (beside the satellite retrieval algorithm) the prior CO₂ fluxes and the meteorological data as most important driver for differences in their inversion results. For this reason, we here analyzed an ensemble consisting of each combination of three satellite data sets, two prior CO₂ flux types (CT2016 and CAMS v15r4), and two meteorological data sources (ERA Interim and NCEP) spanning the years 2003 till 2013.

For the CT2016 runs, we estimated the a priori flux uncertainties from scaling the CarbonTracker reported flux uncertainties by 1/3 and assuming an a priori error correlation length of three months. For the CAMS v15r4 runs, we assumed that the annual flux uncertainty always amounts 0.15GtC/yr (which is a typical value for the CAMS in situ flux inversion) and constructed a corresponding monthly a priori error covariance from the assumptions of error correlations of three months.

For GOSAT, the XCO₂ measurement uncertainties have been used as provided in the L2 data products and then scaled to match the scatter derived from the XCO₂_EMMA validation (1.00 for XCO₂_GOS_OCFP and 1.35 from XCO₂_GOS_OCFP). No sounding-to-sounding error correlations have been assumed.

For SCIAMACHY, we computed for each month the full spatio/temporal error covariance as described in the data product and by Reuter et al. (2017). Longer temporal error correlations have been neglected as the inversion system is allowed to fit a monthly constant bias term.

The main inversion results of annual and monthly fluxes are shown in Figure 26 which also shows the used a priori fluxes from CT2016 and CAMS v15r4. Averaged over all years, XCO₂_SCI_BESD sees the strongest sink signal followed by XCO₂_GOS_SRFP; XCO₂_GOS_OCFP sees the weakest sink (or even a source).

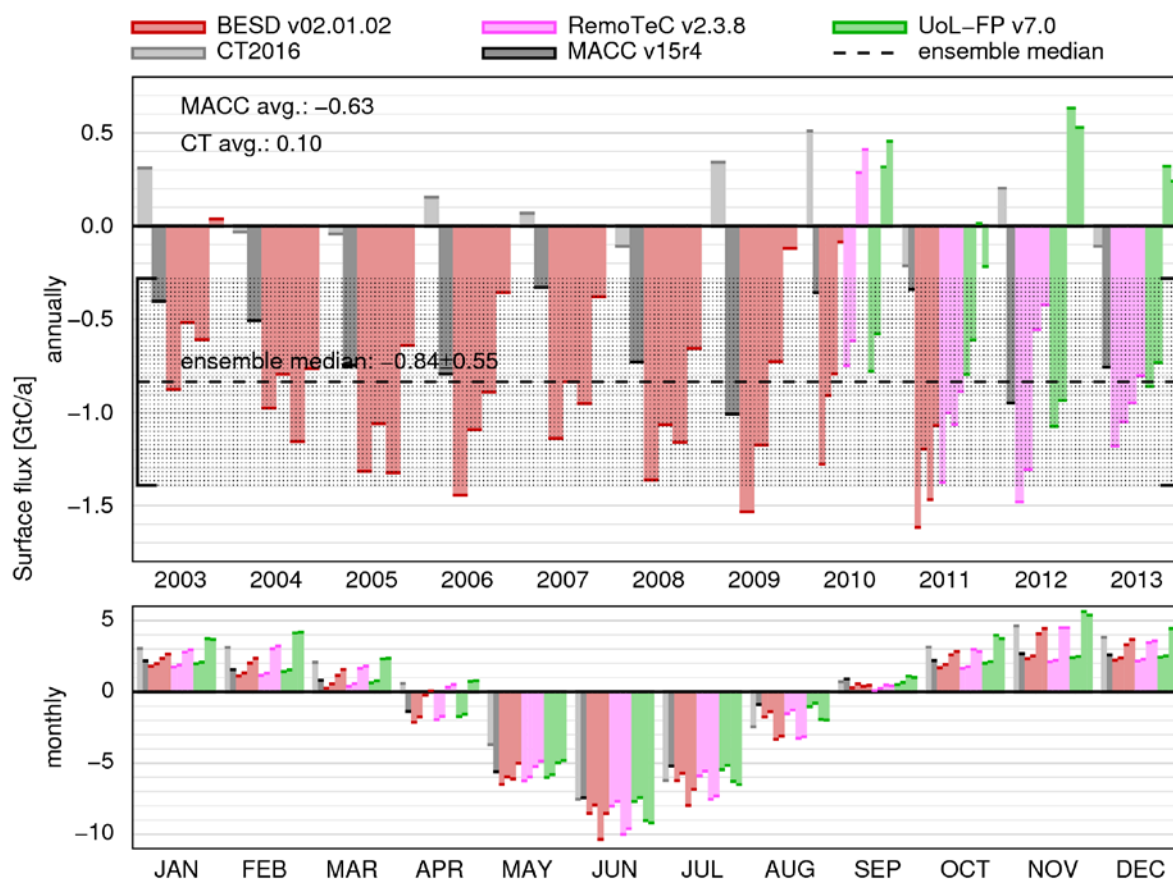



Figure 26. European annual (top) and average monthly (bottom) biospheric fluxes derived from XCO₂_SCI_BESD (red), XCO₂_GOS_SRFP (pink), and XCO₂_GOS_OCFP (green) as well as biospheric CAMS v15r4 (dark gray) and CT2016 (light gray) fluxes derived from surface in situ measurements. Each group of four bars represent (from left to right) inversions based on i) ERA Interim meteorology and CAMS as prior fluxes, ii) NCEP meteorology and CAMS as prior fluxes, iii) ERA Interim meteorology and CT2016 as prior fluxes, iv) NCEP meteorology and CT2016 as prior fluxes. The ensemble median and the standard deviation have been computed from all individual years, retrieval algorithms, and combinations of background model and meteorology.

The ensemble overall median flux amounts to 0.84GtC/yr which is similar to 0.95GtC/yr (2003-2010) obtained by Reuter et al. (2014). However, these authors estimated the ensemble spread (in 2010) to be 0.30GtC/yr which is considerably less than an ensemble standard deviation of 0.55GtC/yr derived here. It shall be noted that these numbers have been computed differently: one the one hand side,

	ESA Climate Change Initiative (CCI)	Page 48
	Climate Assessment Report (CAR)	
	for the Essential Climate Variable (ECV) Greenhouse Gases (GHG)	Version 4 (final)
		28 March 2017

Reuter et al. (2014) used more retrieval algorithms for their ensemble and also more inversion experiments which adds variance; on the other hand, they used only one year to compute the ensemble spread which removes variance because of the missing year-to-year variability compared to this study.

Validation activities and results from XCO₂_EMMA (Buchwitz et al. 2017a) suggest that all retrieval algorithms improved and somewhat converged (i.e., got more similar) from version-to-version. Despite this, the algorithm-to-algorithm differences of the performed inversions seem to have increased. This is most prominently the case for the years 2012 and 2013 when using CT2016 as background model.

However, the largest contribution to the increased ensemble spread comes from the large differences in the fluxes of the used CO₂ background models CT2016 (a source of 0.10GtC/yr, 2003-2013) and CAMS v15r4 (a sink of 0.63GtC/yr, 2003-2013). As visible in Figure 26, the differences are most prominent in the dormant season when the satellite retrievals are essentially “blind” in large parts of Europe and the used a priori fluxes get a strong weight. Apparently, the XCO₂_GOS_OCFP inversions seem to be most sensitive to the used prior fluxes (see, e.g., 2012 and 2013).


3.6.3. Conclusions

Results from a regional ensemble inversion similar to that of Reuter et al. (2014) comprising eleven years (2003-2013), three retrieval algorithms (XCO₂_SCI_BESD, XCO₂_GOS_SRFP and XCO₂_GOS_OCFP), two CO₂ prior flux types (CT2016 and CAMS v15r4), and two meteorological data sources (NCEP and ERA Interim) suggest that the terrestrial European biosphere takes up 0.84 ± 0.55 GtC/yr. This result is in agreement with the estimates of Reuter et al. (2014) and with CAMS v15r4 inverting in situ observations only. Compared to the results of Reuter et al. (2014), the ensemble spread has increased which can in large parts be attributed to the considerable differences between CT2016 and CAMS v15r4 fluxes especially during the dormant season. Additionally to this, the inversion results seem to vary more from one algorithm to another which was not expected because the validation activities and results from XCO₂_EMMA (Buchwitz et al., 2017a) suggest that all retrieval algorithms improved and somewhat converged.

3.7. Assimilation of XCO₂ into a terrestrial vegetation model by iLab

3.7.1. Introduction

The inverse modelling calculations presented in Sections 3.3, 3.4, and 3.5 are based on the inversion of atmospheric transport models (direct flux inversion, see, e.g. Enting, 2002) by directly solving for a flux field that achieves the best possible fit to XCO₂ products in a transport model run. The high dimension of the unknown flux field – in combination with the diffusive nature of atmospheric transport – renders the inverse problem posed by pure transport inversions particularly underdetermined, and therefore it has to be regularised through prior information. The posterior

	ESA Climate Change Initiative (CCI)	Page 49
	Climate Assessment Report (CAR)	
	for the Essential Climate Variable (ECV) Greenhouse Gases (GHG)	Version 4 (final)
		28 March 2017

uncertainty of the derived flux fields thus depends to a large extent on prior information, in particular the covariance of prior uncertainty. In the examples presented in Sections 3.3, 3.4, and 3.5, the degrees of freedom are reduced through assumed covariance of prior uncertainty of fluxes over neighbouring grid cells and subsequent time steps.


In CCDAS, by contrast to flux inversions the assimilation of observations into a terrestrial vegetation model is based on a coupled vegetation-transport model, in which the transport model takes the role of an observation operator linking simulated net surface fluxes to simulated XCO₂. As in transport inversions, the assimilation can be formulated as an inverse problem, but the task is not to optimise a flux field directly, but the model trajectory. The best way to select the unknowns of this inverse problem is to choose the most uncertain values that enter the coupled model simulation. For terrestrial biosphere simulations on climate time scales, the focus is on the model process parameters because these are typically empirical parameters rather than fundamental physical constants (see, e.g. Kaminski et al. 2012, 2013). The primary task of carbon cycle data assimilation is, hence, the calibration of the biosphere model at the core of CCDAS. Target quantities of interest such as surface fluxes are simulated by running the calibrated terrestrial model forward.

This study assesses two ECV core algorithm products of the GHG-CCI Climate Research Data Package (CRDP#4) namely XCO₂_SCI_BESD, version 2.01.02 (updated data set with same version number), and XCO₂_EMMA, version 2.2c, and their use in iLab's CCDAS. Combining these two products with CCDAS, we derive sets of CCDAS-L4 flux products on a 0.5 degree spatial and monthly temporal resolution, which include per-pixel uncertainty ranges consistent with the uncertainty reported in the L2 XCO₂ input products. The products we provide are the terrestrial Net Primary Productivity (NPP), heterotrophic respiration (R_{het}), and Net Ecosystem Productivity (NEP).

3.7.2. Method

The terrestrial biosphere model included in the CCDAS used for this study is conceptionally similar to the one used by Kaminski et al. (2002). The model operates on a 0.5 degree global grid and as Knorr et al. (2014) divides the global terrestrial biosphere into eight land cover classes characterised by the dominance of certain plant functional types (PFTs), based on the MODIS land cover classification (Friedl et al., 2010): (1) cropland/urban/natural vegetation mosaic, (2) needleleaf forest, (3) broadleaf forest, (4) mixed forest, (5) shrubland, (6) savanna or grassland, (7) tundra, (8) barren or sparsely vegetated.

The model calculates the uptake of CO₂ by photosynthesis using a light-use efficiency approach. Heterotrophic (i.e. soil except root) respiration is calculated following a Q₁₀ functional relationship with temperature. Both R_{het} and photosynthesis are modulated by a water stress factor. The model requires global fields of temperature, FAPAR and the water stress factor as driving data. The temperature fields are taken from the CRU data set (Harris et al., 2013) and the water-stress factor, taken as AET/PET (actual divided by potential evapotranspiration, Knorr and Heimann 1995), is computed with the BETHY model of Knorr (2000). As further drivers for the photosynthetic activity, the model uses the FAPAR product derived by JRC-TIP (Pinty et al., 2007). The FAPAR product was

	ESA Climate Change Initiative (CCI)	Page 50
	Climate Assessment Report (CAR)	
	for the Essential Climate Variable (ECV) Greenhouse Gases (GHG)	Version 4 (final)
		28 March 2017

derived by running JRC-TIP after aggregation of its white sky broadband albedo input to the 0.5 degree² resolution (Kaminski et al., 2016). Besides its high spatial resolution of 0.5 degree, the advantage of using this model lies in using the TIP-FAPAR product as additional EO data stream to drive the model. The FAPAR product was derived by running JRC-TIP after aggregation of its white sky broadband albedo input to the 0.5 degree resolution (Kaminski et al., 2016).

The observation operator for XCO₂ used in this study is the atmospheric transport model TM3 (Heimann and Körner, 2003), operated on its fine grid, i.e. in approximately 4×5 degree² horizontal resolution on 19 vertical levels. The model is approximated by a Jacobian that resolves flux impacts up to three months before an observation on the full model grid, from four to 48 months before an observation on 12 zonal bands and from fluxes ingested more than 49 months before an observation by a globally uniform contribution. The coupled model is run from 2006-2010, and the monthly mean 2010 XCO₂ simulation constitutes the observation equivalent in our assimilation experiments.

CCDAS (Rayner et al., 2005, Kaminski et al. 2013) operates through minimisation of a cost function that achieves a balance between the observational constraints and the prior information. As it is the case for the atmospheric inversion systems of Sections 3.3, 3.4, and 3.5, the minimum is determined by varying a *control vector*, in this case a vector of biosphere model parameters and the initial atmospheric CO₂ field.


After minimisation, uncertainty estimates for the simulated target quantities (carbon and water fluxes) are derived in a two-step procedure. In a first step, a second derivative (Hessian) approximation of the cost function is used to approximate the inverse of the posterior uncertainty covariance matrix for the control vector. It quantifies the uncertainty ranges of the control variables that are consistent with the uncertainty ranges of the observations, as well as the model. In the second step, the uncertainty in control space is propagated to the uncertainty in a given target quantity through the linearised model.

In this set of inversions, we focus on the effect of the uncertainty in the different observational data sets. We therefore deliberately neglect contributions from both uncertainties in the formulation of the terrestrial biosphere model, and the atmospheric transport model. The resulting flux uncertainty estimates must therefore be considered to be at the lower end.

3.7.3. Preparation of observational data sets and setup

For the purpose of this assessment, product XCO₂_SCI_BESD was aggregated to monthly mean XCO₂ values on the TM3 grid. The uncertainty of this aggregated product depends on the uncertainty correlation, which is not reported with the product. Reuter et al. (2016b) provide, however, two estimates of the uncertainty covariance:

1. A parametrisation of a so-called full error covariance approximation. This is our default case for the BESD product and we will denote it as **BESD**.
2. The heuristic formula

	ESA Climate Change Initiative (CCI)		Page 51
	Climate Assessment Report (CAR)		
	for the Essential Climate Variable (ECV) Greenhouse Gases (GHG)		Version 4 (final)
			28 March 2017

$$\sigma_{\text{obs}} = 1.91 / \sqrt{n} + 0.39 \text{ ppm}$$

where 1.91 corresponds to the (random) single sounding uncertainty, 0.39 to the systematic uncertainty and n to the number of samples in the given month and grid cell. In the following we will denote this case as “**BESD heuristic**”.

For both cases uncertainty correlations between two grid boxes or months are ignored.

Likewise there is no uncertainty correlation reported for the XCO₂_EMMA product. Here we also use two different uncertainty specifications.

1. For our default case **EMMA** we use the uncertainty specified in the product (σ_{prod}^2).
2. For our case **EMMA spread** we exploit a unique property of the EMMA product, namely that it does not only provide the median of the ensemble of retrieval products together with the uncertainty estimate specific to the respective retrieval algorithm, σ_{prod} , but also the spread over the ensemble members σ_{spread} . We calculate the total observational uncertainty by combining the product uncertainty and the spread between the retrieval algorithms:

$$\sigma_{\text{obs}} = \sqrt{\sigma_{\text{prod}}^2 + \sigma_{\text{spread}}^2}$$

While the first term is the result of an uncertainty propagation through the retrieval algorithm (i.e. intrinsic to the algorithm), the second term is used to approximate the uncertainty from errors in the retrieval algorithm. For the aggregation to monthly mean XCO₂ values on the TM3 grid we assume fully correlated uncertainties for all data points that lie within a given TM3 grid cell and month, and assume no correlation between data points in two different grid boxes or months.

In the aggregation, grid cells and months with less than 10 valid data points were neglected. For the year 2010 this yields 2158 monthly mean observations for EMMA, and 3623 for BESD.

We perform a separate assimilation experiment for each of the four cases. For each experiment, we perform three minimisations from different starting points, one from the prior control vector, one with each element of the control vector increased by 30% and one with each element reduced by 30%.

For validation, we use data of monthly mean atmospheric CO₂ concentrations compiled by Keeling et al. (2001) from flask samples of the Scripps Institution of Oceanography (SIO) network. We use only the seven stations for which monthly mean values for 2010 were available from both the SIO network, and from the Carbon Cycle Cooperative Global Air Sampling Network of the National Oceanic and Atmospheric Administration's (NOAA) Earth System Research Laboratory (ESRL).

3.7.4. Evaluation

In each of the four experiments all three minimisations converged to the same minimum, which gives some confidence in having identified the respective global minima. We first discuss the results of our two default cases BESD and EMMA before we analyse the impact of the uncertainty specification using the results of the other experiments. In each of the four experiments all three minimisations converged to the same minimum, which gives some confidence in having identified the respective global minima.

Figure 27 shows the RMSE of the fit of simulated posterior XCO₂ concentrations to the BESD or EMMA product on the TM3 grid, i.e. against the data sets we assimilated. Except for the high latitudes of the northern hemisphere, some coastal grid cells and three distinct regions, the RMSE values for BESD (right hand panel) vary around 1 ± 0.8 ppm. The three regions that consistently exhibit larger RMSE values (around 2.5 ppm with some >4 ppm) are Amazonia, the central tropics of Africa and Southeast Asia. The fit to the EMMA product (see left hand panel) is much better, except for a few coastal grid cells. However, the RMSE values for the EMMA product are also consistently higher in Amazonia and Tropical Africa than for other regions, but with considerably smaller RMSE values of around 2 ppm. For the Maritime Continent there are no observations during July 2010 in EMMA.

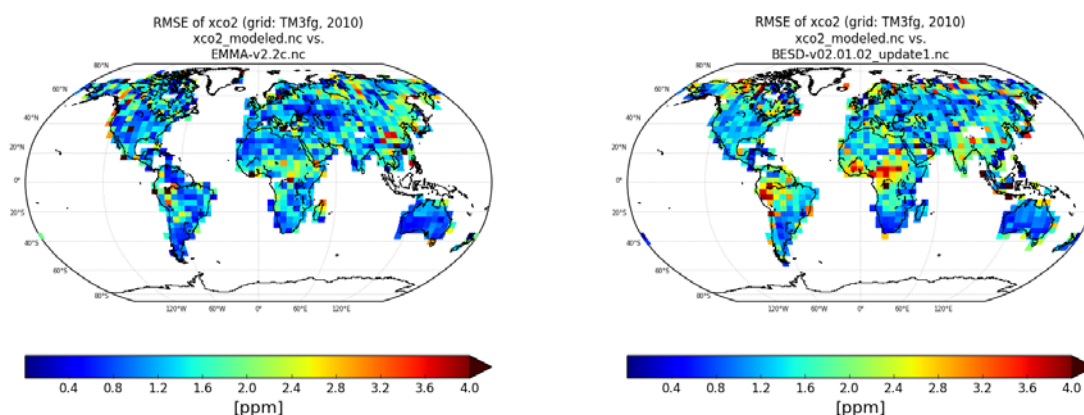


Figure 27. RMSE of the fit of simulated 2010 posterior XCO₂ concentration to the EMMA (left) and BESD (right) products.

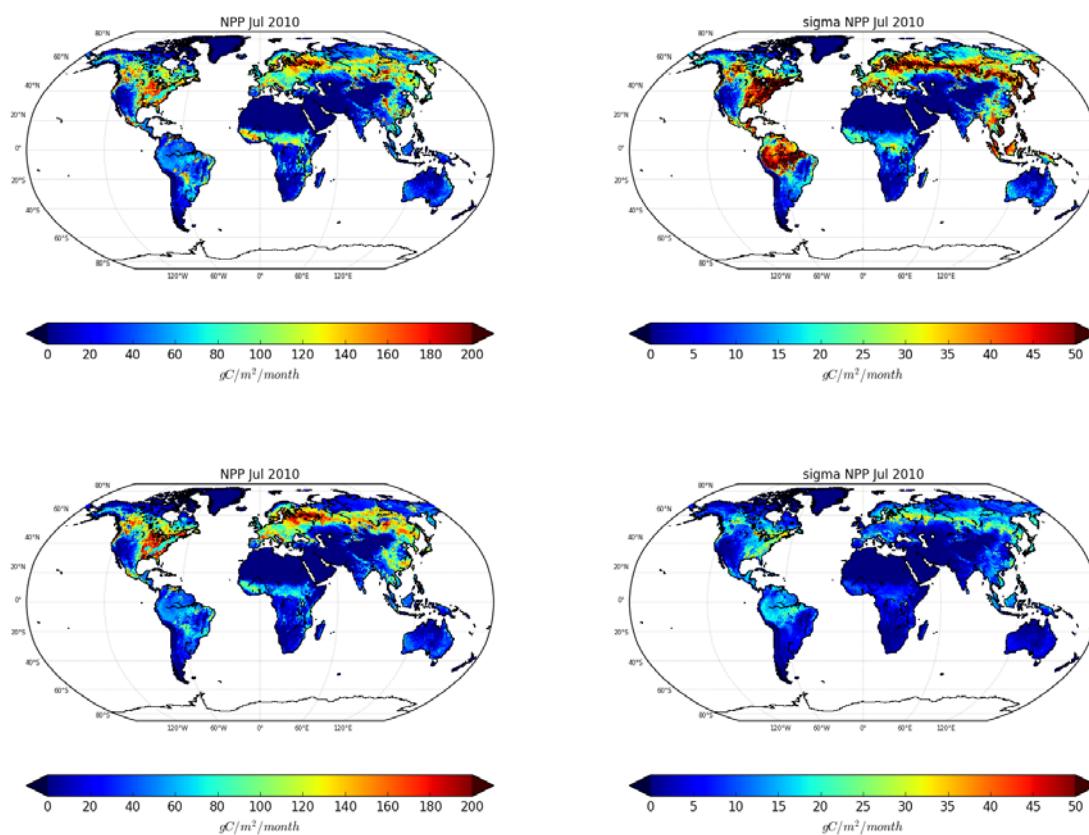


Figure 28. Posterior July 2010 NPP (left) and the 1-sigma uncertainty range (right) for cases "EMMA" (upper row) and "BESD" (bottom row).

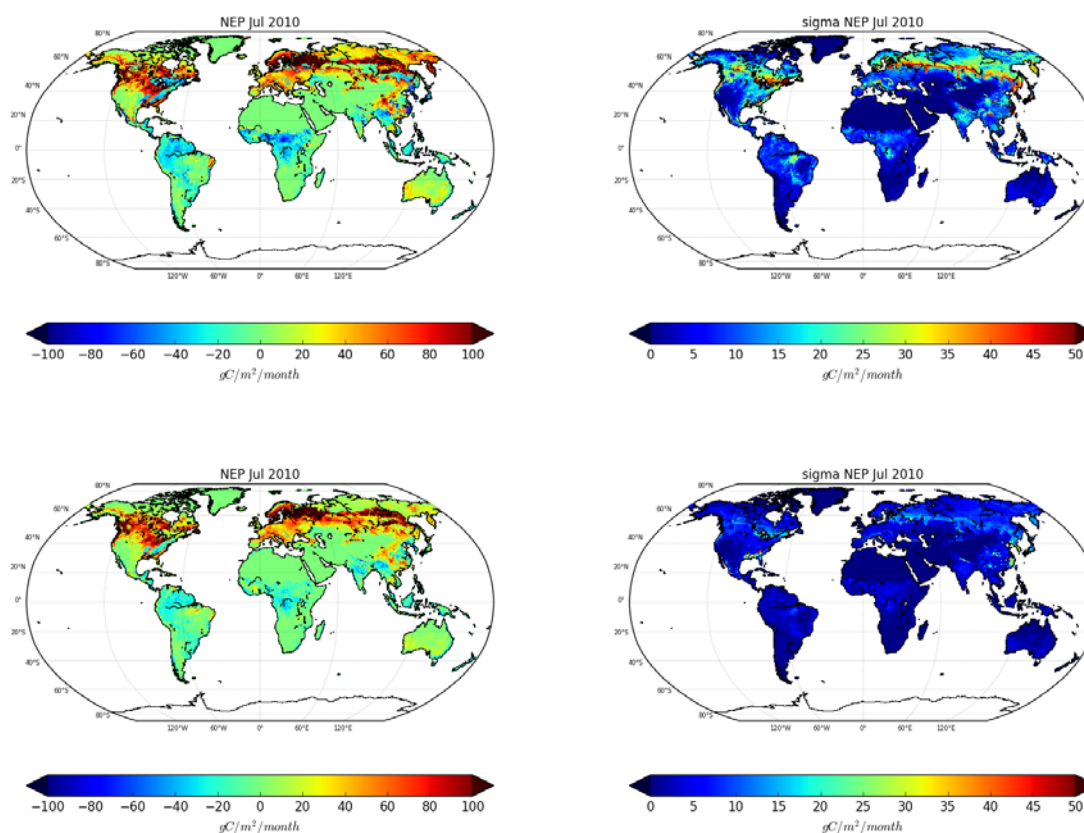


Figure 29. Posterior Juli 2010 NEP (left) and the 1-sigma uncertainty range (right) for cases "EMMA" (upper row) and "BESD" (bottom row).

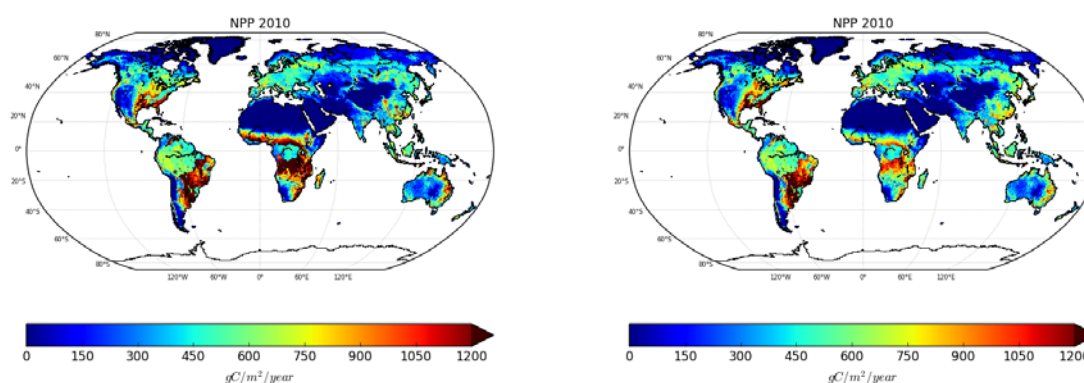



Figure 30. Posterior 2010 NPP for EMMA (left) and BESD (right).

Of the fluxes calculated by the biosphere model, in the following we show only NPP and NEP, while Rhet can be derived from $R_{het} = NPP - NEP$. As an example, we present the two fluxes and their posterior per-pixel uncertainty estimates for July 2010 on the model's 0.5° grid. In order to aid

	ESA Climate Change Initiative (CCI)	Page 55
	Climate Assessment Report (CAR)	
	for the Essential Climate Variable (ECV) Greenhouse Gases (GHG)	Version 4 (final)
		28 March 2017

comparison, we use the same colour scale in all the following figures (except for difference plots), while occasional values beyond this scale are displayed in black colour. Figure 28 shows NPP and Figure 29 shows NEP.

For BESD (Figure 28, lower panel) we find a characteristic band in the northern latitudes of high productivity during the summer (North America, Europe and Russia). The African Savannas and Southeast Asia also show high productivity in July as expected. Also as expected, the Southern latitudes ($>20^{\circ}\text{S}$) are areas of low productivity in July due to the southern-hemisphere winter. The tropical regions, however (South America, central Africa and the Maritime Continent), turn out less productive than expected (see for instance Kicklighter et al, 1999), with values of less than $80 \text{ gC/m}^2/\text{month}$. Compared to BESD the NPP derived from EMMA is slightly higher over some areas, such as the African Northern tropics/Savanna and the Northern hemisphere high latitudes, especially in Northeast Siberia. The remarkably low NPP in South America, central Africa and the Maritime Continent tropical regions is, however, similar to the BESD cases. The regions of high productivity also show higher posterior uncertainty, with considerably higher values ($>50 \text{ gC/m}^2/\text{month}$) for EMMA.

The results for the net exchange flux (NEP, net CO_2 uptake) for EMMA and BESD are displayed in Figure 29. For BESD (lower panel), the terrestrial sink with values of around 40 to $80 \text{ gC/m}^2/\text{month}$ (peaking at more than $100 \text{ gC/m}^2/\text{month}$) is mostly located in the Northern latitudes (north of 40°N), following the NPP pattern of high productivity. Tropical areas tend to be CO_2 sources to the atmosphere in July. Quite remarkable are the large source areas in the African Northern tropics/Savanna, which correspond to an area of rather high NPP (see Figure 28, top and middle row). The EMMA case shows somewhat more structure in NEP as compared to BESD. The African and South American tropics are a larger source, especially the African regions with source values of up to $80 \text{ gC/m}^2/\text{month}$. There is, in contrast to BESD, a small source area of CO_2 (around $50 \text{ gC/m}^2/\text{month}$) along the East coast of the US. Also, the EMMA case shows a larger atmospheric sink of CO_2 over Australia, compared to BESD, with about $30 \text{ gC/m}^2/\text{month}$. The posterior uncertainty in NEP shows much more widespread areas with higher posterior uncertainty in the Northern latitudes (larger than $40 \text{ gC/m}^2/\text{month}$) in the EMMA case than in the BESD case. The CO_2 source region along the US East coast, however, is among regions with the highest uncertainties in EMMA.

The structure in the spatial distribution of annual NPP for 2010 (Figure 30) is rather similar between the BESD and EMMA cases, and compares reasonably well to other model results for NPP (see, e.g., Cramer et al., 1999), with the exception of the tropical regions, as already noted for the July 2010 NPP. Here, we see a general shift of what is normally considered to be the most highly productive regions in the central tropics (around the equator) to their surrounding savanna, grassland and seasonal woodland areas (from the central Amazon basin to southeastern Brazil, Paraguay, Uruguay and parts of Argentina, from the Congo Basin to northern Angola, Zambia and Mozambique). The difference between EMMA and BESD is found less in the spatial patterns but rather in the overall magnitude of annual NPP, with considerably higher values in the EMMA case especially for the southern Africa region. The reduced NPP in the central tropics has consequences for the net exchange fluxes (NEP) in these regions as explained below.

The most prominent feature in NEP (Figure 31) is the tropical regions being a large source of CO₂. This source is present in both cases, but for EMMA this tropical source reaches values above 300 gC/m²/year, especially in the greater Amazonas region, much more pronounced than in the BESD case (~200 gC/m²/year). The high latitudes (>60 degrees N) are a source region, and the extra-tropical mid latitudes (>20 degree N) are strong sink regions. The strong tropical source in the Amazonas region is somewhat countered by large uptake fluxes in South American savanna and grassland regions further south-west (apparent in both cases). The most remarkable difference between EMMA and BESD is the much stronger sink over Australia in the EMMA case. Since the NPP over Australia is very similar in the EMMA case compared to the BESD case, this means that the heterotrophic respiration is much smaller in the EMMA case than in the BESD case. The difference in the posterior NEP between the two cases is shown in Figure 32. Besides the above mentioned difference over Australia there is also a distinct contrast in the tropical NEP especially in tropical Africa where EMMA produces a much larger source than BESD with a difference of up to 300 gC/m²/year (similar in size as over Australia but different in sign).

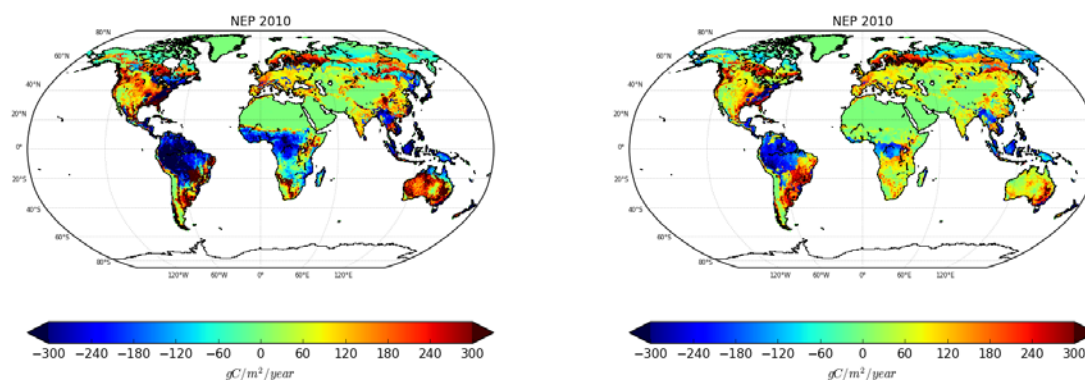


Figure 31. Posterior 2010 NEP for EMMA (left) and BESD (right).

As a validation exercise, we compare the simulated posterior monthly mean atmospheric CO₂ concentrations against observations from flask measurement stations. Figure 33 shows the results for seven different stations for both minimisations, as well as for a model simulation using the prior parameter values. As a rough indication of the uncertainty in these monthly means we plot two error bars. The first uses the difference to the monthly mean concentrations provided by the ESRL (Dlugokencky et al., 2016). The second is the standard deviation from a spline fit (Keeling et al., 2001). For all seven stations there is a clear improvement in the fit against the observations in the amplitude as well as the seasonality for both experiments compared to the prior. The differences in the simulated atmospheric CO₂ concentrations between the EMMA and BESD cases are rather small and there is no indication that one experiment fits the observations better than the other. The match of the large summer draw-down at the northern stations ALT and BRW is notoriously difficult to achieve (Heimann et al., 1998). Part of the mismatch in the second half of the year at SPO – which is highly sensitive to

the southern ocean – may reflect errors on our ocean background field (which is not influenced by our control variables).

We use the comparison between the two BESD cases (BESD and BESD heuristic) to assess the effect of switching between two plausible specifications for the uncertainty correlation. For the year 2010, the two cases yield large differences in NEP in the South American tropics (Figure 32, bottom left). These differences are comparable to the differences in the flux estimates derived from the two default data sets (EMMA versus BESD, see upper panel of Figure 32). For the Amazonas region, the difference between BESD and BESD heuristic is of the same size than the difference between EMMA and BESD. In other parts of the globe (e.g. Northern Australia) the difference between BESD and BESD heuristic reaches the magnitude of NEP itself. As the only difference in these two data sets (BESD and BESD heuristic) are the assumed uncertainty correlations (restricted to the scale of the TM3 grid cells and monthly intervals), these results highlight the importance of providing appropriate uncertainty correlations together with the XCO₂ products.

We use the comparison between the cases EMMA and EMMA spread to quantify the effect of adding an additional uncertainty component to the one reported with the EMMA product, in this case a component that reflects errors in the retrieval systems (σ_{spread} , see above). The increase in uncertainty somewhat reduces the source in the African tropics and the Maritime Continent, while the sink over Australia hardly changes (Figure 32, bottom right). Overall the effect of including the additional uncertainty is slightly smaller than that of switching between the two uncertainty correlation estimates use used for the BESD product.

**Climate Assessment Report (CAR)**for the Essential Climate Variable (ECV)
Greenhouse Gases (GHG)Version 4
(final)

28 March 2017

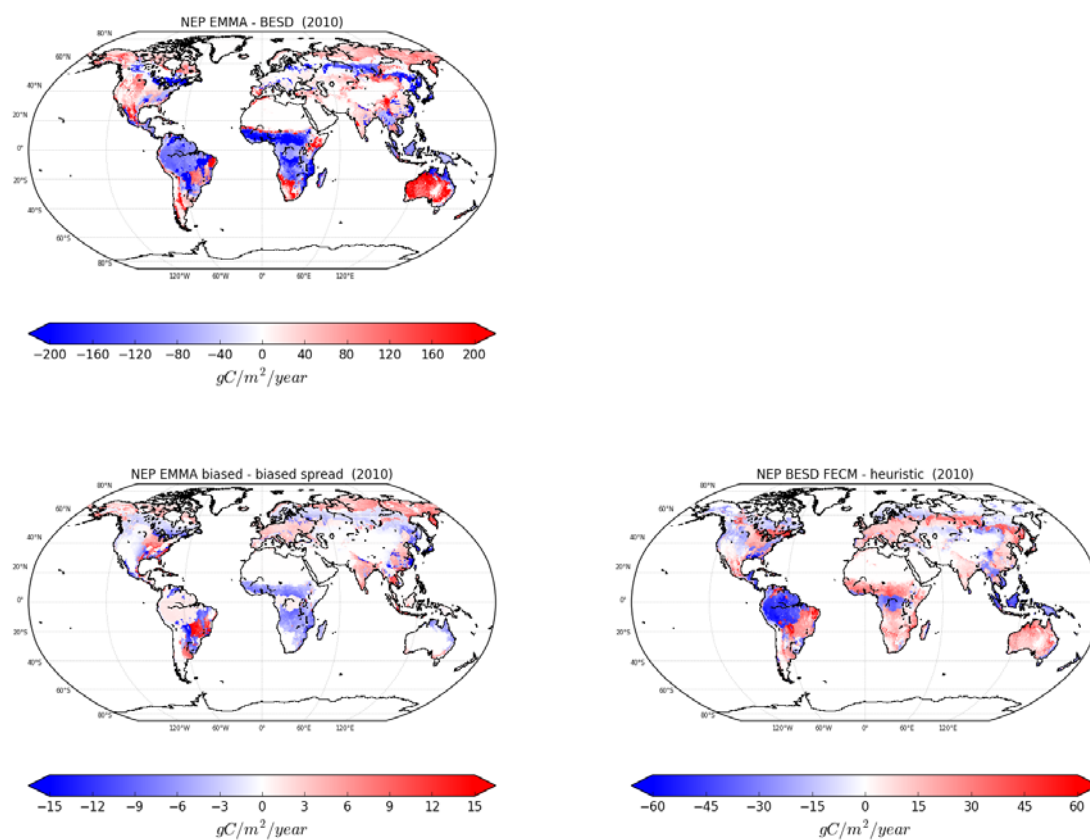


Figure 32. Posterior 2010 NEP difference “EMMA-BESD” (upper panel), “EMMA- EMMA spread” (bottom left) and “BESD – BESD heuristic” (bottom right).



Climate Assessment Report (CAR)

for the Essential Climate Variable (ECV)
Greenhouse Gases (GHG)

Version 4
(final)

28 March 2017

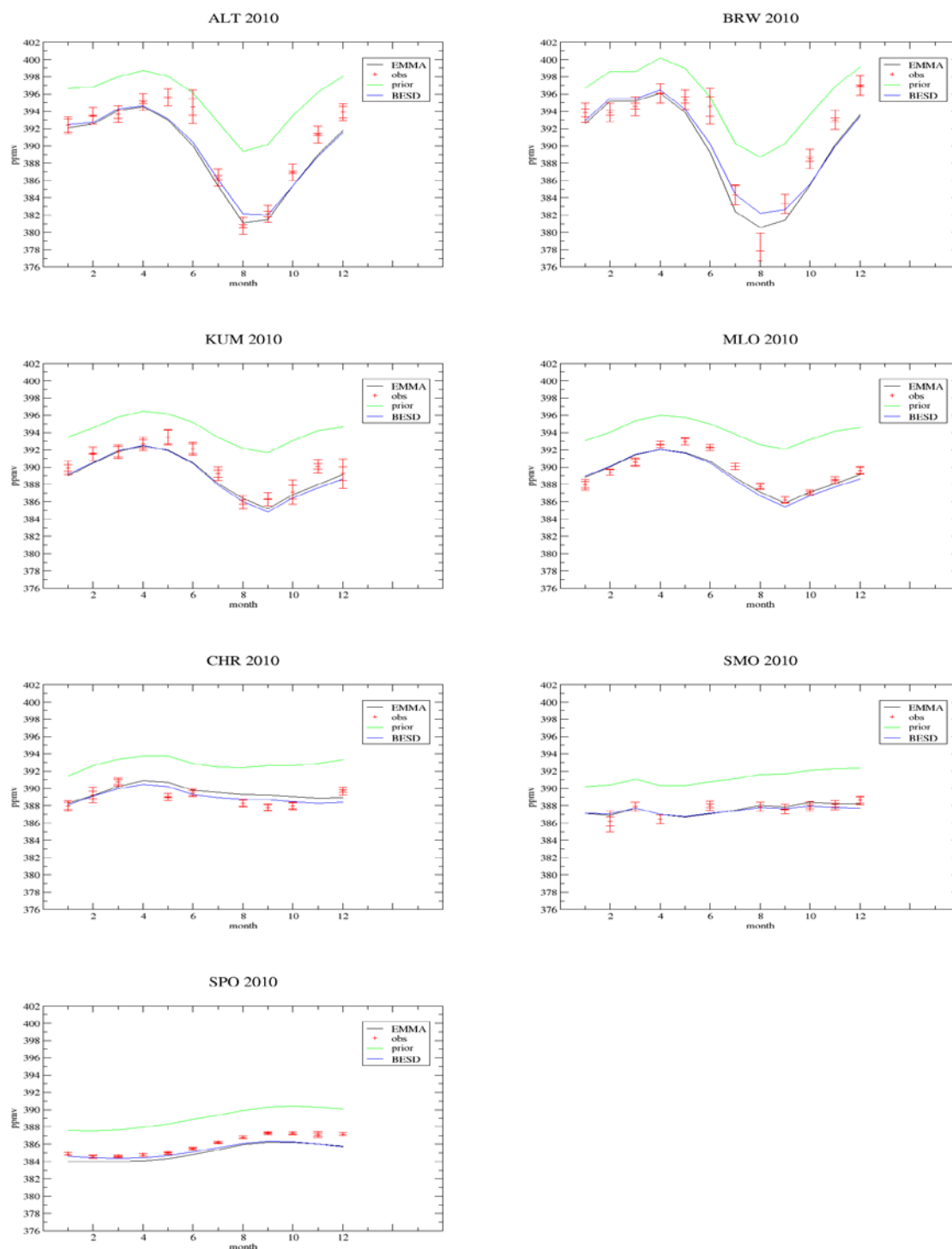



Figure 33. Monthly mean CO₂ concentration in ppm; observed (red), prior (green), posterior after assimilation of EMMA (black), posterior after assimilation of BESD (blue) at ALT (top-left), BRW (top-right), KUM (second row, left), MLO (second row, right), CHR (third row, left), SMO (third row, right), and SPO (bottom-left)

	ESA Climate Change Initiative (CCI)	Page 60
	Climate Assessment Report (CAR)	
	for the Essential Climate Variable (ECV) Greenhouse Gases (GHG)	Version 4 (final)
		28 March 2017

3.7.5. Conclusions

We presented two novel level 4 products derived from the BESD and EMMA CRDP#4 XCO₂ ECV products, retrieved from SCIAMACHY and GOSAT observations, respectively. These products consist of net and gross surface fluxes of carbon dioxide on a global 0.5 degree² grid and are provided with lower-bound per-pixel uncertainty ranges. Assumptions on uncertainty correlation have a considerable impact on the inferred flux fields (~60 gC/m²/year), stressing the importance of documented uncertainty correlation in XCO₂ products. Adding an uncertainty component that approximates the error in the retrieval system has a slightly smaller effect.

The most prominent feature in the posterior net flux is the tropical source of CO₂ inferred from both products. However, for the EMMA product this source is much more pronounced than for BESD, especially over South America with values of 300 gC/m²/year and higher. This high tropical source confirms the results of the intercomparison study of Houweling et al. (2015), which was based on transport inversions using GOSAT data. The CCDAS attributes the larger net flux to increased heterotrophic respiration. Our CCDAS comprises a validation framework that compares the atmospheric carbon dioxide concentration observed at flask sampling sites against transport model simulations based on the posterior flux fields. For both BESD and EMMA this provides a reasonable overall agreement for the seven sites from the SIO network covering a latitudinal range from 82.5°N to the South Pole.

4. Assessment of satellite-derived XCH₄ ECA data products

4.1. Introduction

In the following we show an assessment of the two ECV SCIAMACHY XCH₄ products and the four ECV core algorithm GOSAT XCH₄ products of the GHG-CCI Climate Research Data Package (CRDP#4, http://www.esa-ghg-cci.org/sites/default/files/documents/public/documents/GHG-CCI_DATA.html) by inverse modelling experiments made by JRC and the University of Edinburgh (UoE). The products are listed in Table 3.

product ID	version	instrument	data availability	CRDP	Evaluators (section)
CH4_SCI_IMAP	v7.2	SCIAMACHY	01/2003-04/2012	CRDP#4	JRC (4.2)
CH4_SCI_WFMD	v4.0	SCIAMACHY	10/2002-12/2011	CRDP#4	JRC (4.2)
CH4_GOS_OCPR	v7.0	GOSAT	04/2009-12/2015	CRDP#4 ECA	JRC (4.2), UoE (4.3)
CH4_GOS_SRPR	v2.3.8	GOSAT	04/2009-12/2015	CRDP#4 ECA	JRC (4.2), UoE (4.3)

CH4_GOS_OCFP	v2.0.2	GOSAT	04/2009-12/2015	CRDP#4 ECA	JRC (4.2)
CH4_GOS_SRF	v2.3.8	GOSAT	06/2009-12/2015	CRDP#4 ECA	JRC (4.2)

Table 3. XCH₄ products evaluated in this report.

4.2. Assessment of XCH₄ ECA products using the JRC inverse modelling system

4.2.1. Method

In a first step, all CRDP#4 XCH₄ ECA products (see Table 3) were analysed by comparison with CH₄ flux inversions which were constrained by surface observations only (see section 4.2.2). In a second step, the four CRDP#4 GOSAT XCH₄ products (Table 3) were inverted (see section 4.2.3 and 4.2.4).

The JRC CH₄ flux inversions were performed using the four-dimensional variational (4DVAR) inverse modeling system TM5-4DVAR described in detail by Meirink et al. [2008] including subsequent further developments described by Bergamaschi et al. [2009; 2010]. The 4DVAR system is based on the off-line transport model TM5 [Krol et al., 2005], driven by meteorological fields from the European Centre for Medium-Range Weather Forecasts (ECMWF) ERA-Interim reanalysis [Dee et al., 2011]. We employ the standard TM5 version, with 25 vertical layers, and apply a horizontal resolution of 6° x 4°.

For the comparison of the two XCH₄ products from SCIAMACHY (for the period 2003-2011) we used the MACC reanalysis inversion 'v10-S1NOAA_ra' (<http://apps.ecmwf.int/datasets/data/macc-ghg-inversions/>; [Bergamaschi et al., 2013]), while for the comparison of the four GOSAT products (for the period 2010-2015) a new inversion series was performed, but with very similar settings as the MACC inversion 'v10-S1NOAA_ra', constrained by surface observations from the NOAA Earth System Research Laboratory (ESRL) global cooperative air sampling network [Dlugokencky et al., 1994, 2003, 2009].

The setup of the GOSAT inversions was similar as described by Bergamaschi et al. [2013] and Alexe et al. [2015]. The column averaged CH₄ dry air mole fractions (XCH₄) from the satellite retrievals are assimilated together with the NOAA surface observations. We apply a polynomial bias correction (second-order polynomial as a function of latitude and month [Bergamaschi et al., 2009]) of the satellite retrievals (XCH₄) in order to achieve optimal consistency with the NOAA surface observations (compensating both for biases in the satellite retrievals and potential systematic errors of TM5 to simulate the vertical gradient correctly, especially in the stratosphere).

We apply the same selection criteria for the available individual valid GOSAT pixels as in Bergamaschi et al. [2013] and Alexe et al. [2015], (1) using only pixels over land between 50°S and 50°N, and (2)

using only those pixels for which the difference between the surface elevation of the GOSAT pixel and the TM5 model surface is smaller than 250 m.


product ID	version	CRDP	inversion
CH4_GOS_OCPR	v7.0	CRDP#4 ECA	S1
CH4_GOS_SRPR	v2.3.8	CRDP#4 ECA	S2
CH4_GOS_SRFP	v2.3.8	CRDP#4 ECA	S3
CH4_GOS_OCFP	v2.0.2	CRDP#4 ECA	S4

Table 4. GOSAT XCH₄ products which were assimilated by JRC, using the TM5-4DVAR inverse modelling system.

4.2.2. Comparison of CRDP#4 XCH₄ products with atmospheric inversions based on surface observations

Figure 34 shows the statistics of the comparisons of the different XCH₄ products with the 3D model fields from the CH₄ flux inversions constrained by surface observations. This overview clearly demonstrates the significantly better agreement of the GOSAT XCH₄ products with model simulations (with standard deviations in the range 12-16 ppb) compared to the SCIAMACHY products, for which the annual standard deviation is in the range 30-50 ppb (SCIAMACHY IMAPv7.2) and 27-80 ppb (SCIAMACHY IMAPv4.0). Compared to the previous SCHIAMACHY IMAP products, however, a major improvement has been achieved regarding the consistency of the time series. While IMAPv7.0 showed a large discontinuity mid-2010, resulting in a shift of XCH₄ by ~20ppb (see CARv2), this discontinuity is no longer directly visible in the longitudinal average differences between XCH₄ retrievals and TM5-4DVAR inversions (Figure 35c). Both SCIAMACHY products still suffer from the pixel degradation end of 2005. However the impact is significantly larger for SCIAMACHY WFMDv4.0 compared to SCIAMACHY IMAPv7.2. Although the variations in annual mean bias are slightly smaller for SCIAMACHY WFMDv4.0 (ranging between 4 and 9 ppb; see Figure 34) compared to SCIAMACHY IMAPv7.2 (ranging between between 3 and 13 ppb), the longitudinal average differences between XCH₄ retrievals and model simulations show larger changes with time for SCIAMACHY WFMDv4.0 compared to SCIAMACHY IMAPv7.2 (compare Figure 35c and Figure 36c). Nevertheless, also for SCIAMACHY IMAPv7.2 the retrieval vs. model XCH₄ differences vary significantly over time (especially during 2006-2008). Probably these patterns do not represent real atmospheric signals (which might have been missed by the surface observation based inversion), but are likely largely an artifact of the retrievals (as these anomalies in the differences coincide with the periods with much higher noise of the retrievals, reflected by the higher standard deviation between retrievals and model simulations (Figure 35d)).

Figure 37-Figure 40 display the time series 2010-2015 of the four GOSAT XCH₄ retrieval products and their comparison with model simulations. The two GOSAT proxy products (CH4_GOS_OCPR v7.0 and

	ESA Climate Change Initiative (CCI)	Page 63
	Climate Assessment Report (CAR)	
	for the Essential Climate Variable (ECV) Greenhouse Gases (GHG)	Version 4 (final)
		28 March 2017

CH4_GOS_SRPR v2.3.8) and the CH4_GOS_SRFP v2.3.8 retrievals show overall relatively consistent patterns over the entire 5 years period. In contrast, CH4_GOS_OCFP v2.0.2, shows significant changes in the longitudinal average differences between XCH₄ retrievals and model simulations (Figure 40). Furthermore, these differences vary significantly also with latitude (especially after 2011). The inconsistency of the time series is visible also in the annual mean statistics (Figure 34), with a jump of the annual mean bias by 7.6 ppb between 2011 (mean bias: -6.2 ppb) and 2012 (mean bias: 1.4 ppb), accompanied by an increase of the standard deviation between retrievals and model simulations by ~2ppb after 2011.

4.2.3. CH₄ flux inversions: assimilated XCH₄

Figure 41 shows the retrieved and assimilated column averaged CH₄ dry air mole fractions (XCH₄) for the four GOSAT products which were inverted (composite average 2010-2015). In general, both the spatial patterns of the XCH₄ retrievals and the average latitudinal XCH₄ gradients are reproduced by TM5-4VAR relatively well. The good consistency between retrieved and assimilated XCH₄ is largely achieved by means of the applied bias correction (as function of latitude and month; shown in the small panels of (Figure 41, second column)), which is required in order to simultaneously assimilate the satellite retrievals and the NOAA surface observations. Previous studies identified some deficiencies of TM5 to simulate the CH₄ gradients in the stratosphere, especially at mid to high latitudes [Bergamaschi et al., 2009; 2013; Alexe et al., 2015]. Hence the bias correction also serves to partly compensate these model shortcomings. However, the calculated bias corrections show significant differences (Figure 41, second column) for the different GOSAT products, which suggest that also at least some of the GOSAT products have some biases (varying with latitude and time). For CH4_GOS_OCFP v2.0.2 the calculated bias correction varies significantly with time, probably largely due to the inconsistency of the timeseries (i.e. time dependent bias) of that product, which was diagnosed already by comparison with the surface observation based inversions (section 4.2.2, Figure 40). Despite the applied bias correction, some small residuals between retrieved and assimilated XCH₄ are visible (Figure 42). The largest residuals are visible for CH4_GOS_OCFP v2.0.2, with significant residuals in the mean XCH₄ over North America, South America, and Africa. Also the mean longitudinal average XCH₄ has significant positive residuals around the equator (up to ~10 ppb). Smaller residuals are visible also for the other products, e.g. CH4_GOS_OCPR v7.0 inversions show a clear dipole in the residuals over North-America, slightly negative over western North-America, and slightly positive over eastern North-America, while for CH4_GOS_SRPR v2.3.8 the residual pattern over the United States is partly in opposite direction. Such residuals indicate that emission increments (and bias corrections) calculated in the inversion are not sufficient to achieve a fully bias-free agreement of the model simulations with the retrievals. Especially over the US, this may point to issues related to topography (i.e. representation of the real topography in the model, and proper use of the satellite retrievals over elevated surfaces). However, the fact that the described residual patterns over North-America are different for the inversions of the different retrieval products suggests that also the retrievals may have some inconsistencies.

Figure 42 shows also the total numbers of assimilated XCH₄ retrievals per 1°x1° grid cell. Please note, however, that these numbers are smaller than the number of original GOSAT pixels, because prior to the assimilation in TM5-4DVAR individual data records are averaged over the applied 3-hourly assimilation window and the 1°x1° grid. Furthermore, specific selection criteria were used (see section 4.2.1). The total number (and the spatial distribution) is very similar between the two proxy retrievals (CH₄_GOS_SRPR v2.3.8 and CH₄_GOS_OCPR v7.0). Compared to the proxy retrievals, the full physics retrievals have much less valid pixels, but their total number and spatial distribution are very similar between the two full physics retrievals (CH₄_GOS_SRFP v2.3.8 and CH₄_GOS_OCFP v2.0.2). The most striking pattern is the much lower number (and partly lack) of the full physics retrievals near the equator due to frequent occurrence of clouds.

4.2.4. CH₄ flux inversions: derived CH₄ fluxes

Figure 43 shows the derived CH₄ fluxes for the inversions of the four different GOSAT XCH₄ products (average 2010-2015). Overall, the four inversions show qualitatively very similar spatial distributions of the posteriori CH₄ fluxes, consistent with the analysis of the previous CRDP#3 GOSAT products described in CAR version 3 (Chevallier et al. 2016). Pronounced patterns in the inversions increments are the considerable emission increase over the South-Central United States, increase over tropical East Africa, and reductions over large parts of Southeast Asia compared to the prior emissions. A significant decrease is visible over the Congo basin for the inversions of the two proxy products (CH₄_GOS_SRPR v2.3.8 and CH₄_GOS_OCPR v7.0), while only smaller emission increments are derived in this regions from the inversions of the two full physics XCH₄ products (CH₄_GOS_SRFP v2.3.8 and CH₄_GOS_OCFP v2.0.2), most likely largely related to the much lower number of retrievals close to the equator (see section 4.2.3 and Figure 42).

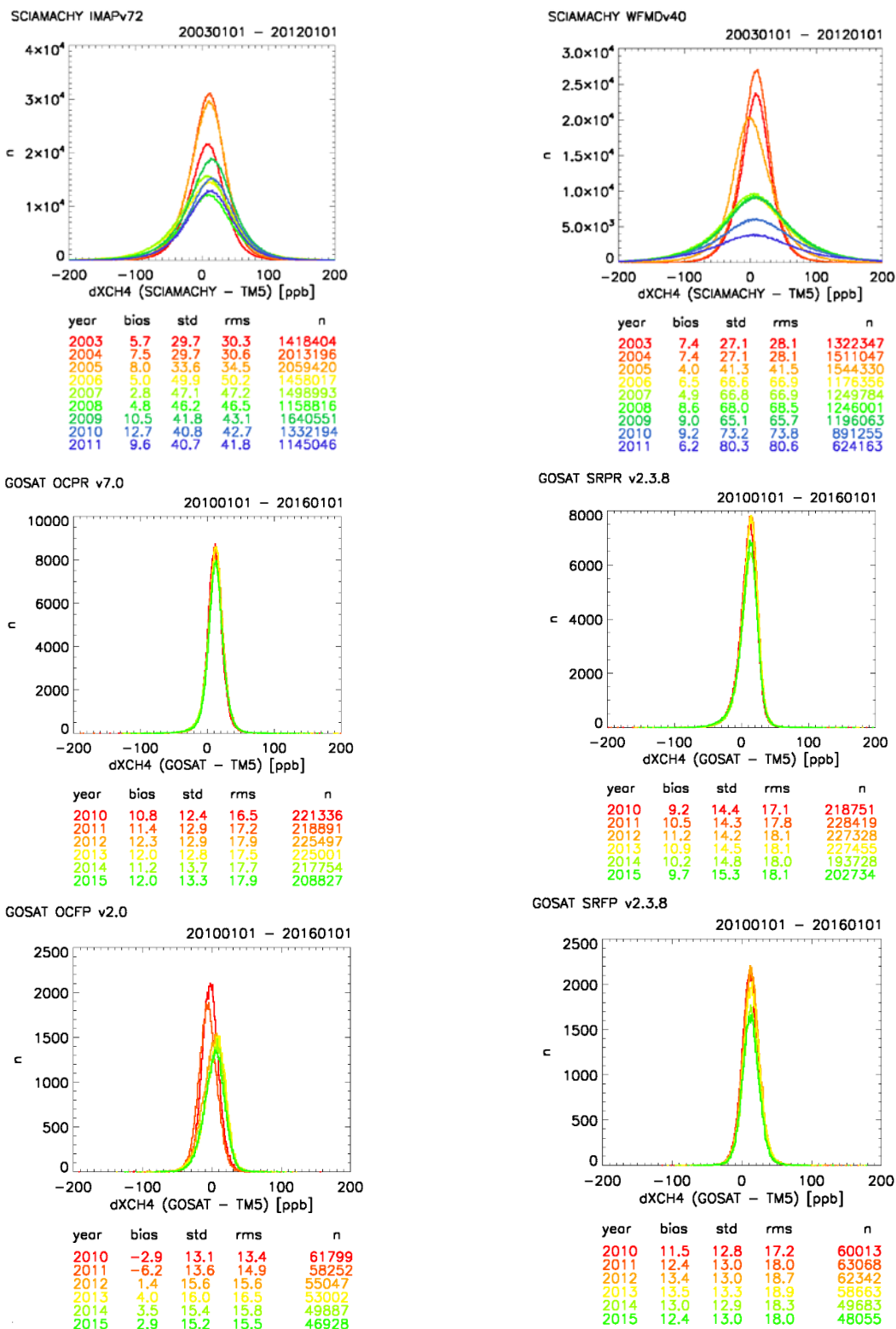


Figure 34. Comparison of different CRDP#4 XCH₄ products with TM5-4DVAR inversions based on NOAA surface observation: frequency distribution of deviations between XCH₄ retrievals and TM5-4DVAR model simulations.

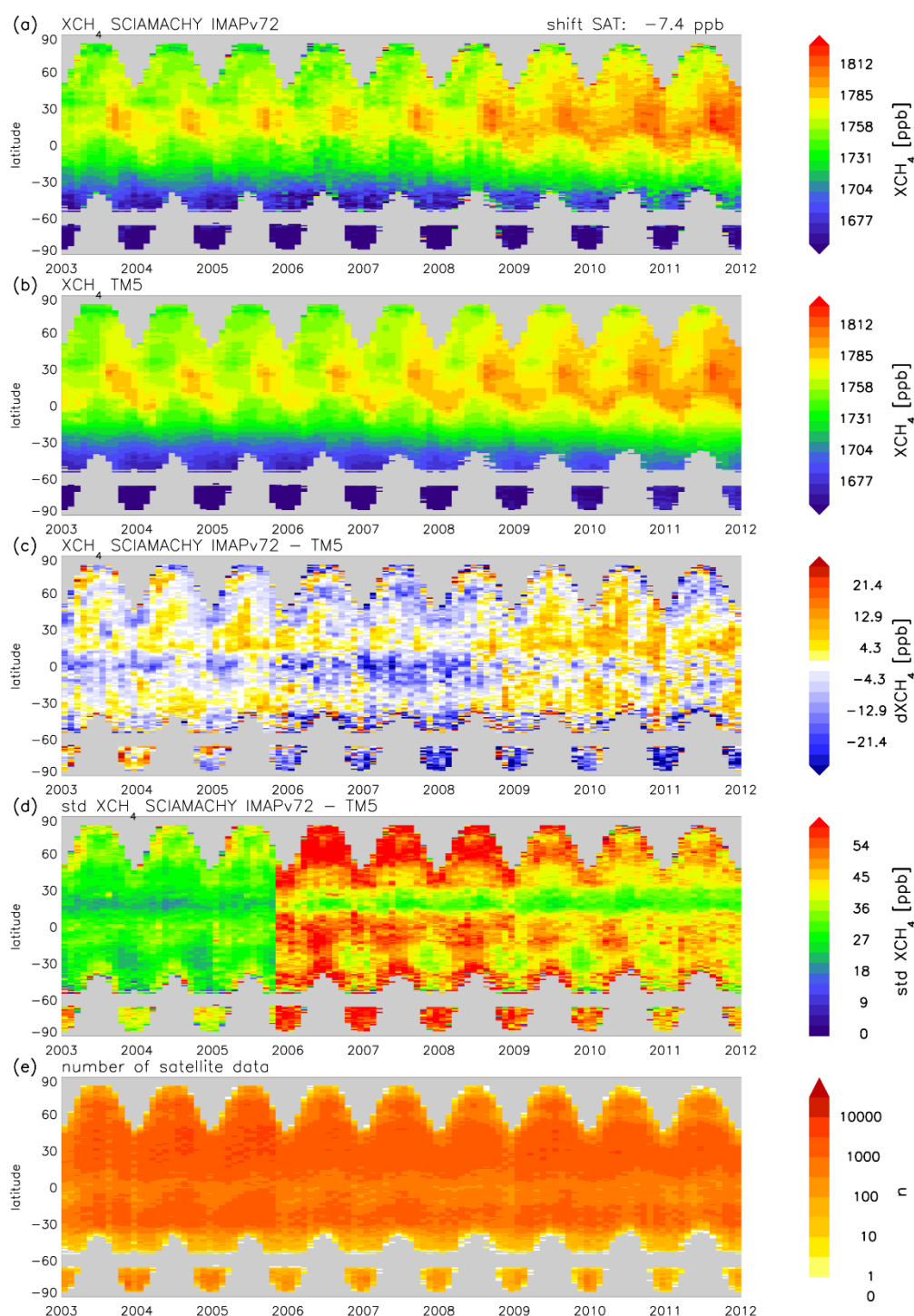


Figure 35. Comparison of CH_4 _SCI_IMAP v7.2 with TM5-4DVAR model simulations: time series from 2003 until 2011. (a) XCH_4 retrievals, monthly longitudinal averages (after subtracting a global offset of 7.4 ppb); (b) corresponding XCH_4 from TM5-4DVAR model simulations; (c) difference between XCH_4 retrievals and TM5-4DVAR; (d) standard deviation between XCH_4 retrievals and TM5-4DVAR model simulations (within each monthly 1° latitude bin); (e) number of valid XCH_4 retrievals.

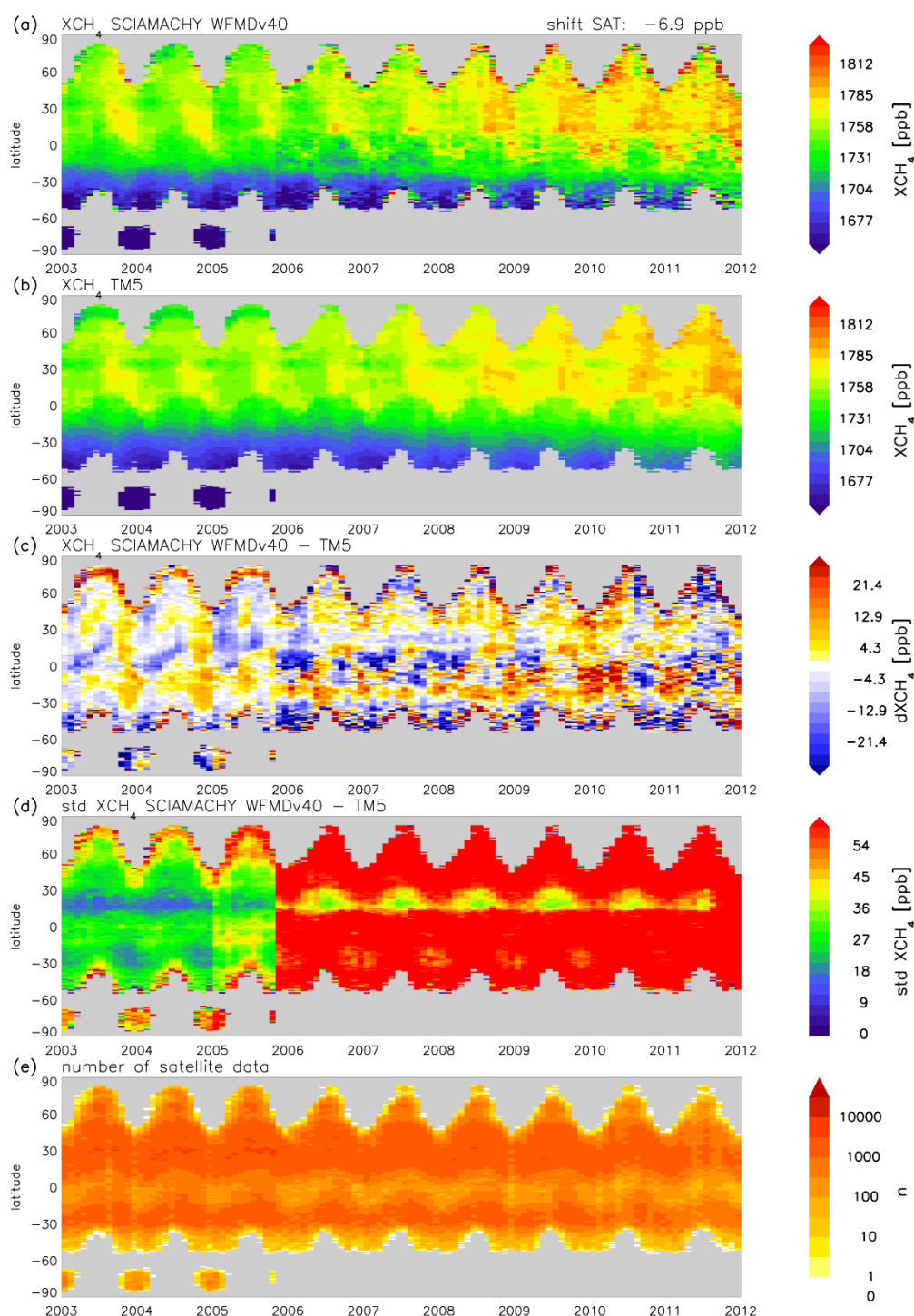


Figure 36. Comparison of CH₄_SCI_WFMD v4.0 with TM5-4DVAR model simulations: time series from 2003 until 2011. (a) XCH₄ retrievals, monthly longitudinal averages (after subtracting a global offset of 6.9 ppb); (b) corresponding XCH₄ from TM5-4DVAR model simulations; (c) difference between XCH₄ retrievals and TM5-4DVAR; (d) standard deviation between XCH₄ retrievals and TM5-4DVAR model simulations (within each monthly 1° latitude bin); (e) number of valid XCH₄ retrievals.

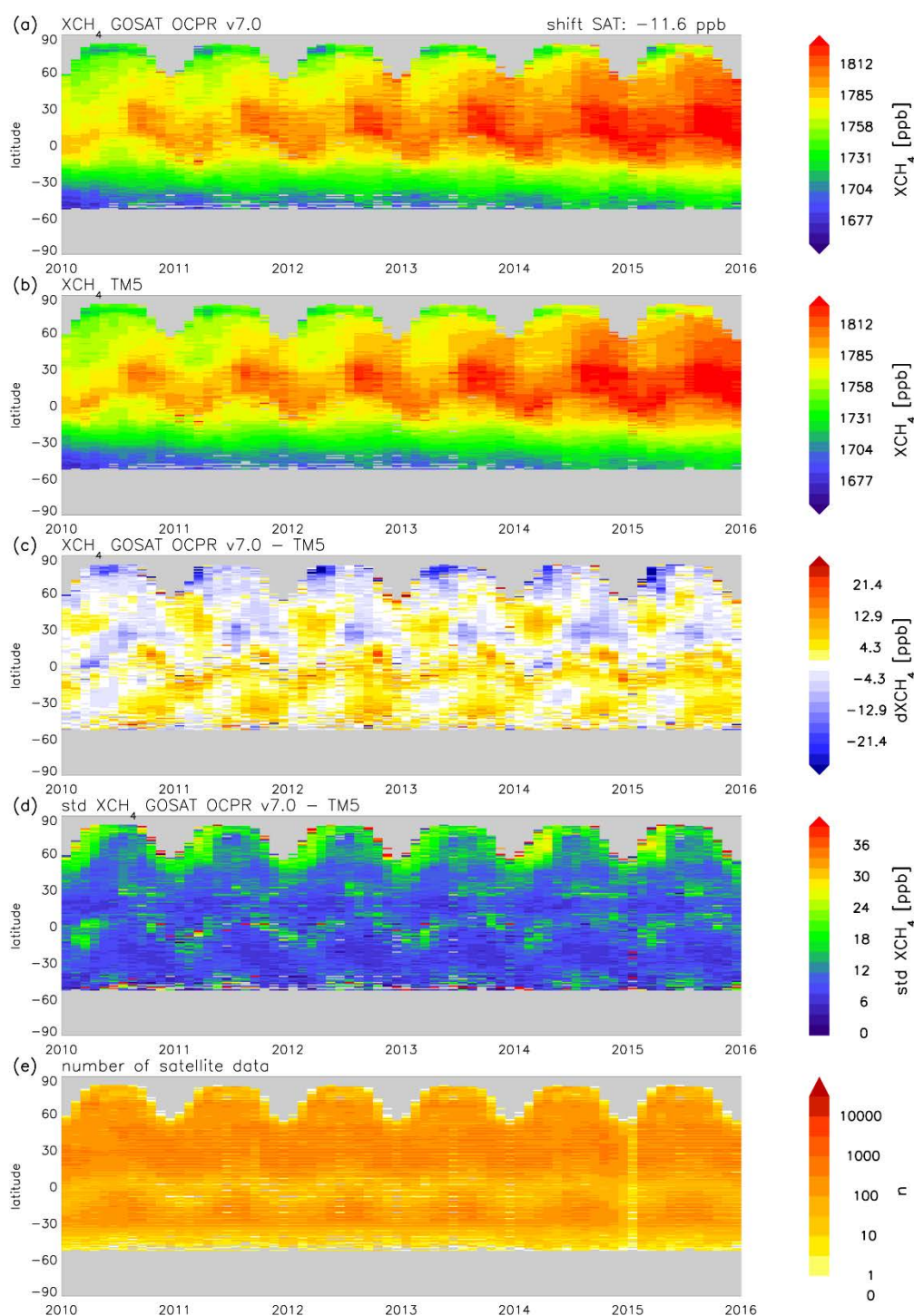


Figure 37. Comparison of CH_4 _GOS_OCPR v7.0 with TM5-4DVAR model simulations: time series from 2010 until 2015. (a) XCH_4 retrievals, monthly longitudinal averages (after subtracting a global offset of 11.6 ppb); (b) corresponding XCH_4 from TM5-4DVAR model simulations; (c) difference between XCH_4 retrievals and TM5-4DVAR; (d) standard deviation between XCH_4 retrievals and TM5-4DVAR model simulations (within each monthly 1° latitude bin); (e) number of valid XCH_4 retrievals.

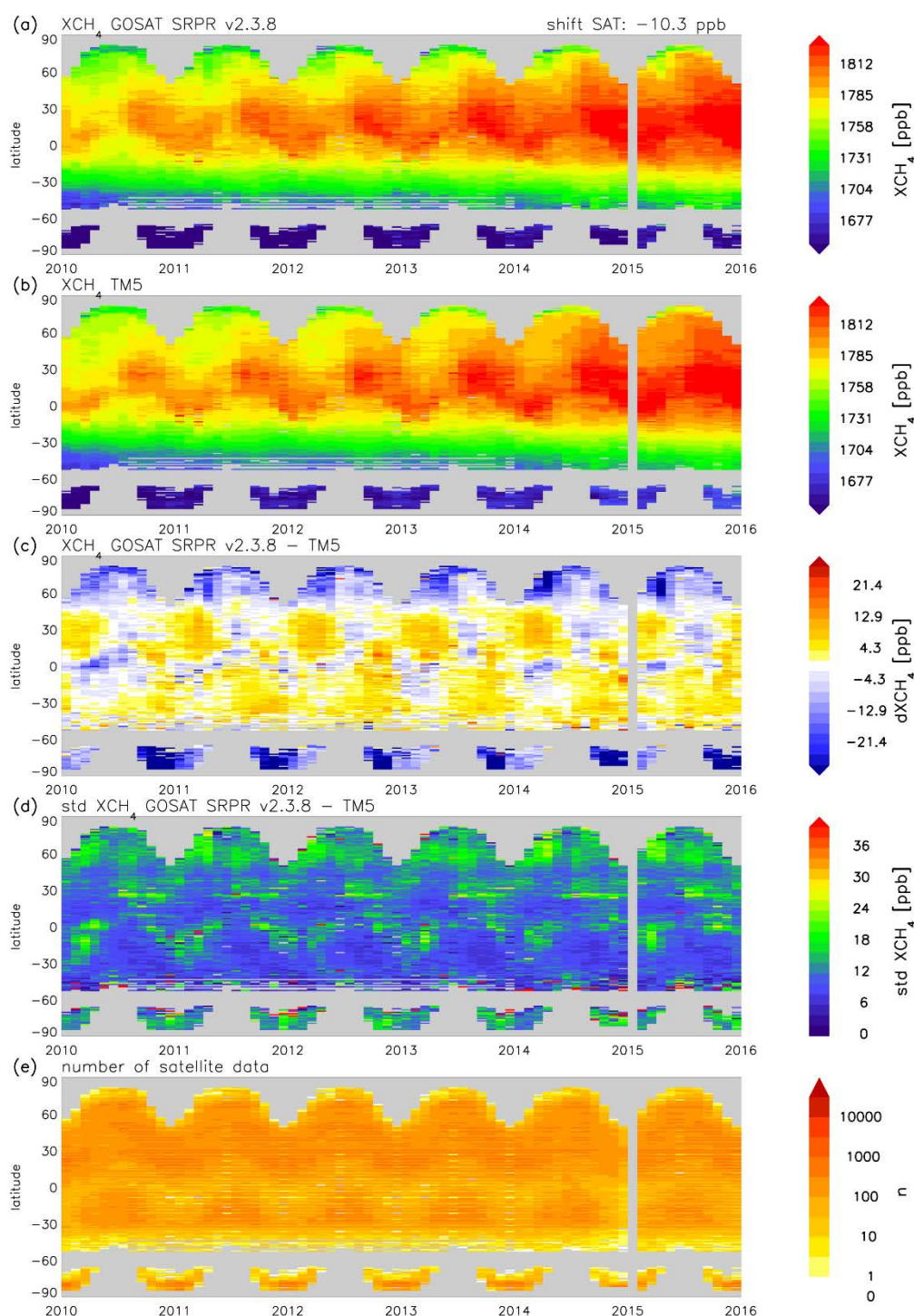


Figure 38. Comparison of CH_4 _GOS_SRPR v2.3.8 with TM5-4DVAR model simulations: time series from 2010 until 2015. (a) XCH_4 retrievals, monthly longitudinal averages (after subtracting a global offset of 10.3 ppb); (b) corresponding XCH_4 from TM5-4DVAR model simulations; (c) difference between XCH_4 retrievals and TM5-4DVAR; (d) standard deviation between XCH_4 retrievals and TM5-4DVAR model simulations (within each monthly 1° latitude bin); (e) number of valid XCH_4 retrievals.

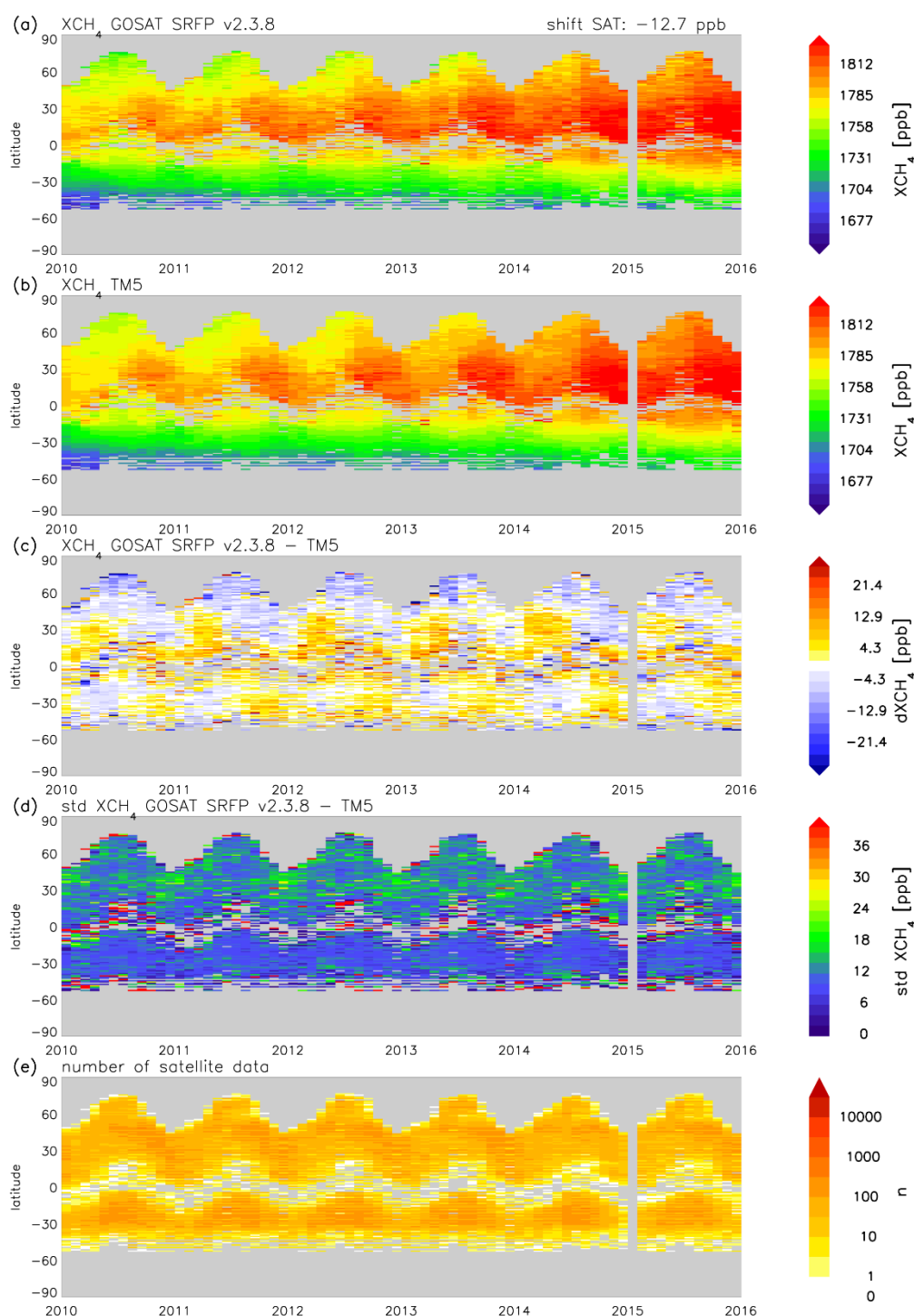


Figure 39. Comparison of CH_4 _GOS_SRFP v2.3.8 with TM5-4DVAR model simulations: time series from 2010 until 2015. (a) XCH_4 retrievals, monthly longitudinal averages (after subtracting a global offset of 12.7 ppb); (b) corresponding XCH_4 from TM5-4DVAR model simulations; (c) difference between XCH_4 retrievals and TM5-4DVAR; (d) standard deviation between XCH_4 retrievals and TM5-4DVAR model simulations (within each monthly 1° latitude bin); (e) number of valid XCH_4 retrievals.

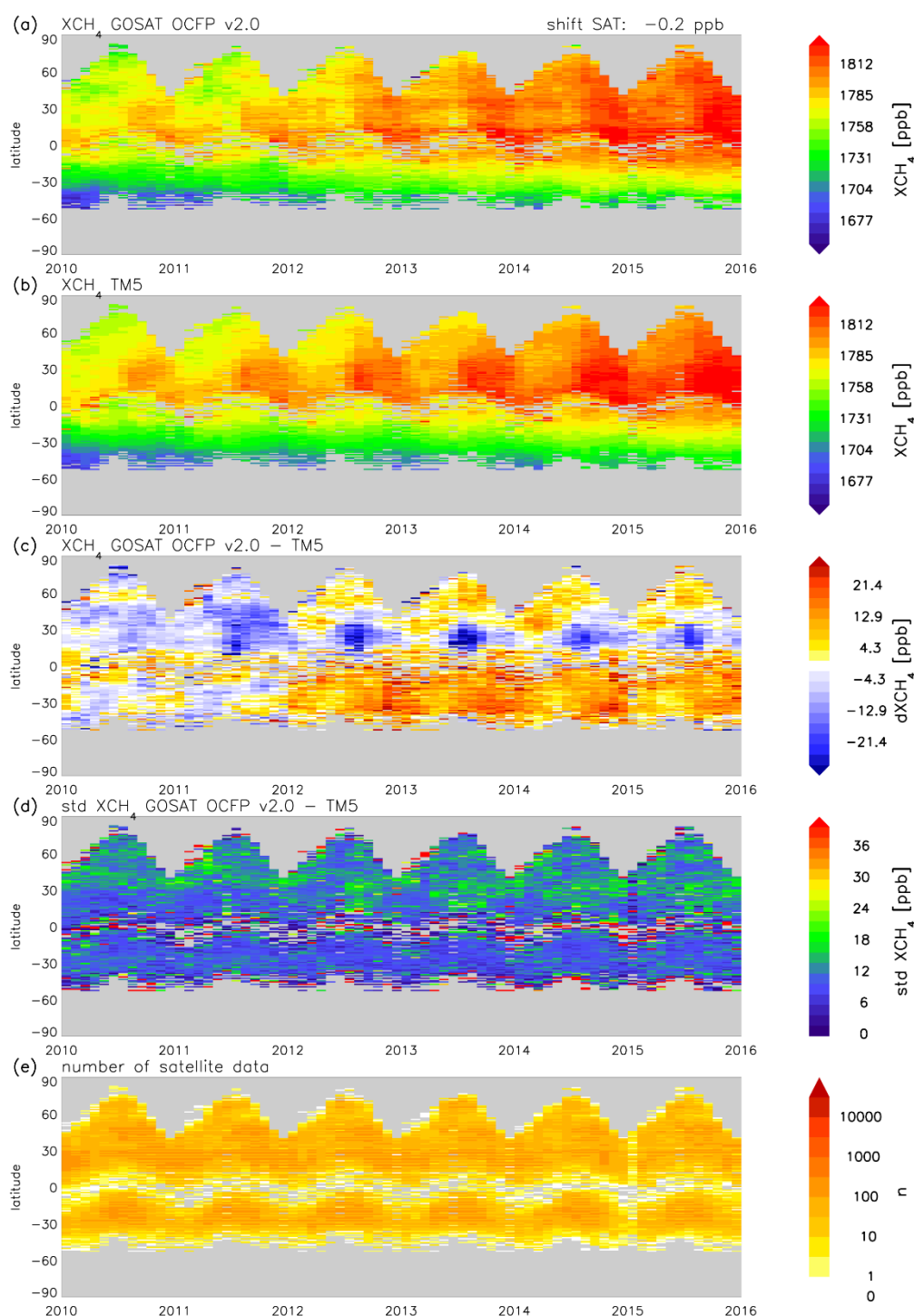


Figure 40. Comparison of CH_4 _GOS_OCFP v2.0 with TM5-4DVAR model simulations: time series from 2010 until 2015. (a) XCH_4 retrievals, monthly longitudinal averages (after subtracting a global offset of 0.2 ppb); (b) corresponding XCH_4 from TM5-4DVAR model simulations; (c) difference between XCH_4 retrievals and TM5-4DVAR; (d) standard deviation between XCH_4 retrievals and TM5-4DVAR model simulations (within each monthly 1° latitude bin); (e) number of valid XCH_4 retrievals.

01/2010–12/2015

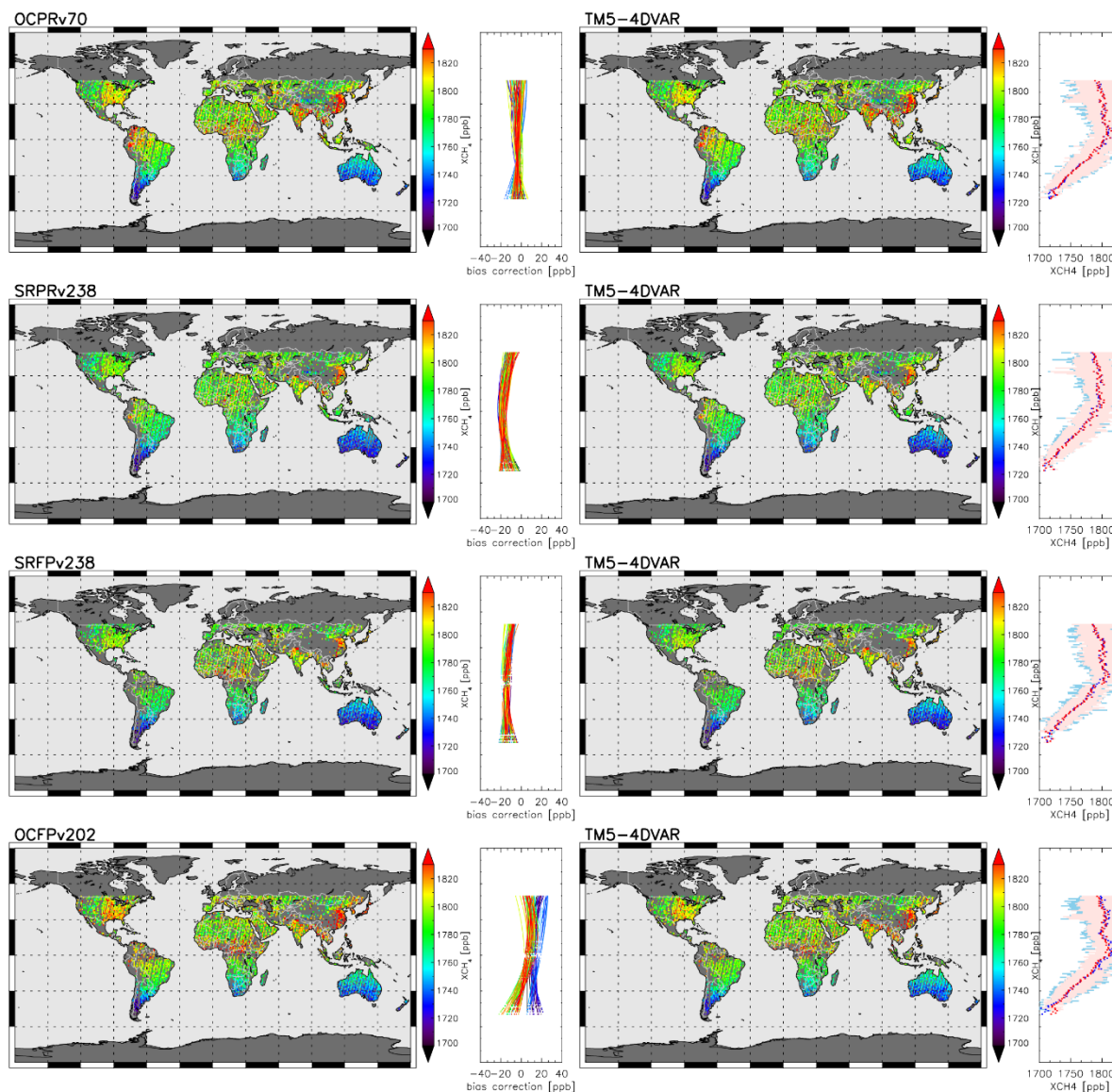


Figure 41. Column averaged CH₄ dry air mole fractions (XCH₄). Left: XCH₄ retrievals (composite average 2010-2015) including bias correction calculated by TM5-4DVAR. The bias correction (as function of latitude and month) is shown in the small panels (second column; bias corrections for individual months shown in different colors (from dark violet (01/2010) to red (12/2015))). Right: Assimilated XCH₄. The longitudinal averages of XCH₄ retrievals (after bias correction; blue) and assimilated XCH₄ (red) are shown in the small panels on the right side (4th column). The light blue area shows the range of XCH₄ retrievals across all longitudes (for the 2010-2015 average) and the light red area the corresponding range for the assimilated XCH₄. The four rows show the retrievals and corresponding model simulations for the 4 GOSAT products analyzed (see Table 3).

01/2010–12/2015

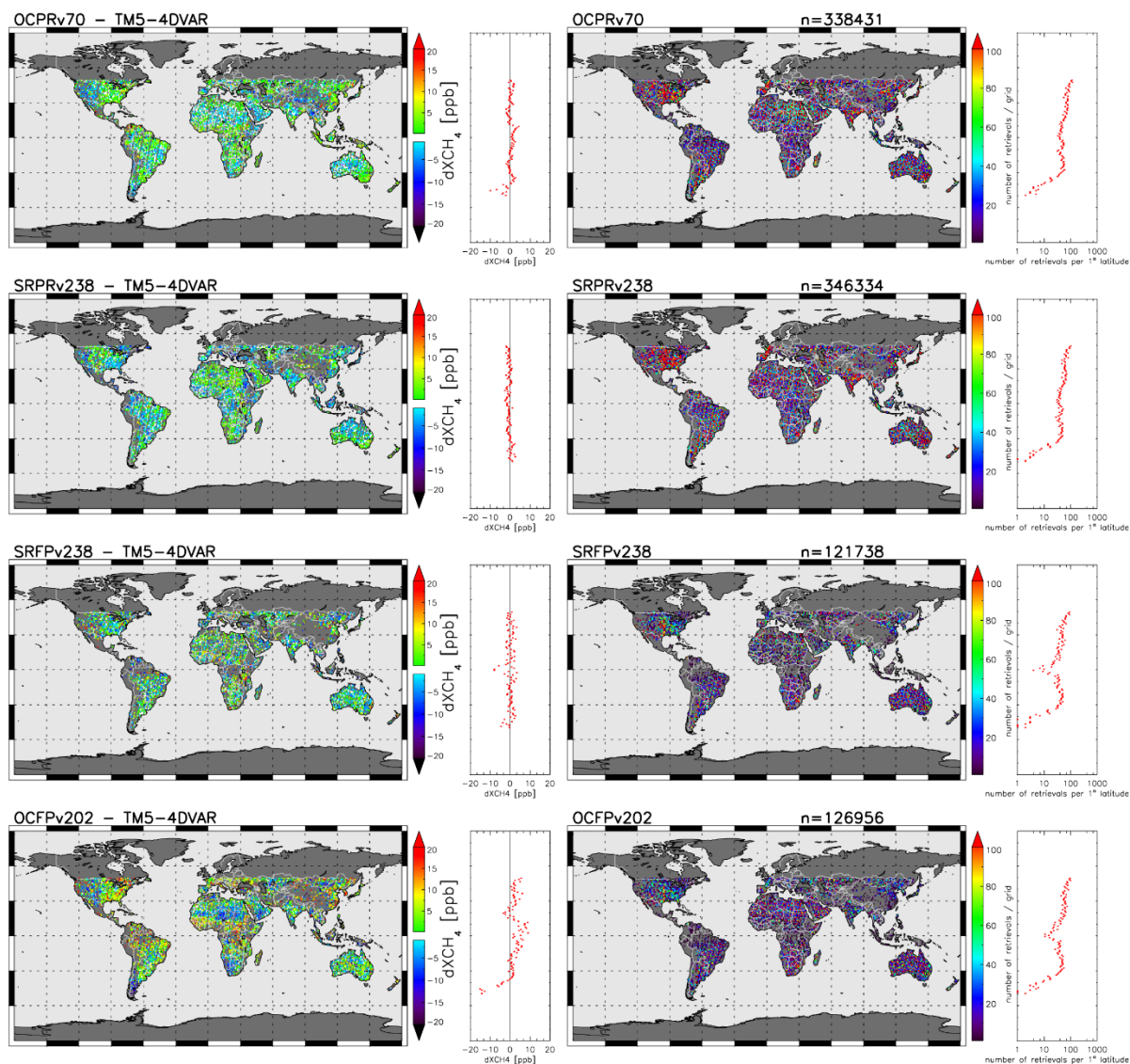
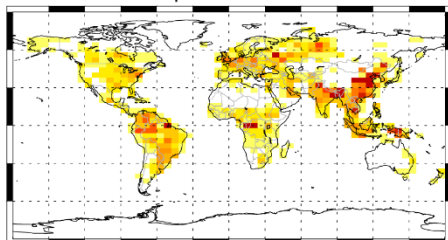


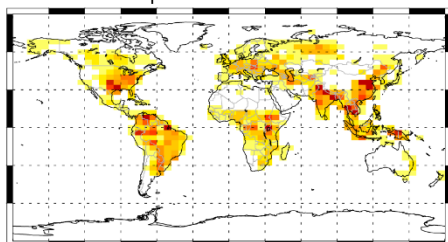
Figure 42. Left: difference between XCH₄ retrievals (after bias correction) and model simulations (assimilated XCH₄); composite average 2010–2015. The longitudinal averages of these XCH₄ differences are shown in the small panels on the right (second column). Right: total numbers of assimilated XCH₄ retrievals per 1°x1° grid cell (note that these numbers are smaller than the numbers of original valid GOSAT pixels, because prior to the assimilation in TM5-4DVAR individual data records are averaged over the applied 3-hourly assimilation window and the 1°x1° grid; furthermore, specific selection criteria were used (see section 4.2.1)). The total numbers of assimilated XCH₄ retrievals across all longitudes (per 1° latitude band) are shown in the small panels on the right side (4th column).

01/2010–12/2015

TM5–4DVAR a priori

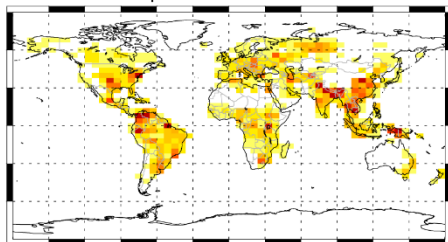


TM5–4DVAR posteriori OCPRv70



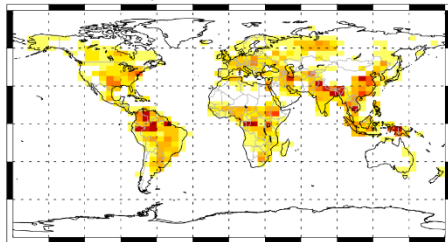
VAR_M07B.ECC.CH4_glb_OCPR70_E42FL_K_G3_TM_EC_V01.J3

TM5–4DVAR posteriori SRPRv238



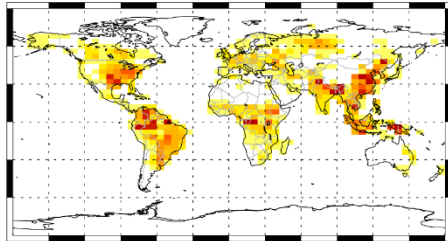
VAR_M07B.ECC.CH4_glb_SRPR238_E42FL_K_G3_TM_EC_V01.J3

TM5–4DVAR posteriori SRFPv238



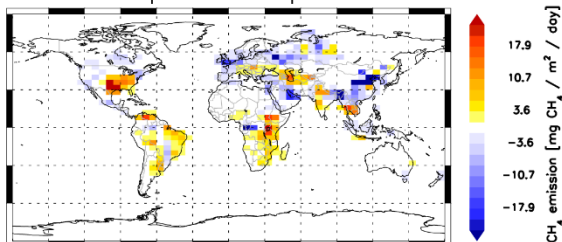
VAR_M07B.ECC.CH4_glb_SRFP238_E42FL_K_G3_TM_EC_V01.J3

TM5–4DVAR posteriori OCFPv202

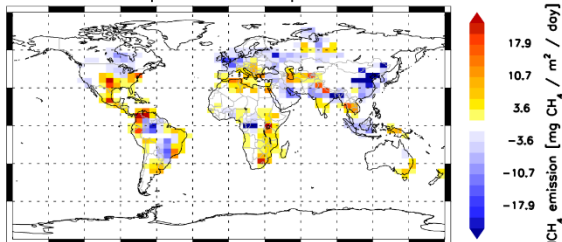


VAR_M07B.ECC.CH4_glb_OCFP202_E42FL_K_G3_TM_EC_V01.J3

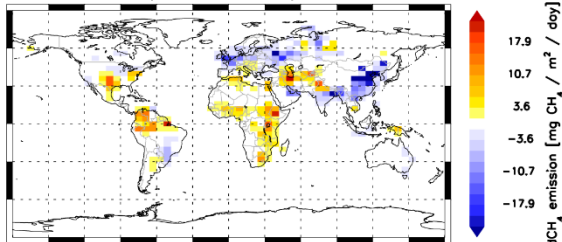
TM5–4DVAR posteriori – prior OCPRv70



TM5–4DVAR posteriori – prior SRPRv238



TM5–4DVAR posteriori – prior SRFPv238



TM5–4DVAR posteriori – prior OCFPv202

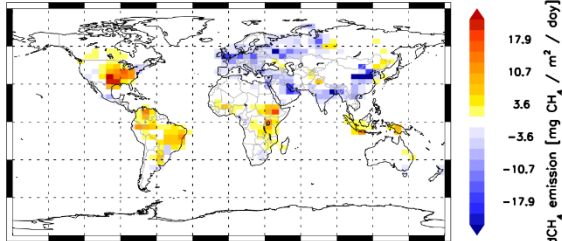



Figure 43. CH₄ emissions (average 2010–2015). Upper left map shows the applied prior emissions, and the subsequent rows the posteriori emissions (left) and the inversion increments (difference between posterior and prior emissions; right) for the inversions of 4 GOSAT products (see Table 3).

	ESA Climate Change Initiative (CCI)	Page 75
	Climate Assessment Report (CAR)	
	for the Essential Climate Variable (ECV) Greenhouse Gases (GHG)	Version 4 (final)
		28 March 2017

4.2.5. Conclusions


Compared to CRDP#3, the CH₄_SCI_IMAP product has been significantly improved regarding the consistency of the time series. However, the comparison of the new CH₄_SCI_IMAP v7.2 retrievals with surface observation based inversions still show significant changes of the longitudinal average XCH₄ differences over time (especially during 2006-2008), which are likely largely an artifact of the retrievals and which could be related to the pixel degradation end of 2005.

For CH₄_SCI_WFMD v4.0, the impact of the pixel degradation is even larger (larger increase in the standard deviation between retrievals and model simulations after 2005 compared to CH₄_SCI_IMAP v7.2). Furthermore CH₄_SCI_WFMD v4.0 shows larger changes of the longitudinal average differences between XCH₄ retrievals and model simulations with time than CH₄_SCI_IMAP v7.2.

Compared to the two SCIAMACHY products, the four GOSAT products have significantly better quality, with annual standard deviations between retrievals and model simulations in the range of 12-16 ppb, while the annual standard deviations are in the range 30-50 ppb for CH₄_SCI_IMAP v7.2 and 27-80 ppb for CH₄_SCI_WFMD v4.0.

The four GOSAT XCH₄ products show an overall good consistency regarding their spatial XCH₄ patterns and the use of these four products in the TM5-4DVAR inverse modelling system results in qualitatively similar spatial distributions of the posteriori CH₄ fluxes (average 2010-2015). There remains however quantitative differences in the derived regional fluxes which need to be further analyzed. An important issue remains also the bias correction, which is still required for the simultaneous assimilation of the satellite retrievals and the NOAA surface observations. Our analysis suggests that the calculated bias correction reflects a combination of model errors (especially the vertical CH₄ gradient in the stratosphere at mid to high latitudes) and remaining systematic errors in the XCH₄ retrievals. For CH₄_GOS_OCFP v2.0.2 we identified a significant time dependent bias, which is apparent (1) from the comparison with the surface observation based inversion, and (2) from the significant changes of the required bias correction over time, when inverting this product (together with the surface measurements).

CH₄_GOS_SRFP v2.3.8 shows overall good consistency with the two GOSAT proxy retrievals. Despite the lower number of valid pixels (both in the original datasets and after application of the described specific selection criteria in TM5-4DVAR), the full physics retrievals are considered as very valuable because they are independent from CO₂ model fields.

	ESA Climate Change Initiative (CCI)	Page 76
	Climate Assessment Report (CAR)	
	for the Essential Climate Variable (ECV) Greenhouse Gases (GHG)	Version 4 (final)
		28 March 2017

4.3. CH₄ fluxes inferred from GOSAT proxy XCH₄:XCO₂ retrievals with the UoE system

4.3.1. Method

Fraser et al (2014) demonstrated using the maximum likelihood estimation a method to simultaneously infer regional CO₂ and CH₄ flux estimates from the GOSAT XCH₄:XCO₂ ratio of CH₄ and CO₂ dry-air mole fraction measurements retrieved using the proxy approach. The proxy retrieval approach fits CO₂ and CH₄ gases in nearby spectral windows at 1.65 μm and 1.61 μm, under the assumption that the ratio of these two gases is less sensitive to fitting artefacts common to both gases, e.g. aerosol and clouds. In general the proxy data product is simpler than the full physics retrieval approach, and is more robust against scattering so that there are more useable retrievals over geographical regions that are compromised by seasonal aerosol and clouds, e.g., tropical South America. Using these data directly, together with in situ mole fraction observations of CO₂ and CH₄, we can estimate simultaneously CO₂ and CH₄ fluxes. We present an update to that approach, building on work recently reported by Feng et al. (2016b) that uses an ensemble Kalman filter (EnKF), to infer monthly surface CO₂ and CH₄ fluxes using GOSAT XCH₄:XCO₂ proxy data.

We assimilate GOSAT proxy XCH₄:XCO₂ retrievals from CH₄_GOS_OCPR and CH₄_GOS_SRPR from 2010 to 2015, inclusive. To anchor the inversion system (Fraser et al., 2014; Feng et al., 2016b), we also assimilate CO₂ and CH₄ mole fraction measurements from the NOAA in situ network. The inversion set up is the same as used in CARv3 (Chevallier et al., 2016). We use the GEOS-Chem global chemistry transport model to relate surface fluxes to the observed variations of atmospheric CO₂ and CH₄ concentrations (Fraser et al., 2014) at a horizontal resolution of 4° latitude and 5° longitude, driven by GEOS-5 (GEOS-FP after 2012) meteorological analyses from the Global Modeling and Assimilation Office Global Circulation Model based at NASA Goddard Space Flight Centre. Emission inventories common for both CO₂ and CH₄ include: monthly biomass burning emission (GFEDv3.0, van der Werf et al., 2010) and monthly fossil fuel emissions (ODIAC, Oda and Maksyutov, 2011). To describe atmospheric CO₂ variations, we also use monthly-resolved climatological ocean fluxes (Takahashi et al., 2009), and three-hourly terrestrial biosphere fluxes (CASA, Olsen and Randerson, 2004). To describe atmospheric CH₄ variations (see Fraser et al (2014) for more details), we use prescribed annual inventories for emissions from oil and gas production, coal mining, ruminant animals (Olivier et al., 2005), termites, and hydrates (Fung et al., 1991). We use monthly-resolved emissions from rice paddies and wetlands (Bloom et al., 2012). We use monthly 3-D concentration fields of the hydroxyl radical sink and a simple soil sink.

For the inversion, we distinguish between CO₂ fluxes from the ocean, the terrestrial biosphere and from anthropogenic activity. Similarly, for CH₄ we distinguish between anthropogenic emissions (broken down further into coal mining and other), and natural fluxes (broken down further into wetlands, rice paddies, biomass burning, and other).

In the inversion experiments, we estimate scaling coefficients for these emission categories at a temporal resolution of 1 month over 44 land regions, and 11 oceanic regions, by optimally fitting the

model simulations with in situ CO₂ and CH₄ concentrations, as well as with the GOSAT proxy retrievals. We assume that the a priori uncertainty of the natural CO₂ (CH₄) emissions is equal to 40% (60%) of the monthly emissions over each land regions. We use smaller uncertainties (25% for CO₂ and 40% for CH₄) for anthropogenic emissions. We also assume that the a priori errors are correlated with each other with a spatial correlation length of 800 km, and a temporal correlation of 1 month (Feng et al., 2016a).

Below, we present three parallel inversions, by assimilating different set of observations:

1. **INSITU** for which only NOAA in situ CO₂ and CH₄ observations are assimilated;
2. **OCPR** for which GOSAT proxy XCH₄:XCO₂ retrievals of OCPR version 7.0, together with NOAA in situ CO₂ and CH₄ observations; and
3. **SRPR** for which GOSAT proxy XCH₄:XCO₂ retrievals of SRPR version 2.3.8, together with NOAA in situ CO₂ and CH₄ observations.

These inversions assimilate a common set of in situ CH₄ observations from 47 NOAA sites and in situ CO₂ observations from 72 sites (Fraser et al., 2014; Feng et al., 2016a). For experiments OCPR and SRPR we assume that each single proxy XCH₄:XCO₂ retrieval is independent, but with doubled uncertainty as recommended by the retrieval teams.

4.3.2. Results

4.3.2.1. Annual flux maps

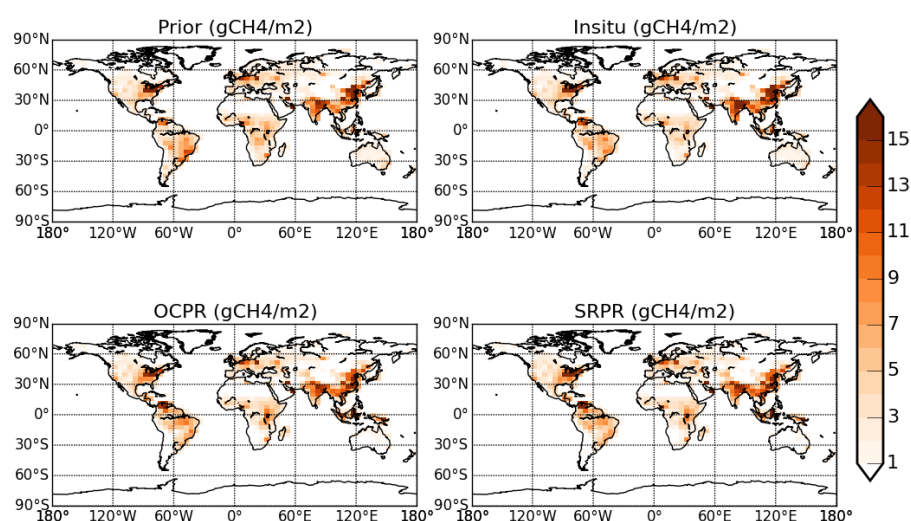


Figure 44. Annual fluxes of CH₄ (kgCH₄/km²) averaged on a 4° latitude and 5° longitude grid over 2010-2015.

Figure 44 shows that, compared to the a priori flux inventories and a posteriori fluxes inferred from in situ data, the a posteriori fluxes inferred from OCPR and SRPR data show larger emissions over Tropical Asia and Tropical South America, and lower emissions from temperate regions, particularly over China. These regions are typically where the in situ measurement coverage is particularly poor.

Figure 45 shows the differences between the three inversions. It again shows that the two inversions using GOSAT XCH₄:XCO₂ are more similar than either OCPR or SRPR with INSITU. The differences between the inversions OCPR and SRPR are generally very small, with the largest values mainly over regions where the observation coverage provided by the two products are slightly different (e.g., over tropical South America). Despite the spatial differences between the three inversions, the corresponding global totals are reasonably similar: 514±25 Mt/yr for INSITU, 518±12 Mt/yr for OCPR, and 521±12 Mt/yr for SRPR. These annual means are slightly larger (up to 3 Mt/yr) than the means inferred from previous OCPR v6 and SRON v2.37 (Chevallier et al., 2016) for 2010-2014, mainly due to larger emissions for 2015 (e.g., 538±12 Mt/yr for OCPR). Similar to our previous experiments using OCPR v6 and SRON v2.3.7 data sets (Chevallier et al., 2016, Feng et al., 2016b), we find the shift of emissions from northern mid-latitudes towards the lower latitudes, which has been reported previously in other studies that use full physics and proxy XCH₄ retrievals (e.g., Alexe et al., 2015).

Climate Assessment Report (CAR)

for the Essential Climate Variable (ECV)
Greenhouse Gases (GHG)

Version 4
(final)

28 March 2017

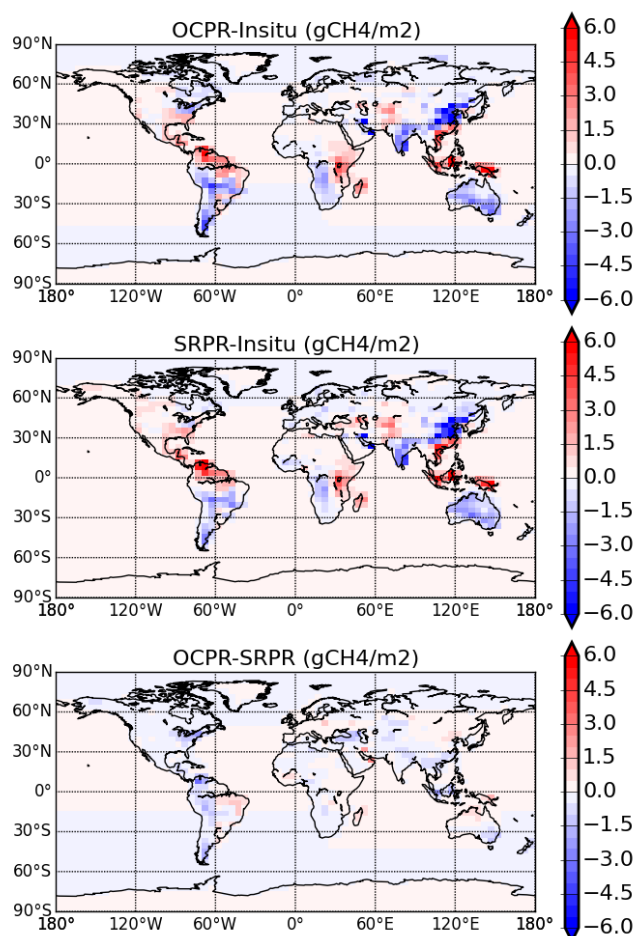


Figure 45. Differences between annual mean a posteriori CH_4 fluxes from inversion experiments: INSITU, OCPR and SRPR, averaged on a 4° latitude and 5° longitude grid over 2010-2015,

4.3.2.2. Regional annual emissions

We spatially aggregate flux estimates using commonly-used geographical regions of Figure 45. Figure 46 shows that the a posteriori flux estimates inferred from the GOSAT $\text{XCH}_4:\text{XCO}_2$ data are lower over northern mid-latitude regions (e.g., Eurasia temperate) and higher over tropical regions. We find that using $\text{XCH}_4:\text{XCO}_2$ data significantly reduces the a posteriori flux uncertainty (up to 70%) over these regions, which are poorly constrained by current in situ observations.

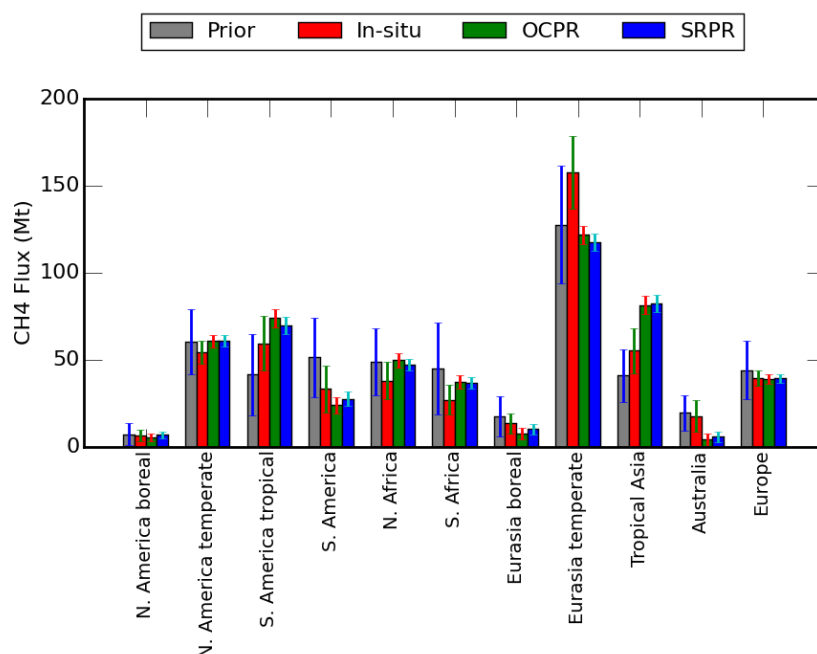


Figure 46. Regional annual CH₄ emissions (Mt CH₄) on the TransCom-3 geographical regions, averaged over 2010-2015.

4.3.2.3. Seasonal cycle on a regional scale

Figure 48 shows that OCPR or SRPR posterior flux estimates generally have larger seasonal cycles than the fluxes estimates from the in situ data, particularly over the tropics where there are less in situ data. These results are similar to those inferred from previous versions of OCPR and SRPR. We find that that OCPR and SRPR are generally in good agreement, as shown above, with the exception of the winter months at temperate northern latitudes and over the tropics that is related to observation coverage as a result of observation quality filtering applied by the retrieval teams.

Climate Assessment Report (CAR)

for the Essential Climate Variable (ECV)
Greenhouse Gases (GHG)

Version 4
(final)

28 March 2017

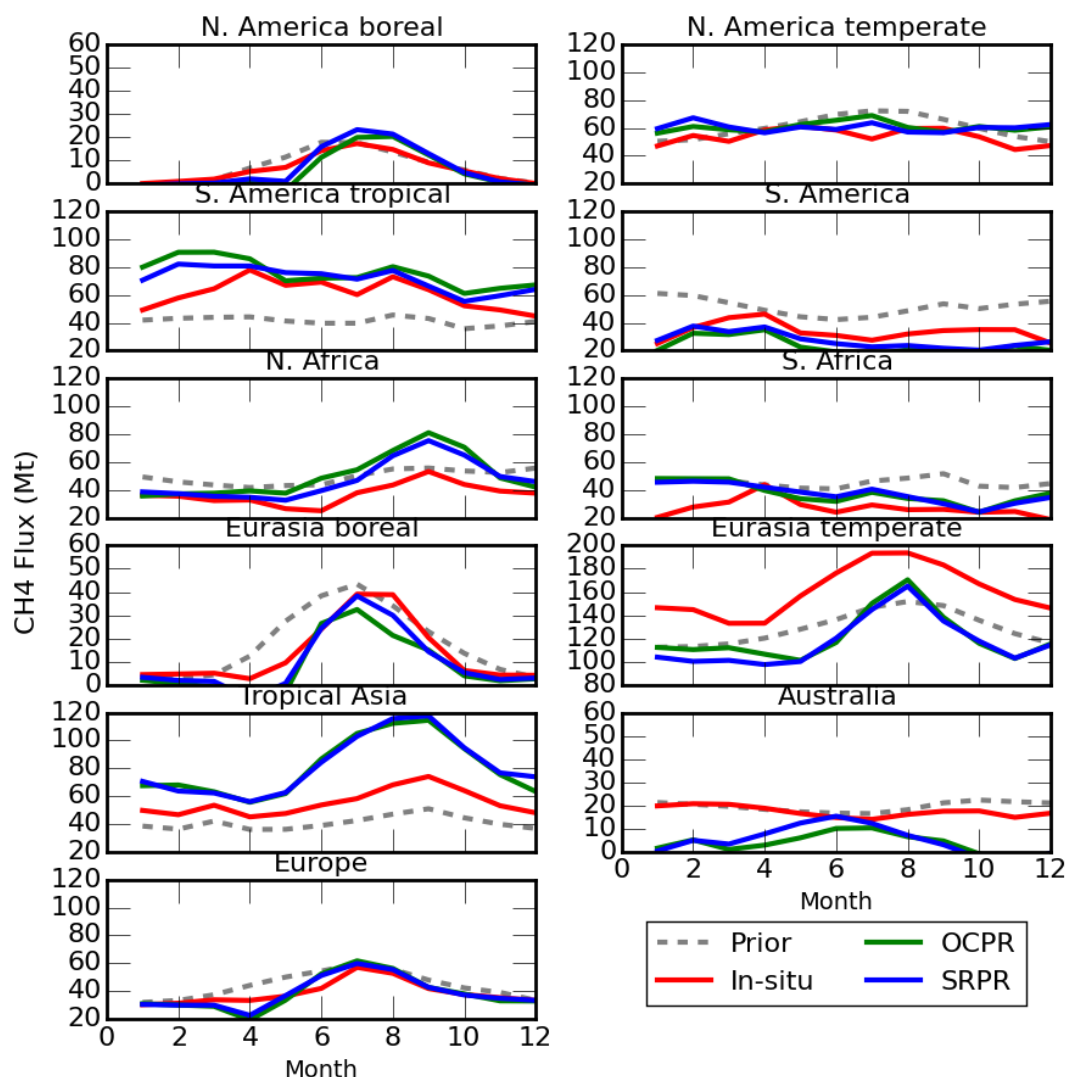


Figure 47. Seasonal cycle of a priori and a posteriori monthly CH₄ fluxes over 11 TransCom-3 land regions, averaged 2010-2015.

Figure 47 shows that, as expected, INSITU has a different trend compared with OCPR or SRPE over tropical regions, particularly pronounced for 2014 and 2015. During 2014 and 2015, for example, the OCPR and SRPR inversions show generally increased monthly emissions over North Africa, and reduced emissions over tropical Asia and tropical South America while INSITU shows smaller or even opposite trends. During 2015, we find that OCPR fluxes over tropical South America and tropical Asia are generally larger than SRPR, which is due to their different observation coverages.

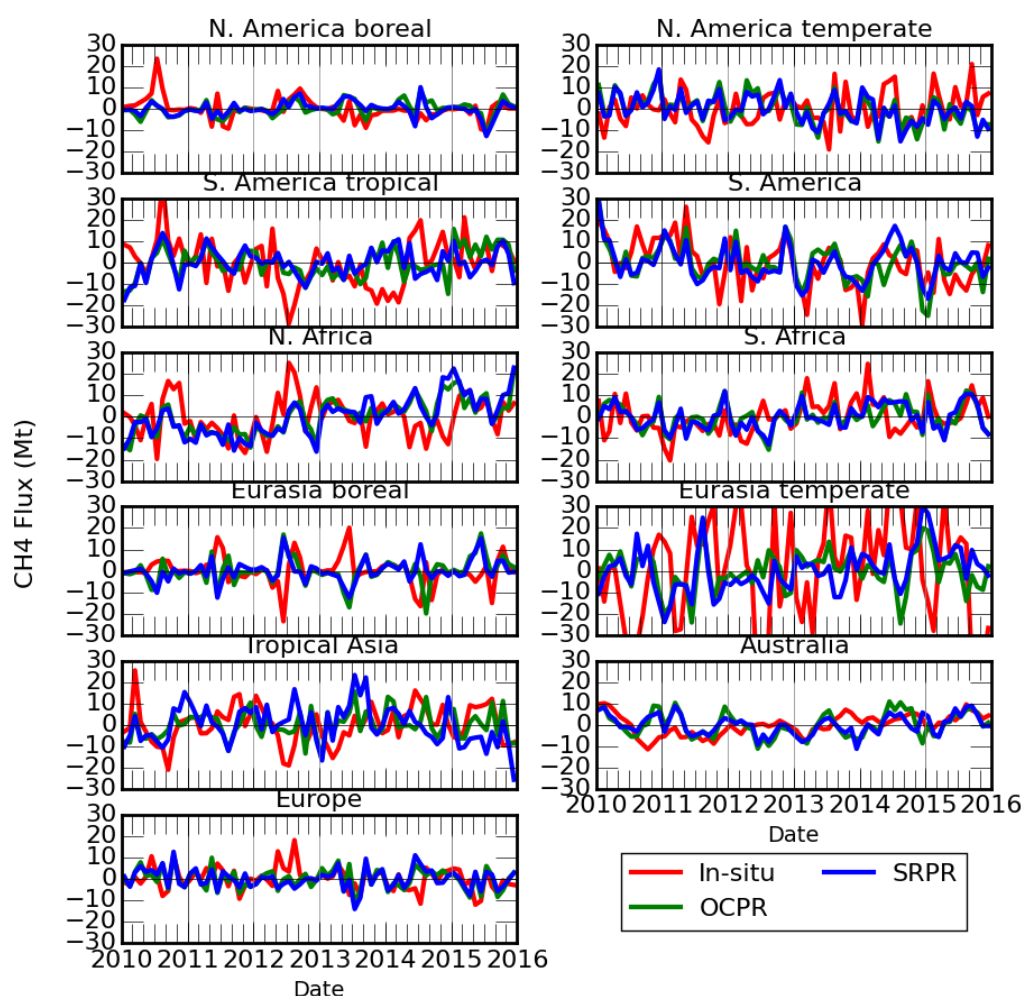



Figure 48. Monthly mean CH₄ flux anomalies (Mt CH₄) from 2010-2015, relative to the 2010-2015 monthly means.

4.3.3. Conclusions

We have shown that assimilating proxy XCH₄:XCO₂ retrievals significantly reduces uncertainties of the a posteriori CH₄ flux estimates, particularly over tropical regions where in-situ measurement coverage is poor. The in-situ and proxy ratio data all result in similar global annual CH₄ emission totals, but the ratio data have lower emissions from temperate regions and higher emissions from the tropics. These results are broadly consistent with previous studies (Chevallier et al., 2016, Feng et al., 2016b) using OCPR v6 and SRPR v2.3.7, and also agree with the inversions that use full-physics or proxy XCH₄ retrievals. We also found that assimilating the XCH₄:XCO₂ proxy data led to larger seasonal cycles over tropical regions. Broadly, the two proxy datasets are consistent but we find differences at their resulting seasonal cycles over some northern regions such as Temperate Northern America. The

	ESA Climate Change Initiative (CCI)	Page 83
	Climate Assessment Report (CAR)	
	for the Essential Climate Variable (ECV) Greenhouse Gases (GHG)	Version 4 (final)
		28 March 2017


differences are caused by different observation coverage as a result of different data filtering applied by the retrieval teams. This is also reflected in the year-to-year variations over geographical regions but in general the flux estimates inferred from the two GOSAT proxy datasets are more consistent with each other than the fluxes inferred from the in situ data.

Acknowledgements

The authors thank the various providers of CRDP and M. Buchwitz for constructive discussions about the use and the evaluation of these products. TCCON data were obtained from the TCCON Data Archive, operated by the California Institute of Technology from the website at <http://tccon.ipac.caltech.edu/>. Support for TCCON is provided by many national research support organizations that are listed on the TCCON web site. Wolfgang Knorr and Michael Voßbeck are acknowledged for their help for Section 48. The authors are very grateful to the many people involved in the surface air sample measurement and in the archiving of these data. Some of the computations of Sections 3.2 and 3.3 have been performed using HPC resources from CCRT under the allocation 2016-t2015012201 made by GENCI (Grand Equipement National de Calcul Intensif).

References

- Alexe, M., P. Bergamaschi, A. Segers, et al., Inverse modeling of CH₄ emissions for 2010–2011 using different satellite retrieval products from GOSAT and SCIAMACHY, *Atmos. Chem. Phys.*, 15, 113–133, doi:10.5194/acp-15-113-2015, 2015.
- Bastos, A., Running, S.W., Gouveia, C. and Trigo, R.M: The global NPP dependence on ENSO: La-Nina and the extraordinary year of 2011. *J. Geophys. Res.* 118, 1247–1255, 2013
- Basu, S., Guerlet, S., Butz, A., et al., Global CO₂ fluxes estimated from GOSAT retrievals of total column CO₂, *Atmos. Chem. Phys.*, 13, 8695–8717, 2013.
- Basu, S., Krol, M., Butz, A., et al., The seasonal variation of the CO₂ flux over Tropical Asia estimated from GOSAT, CONTRAIL and IASI, *Geophys. Res. Lett.*, doi: 10.1002/2013GL059105, 2014.
- Bergamaschi, P., C. Frankenberg, J. F. Meirink, M. Krol, M. G. Villani, S. Houweling, F. Dentener, E. J. Dlugokencky, J. B. Miller, L. V. Gatti, A. Engel, and I. Levin: Inverse modeling of global and regional CH₄ emissions using SCIAMACHY satellite retrievals, *J. Geophys. Res.*, 114, doi:10.1029/2009JD012287, 2009.
- Bergamaschi, P., et al.: Inverse modeling of European CH₄ emissions 2001–2006, *J. Geophys. Res.*, 115(D22309), doi:10.1029/2010JD014180, 2010.

	ESA Climate Change Initiative (CCI)	Page 84
	Climate Assessment Report (CAR)	
	for the Essential Climate Variable (ECV) Greenhouse Gases (GHG)	Version 4 (final)
		28 March 2017

Bergamaschi, P., S. Houweling, A. Segers, M. Krol, C. Frankenberg, R. A. Scheepmaker, E. Dlugokencky, S. Wofsy, E. Kort, C. Sweeney, T. Schuck, C. Brenninkmeijer, H. Chen, V. Beck and C. Gerbig, Atmospheric CH₄ in the first decade of the 21st century: Inverse modeling analysis using SCIAMACHY satellite retrievals and NOAA surface measurements, *J. Geophys. Res.*, 118, doi:10.1002/jgrd.50480, 2013.

Bloom, A. A., Palmer, P. I., Fraser, A., and Reay, D. S.: Seasonal variability of tropical wetland CH₄ emissions: the role of the methanogen-available carbon pool, *Biogeosciences*, 9, 2821–2830, doi:10.5194/bg-9-2821-2012, 2012

Boden, T. A., Marland, G., and Andres, R. J.: Global, regional, and national fossil-fuel CO₂ emissions. Carbon Dioxide Information Analysis Center, Oak Ridge National Laboratory, U.S. Department of Energy, Oak Ridge, Tenn., U.S.A., Doi:10.3334/CDIAC/00001_V2013, 2013

Buchwitz, M., M. Reuter, O. Schneising, et al., The Greenhouse Gas Climate Change Initiative (GHG-CCI): comparison and quality assessment of near-surface-sensitive satellite-derived CO₂ and CH₄ global data sets, *Remote Sensing of Environment*, 162, 344–362, doi:10.1016/j.rse.2013.04.024, 2015.

Buchwitz, M., Dils, B., Boesch, H., et al., Product Validation and Intercomparison Report (PVIR) for the GHG-CCI project of ESA's Climate Change Initiative, version 3.1 (PVIRv4), 24 February 2016, http://www.esa-ghg-cci.org/index.php?q=webfm_send/300, 2016.

Buchwitz, M., Dils, B., Boesch, H., et al., Product Validation and Intercomparison Report (PVIR) for the for the Essential Climate Variable (ECV) Greenhouse Gases (GHG) for data set Climate Research Data Package No. 4 (CRDP#4), 9 February 2017, <http://www.esa-ghg-cci.org/>, 2017a.


Buchwitz, M., M. Reuter, O. Schneising, W. Hewson, R.G. Detmers, H. Boesch, O.P. Hasekamp, I. Aben, H. Bovensmann, J.P. Burrows, A. Butz, F. Chevallier, B. Dils, C. Frankenberg, J. Heymann, G. Lichtenberg, M. De Mazière, J. Notholt, R. Parker, T. Warneke, C. Zehner, D.W.T. Griffith, N.M. Deutscher, A. Kuze, H. Suto, D. Wunch, 2017: Global satellite observations of column-averaged carbon dioxide and methane: The GHG-CCI XCO₂ and XCH₄ CRDP3 data set, *Remote Sensing of Environment*, doi: 10.1016/j.rse.2016.12.027, accepted, 2017b.

Butz, A., Guerlet, S., Hasekamp, O., et al., Toward accurate CO₂ and CH₄ observations from GOSAT, *Geophys. Res. Lett.*, doi:10.1029/2011GL047888, 2011.

Canadell, J. G., Ciais, P., Dhakal, S., et al., Interactions of the carbon cycle, human activity, and the climate system: a research portfolio, *Curr. Opin. Environ. Sustainabil.*, 2, 301–311, 2010.

Chevallier, F., et al.: Inferring CO₂ sources and sinks from satellite observations: method and application to TOVS data. *J. Geophys. Res.*, 110, D24309, 2005.

Chevallier, F.: Impact of correlated observation errors on inverted CO₂ surface fluxes from OCO measurements, *Geophys. Res. Lett.*, 34, L24804, doi:10.1029/2007GL030463, 2007.

	ESA Climate Change Initiative (CCI)		Page 85
	Climate Assessment Report (CAR)		
	for the Essential Climate Variable (ECV) Greenhouse Gases (GHG)		Version 4 (final)
			28 March 2017

Chevallier, F., Maksyutov, S., Bousquet, P., Bréon, F.-M., Saito, R., Yoshida, Y., and Yokota, T.: On the accuracy of the CO₂ surface fluxes to be estimated from the GOSAT observations. *Geophys. Res. Lett.*, 36, L19807, doi:10.1029/2009GL040108, 2009.

Chevallier, F., et al.: CO₂ surface fluxes at grid point scale estimated from a global 21-year reanalysis of atmospheric measurements. *J. Geophys. Res.*, 115, D21307, doi:10.1029/2010JD013887, 2010a.

Chevallier, F., Feng, L., Boesch, H., Palmer, P., and Rayner, P.: On the impact of transport model errors for the estimation of CO₂ surface fluxes from GOSAT observations. *Geophys. Res. Lett.*, 37, L21803, doi:10.1029/2010GL044652, 2010b.

Chevallier, F., Deutscher, N. M., Conway, T. J., Ciais, P., Ciattaglia, L., Dohe, S., Frohlich, M., Gomez-Pelaez, A. J., Griffith, D., Hase, F., Haszpra, L., Krummel, P., Kyro, E., Labuschagne, C., Langenfelds, R., Machida, T., Maignan, F., Matsueda, H., Morino, I., Notholt, J., Ramonet, M., Sawa, Y., Schmidt, M., Sherlock, V., Steele, P., Strong, K., Sussmann, R., Wennberg, P., Wofsy, S., Worthy, D., Wunch, D., and Zimnoch, M.: Global CO₂ fluxes inferred from surface air-sample measurements and from TCCON retrievals of the CO₂ total column, *Geophys. Res. Lett.*, 38, L24810, doi:10.1029/2011GL049899, 2011

Chevallier, F., Bergamaschi, P., Kaminiski, T., Scholze, M., Climate Assessment Report (CAR) for the GHG-CCI project of ESA's Climate Change Initiative, version 1.1 (CARv1.1), 18. Nov. 2013, http://www.esa-ghg-cci.org/index.php?q=webfm_send/153, 2013.


Chevallier, F., and O'Dell, C. W., Error statistics of Bayesian CO₂ flux inversion schemes as seen from GOSAT, *Geophys. Res. Lett.*, doi: 10.1002/grl.50228, 2013.

Chevallier, F., Palmer, P.I., Feng, L., Boesch, H., O'Dell, C.W., Bousquet, P., Towards robust and consistent regional CO₂ flux estimates from in situ and space-borne measurements of atmospheric CO₂, *Geophys. Res. Lett.*, 41, 1065-1070, DOI: 10.1002/2013GL058772, 2014a.

Chevallier, F., Buchwitz, M., Bergamaschi, et al., User Requirements Document for the GHG-CCI project of ESA's Climate Change Initiative, version 2 (URDv2), 28. August 2014, http://www.esa-ghg-cci.org/?q=webfm_send/173, 2014b.

Chevallier, F., P. Bergamaschi, D. Brunner, S. Gonzi, S. Houweling, T. Kaminski, G. Kuhlmann, T. T. van Leeuwen, J. Marshall, P. I. Palmer, and M. Scholze, Climate Assessment Report for the GHG-CCI project of ESA's Climate Change Initiative, pp. 87, version 2, 22 April 2015, http://www.esa-ghg-cci.org/?q=webfm_send/256, 2015.

Chevallier, F., M. Alexe, P. Bergamaschi, D. Brunner, L. Feng, S. Houweling, T. Kaminski, W. Knorr, T. T. van Leeuwen, J. Marshall, P. I. Palmer, M. Scholze, A.-M. Sundström and M. Voßbeck, Climate Assessment Report for the GHG-CCI project of ESA's Climate Change Initiative, pp. 94, version 3, 3 May 2016, 2016.

	ESA Climate Change Initiative (CCI)		Page 86
	Climate Assessment Report (CAR)		
	for the Essential Climate Variable (ECV) Greenhouse Gases (GHG)		Version 4 (final)
			28 March 2017

Cogan, A. J., Boesch, H., Parker, R. J., et al., Atmospheric carbon dioxide retrieved from the Greenhouse gases Observing SATellite (GOSAT): Comparison with ground-based TCCON observations and GEOS-Chem model calculations, *J. Geophys. Res.*, 117, D21301, doi:10.1029/2012JD018087, 2012.

Conway, T. J., Tans, P. P., Waterman, L. S., Thoning, K. W., Kitzis, D. R., Masarie, K. A. and Zhang, N.: Evidence for interannual variability of the carbon cycle from the National Oceanic and Atmospheric Administration/Climate Monitoring and Diagnostics Laboratory Global Air Sampling Network, *J. Geophys. Res.*, 99(D11), 22,831–22,855, doi:10.1029/94JD01951, 1994

Cramer, W., Kicklighter, D. W., Bondeau, A., Iii, B. M., Churkina, G., Nemry, B., Ruimy, A., Schloss, A. L. and Intercomparison, ThE. P. OF. ThE. P. NpP. M., Comparing global models of terrestrial net primary productivity (NPP): overview and key results. *Global Change Biology*, 5: 1–15. doi:10.1046/j.1365-2486.1999.00009.x, 1999.

Cressot, C., F. Chevallier, P. Bousquet, et al., On the consistency between global and regional methane emissions inferred from SCIAMACHY, TANSO-FTS, IASI and surface measurements, *Atmos. Chem. Phys.*, 14, 577-592, 2014.

Cressot, C., Pison, I., Rayner, P. J., Bousquet, P., Fortems-Cheiney, A., and Chevallier, F.: Can we detect regional methane anomalies? A comparison between three observing systems, *Atmos. Chem. Phys.*, 16, 9089-9108, doi:10.5194/acp-16-9089-2016, 2016..

Crevoisier, C., Sweeney, C., Gloor, M., Sarmiento, J. L., and Tans, P. P.: Regional U.S. carbon sinks from three-dimensional atmospheric CO₂ sampling, *Proc. Natl. Acad. Sci.* (2010), 107: 18348-18353, 2010.

Dee, D. P., et al., The ERA-Interim reanalysis: configuration and performance of the data assimilation system, *Q. J. R. Meteorol. Soc.*, 137, 553–597, 2011.


Desroziers G., Berre, L., Chapnik, B., and Poli, P.: Diagnosis of observation, background and analysis error statistics in observation space. *Q. J. Roy. Meteor. Soc.*, 131, 3385-3396, 2005.

Detmers, R., Hasekamp, O., Aben, I., Houweling, S., van Leeuwen, T.T., Butz, A., Landgraf, J., Kohler, P., Guanter, L., and Poulter, B.: Anomalous carbon uptake in Australia as seen by GOSAT. *Geophysical Research Letters*, 42(19), 2015

Dlugokencky, E. J., L. P. Steele, P. M. Lang, and K. A. Masarie, The growth rate and distribution of atmospheric methane, *J. Geophys. Res.*, 99, 17021–17043. 1994.

Dlugokencky, E. J., S. Houweling, L. Bruhwiler, K. A. Masarie, P.M. Lang, J. B. Miller, and P. P. Tans, Atmospheric methane levels off: Temporary pause or a new steady-state? *Geophys. Res. Lett.*, 30(19), 1992, doi:10.1029/2003GL018126, 2003.

Dlugokencky, E. J., Bruhwiler, L., White, J. W. C., et al., Observational constraints on recent increases in the atmospheric CH₄ burden, *Geophys. Res. Lett.*, 36, L18803, doi:10.1029/2009GL039780, 2009.

	ESA Climate Change Initiative (CCI)		Page 87
	Climate Assessment Report (CAR)		
	for the Essential Climate Variable (ECV) Greenhouse Gases (GHG)		Version 4 (final)
			28 March 2017

Dlugokencky, E., P. Lang, J. Mund, A. Crotwell, M. Crotwell, and K. Thoning, Atmospheric carbon dioxide dry air mole fractions from the NOAA ESRL carbon cycle cooperative global air sampling network, 1968-2015, 2016.

Dubovik, O. and King, M. D.: A flexible inversion algorithm for retrieval of aerosol optical properties from Sun and sky radiance measurements, *J. Geophys. Res.*, 105, 20673–20696, 2000.

Enting, I. G.: Inverse Problems in Atmospheric Constituent Transport. Cambridge University Press, 2002.

ESA: A-SCOPE - Advanced Space Carbon And Climate Observation of Planet Earth, Technical Report SP-1313/1, European Space Agency, Noordwijk, The Netherlands. 2008

Feng, L., Palmer, P. I., Bösch, H., and Dance, S.: Estimating surface CO₂ fluxes from space-borne CO₂ dry air mole fraction observations using an ensemble Kalman Filter, *Atmos. Chem. Phys.*, 9, 2619–2633, doi:10.5194/acp-9-2619-2009, 2009.

Feng, L., P. I. Palmer, R. J. Parker, et al., Estimates of European uptake of CO₂ inferred from GOSAT X_{CO2} retrievals: sensitivity to measurement bias inside and outside Europe, *Atmos. Chem. Phys.*, 16, 1289-1302, doi:10.5194/acp-16-1289-2016, 2016a.


Feng, L., Palmer, P. I., Bösch, H., Parker, R. J., Webb, A. J., Correia, C. S. C., Deutscher, N. M., Domingues, L. G., Feist, D. G., Gatti, L. V., Gloor, E., Hase, F., Kivi, R., Liu, Y., Miller, J. B., Morino, I., Sussmann, R., Strong, K., Uchino, O., Wang, J., and Zahn, A.: Consistent regional fluxes of CH₄ and CO₂ inferred from GOSAT proxy XCH₄:XCO₂ retrievals, 2010–2014, *Atmos. Chem. Phys. Discuss.*, doi:10.5194/acp-2016-868, in review, 2016b. Frankenberg, C., Aben, I., Bergamaschi, P., et al., Global column-averaged methane mixing ratios from 2003 to 2009 as derived from SCIAMACHY: Trends and variability, *J. Geophys. Res.*, doi:10.1029/2010JD014849, 2011.

Frankenberg, C., Product User Guide (PUG) for the IMAP-DOAS XCH₄ SCIAMACHY Data Products, version 1, ESA Climate Change Initiative (CCI) GHG-CCI project, 13 Dec. 2012, 2012. http://www.esa-ghg-cci.org/sites/default/files/documents/public/documents/PUG_GHG-CCI_draft_IMAPcfranken_v1.pdf

Fraser, A., Palmer, P. I., Feng, L., et al., Estimating regional methane surface fluxes: the relative importance of surface and GOSAT mole fraction measurements, *Atmos. Chem. Phys.*, 13, 5697-5713, doi:10.5194/acp-13-5697-2013, 2013.

Fraser, A., Palmer, P. I., Feng, L. et al., Estimating regional fluxes of CO₂ and CH₄ using space-borne observations of XCH₄:XCO₂, *Atmos. Chem. Phys.*, 14, 12883-12895, doi:10.5194/acp-14-12883-2014, 2014.

Friedl, M. A., Strahler, A. H., and Hodges, J.: ISLSCP II MODIS (Collection 4) IGBP Land Cover, 2000–2001, in: ISLSCP Initiative II Collection, Data set, edited by: Hall, F. G., Collatz, G., Meeson, B., Los, S.,

	ESA Climate Change Initiative (CCI) Climate Assessment Report (CAR) for the Essential Climate Variable (ECV) Greenhouse Gases (GHG)	Page 88
		Version 4 (final)
		28 March 2017

Brown de Colstoun, E., and Landis, D., Oak Ridge National Laboratory Distributed Active Archive Center, Oak Ridge, Tennessee, USA, doi:10.3334/ORNLDAAC/96

Gatti, L. V., Gloor, M., Miller, J. B., Doughty, C. E., Malhi, Y., Domingues, L. G., Basso, L. S., Martinewski, A., Correia, C. S. C., Borges, V. F., Freitas, S., Braz, R., Anderson, L. O., Rocha, H., Grace, J., Philips, O. L., and Lloyd, J.: Drought sensitivity of Amazonian carbon balance revealed by atmospheric measurements, *Nature*, 506(7486), 76-80, doi:10.1038/nature12957, 2014

Giles, D.M., Holben, B.N., Eck, T.F., Sinyuk, A., Smirnov, A., Slutsker, I., Dickerson, R. R., Thompson, A.M., and Shafer J. S.: An analysis of AERONET aerosol absorption properties and classifications representative of aerosol source regions, *J. Geophys. Res.*, 117, D17203, 2012.

GLOBALVIEW-CO2: Cooperative Global Atmospheric Data Integration Project. 2013, updated annually. Multi-laboratory compilation of synchronized and gap-filled atmospheric carbon dioxide records for the period 1979-2012 (obspack_co2_1_GLOBALVIEW-CO2_2013_v1.0.4_2013-12-23). Compiled by NOAA Global Monitoring Division: Boulder, Colorado, U.S.A. Data product accessed at <http://dx.doi.org/10.3334/OBSPACK/1002>. 2013

Gerbig, C., Lin, J. C., Wofsy, S. C., Daube, B. C., Andrews, A. E., Stephens, B. B., Bakwin, P. S., and Grainger, C. A.: Toward constraining regional-scale fluxes of CO₂ with atmospheric observations over a continent: 2. Analysis of COBRA data using a receptor-oriented framework, *J. Geophys. Res.-Atmos.*, 108, 4757, doi:10.1029/2003JD003770, 2003.

Guerlet, S., Basu, S., Butz, A., et al., Reduced carbon uptake during the 2010 Northern Hemisphere summer from GOSAT, *Geophys. Res. Lett.*, doi: 10.1002/grl.50402, 2013a.


Guerlet, S., Butz, A., Scheppers, D., Basu, S., Hasekamp, O.P., Kuze, A., Yokota, T., Blavier, J.-F., Deutcher, N.M., Griffith, D.W.T, Hase, F., Kyrö, E., Morino, I, Scherlock, V., Sussmann, R., Galli, A., and Aben, I.: Impact of aerosol and thin cirrus on retrieving and validating XCO₂ from GOSAT shortwave infrared measurements. *J. Geophys. Res.*, 118, 4887-4905, 2013b.

Gurney, K.R., et al.: Towards robust regional estimates of CO₂ sources and sinks using atmospheric transport models. *Nature*, 415:6872, 626-630, 2002.

Harris, I., Jones, P.D., Osborn, T.J. and Lister, D.H., Updated high-resolution grids of monthly climatic observations – the CRU TS3.10 Dataset. *Int. J. Climatol.* doi: 10.1002/joc.3711, 2013

Haverd, V., Raupach, M. R., Briggs, P. R., J. G. Canadell., Davis, S. J., Law, R. M., Meyer, C. P., Peters, G. P., Pickett-Heaps, C., and Sherman, B.: The Australian terrestrial carbon budget, *Biogeosciences*, 10, 851-869, doi:10.5194/bg-10-851-2013, 2013.

Hayman, G. D., O'Connor, F. M., Dalvi, et al., Comparison of the HadGEM2 climate-chemistry model against in-situ and SCIAMACHY atmospheric methane data, *Atmos. Chem. Phys.*, 14, 13257-13280, doi:10.5194/acp-14-13257-2014, 2014.

	ESA Climate Change Initiative (CCI)		Page 89
	Climate Assessment Report (CAR)		
	for the Essential Climate Variable (ECV) Greenhouse Gases (GHG)		Version 4 (final)
			28 March 2017

Heimann, M.: The global atmospheric tracer model TM2, Technical Report No. 10, Max-Planck-Institut für Meteorologie, Hamburg, Germany. 1995

Heimann, M., G. Esser, A. Haxeltine, J. Kaduk, D.W. Kicklighter, W. Knorr, G. H. Kohlmaier, A. D. McGuire, J. Melillo, B. Moore, et al., Evaluation of terrestrial carbon cycle models through simulations of the seasonal cycle of atmospheric CO₂: First results of a model intercomparison study, *Global Biogeochemical Cycles*, 12, 1–24, 1998.

Heimann, M. and S. Körner: The global atmospheric tracer model TM3. In: Max-Planck-Institut für Biogeochemie (Eds.): Technical Report. Vol. 5. Max-Planck-Institut für Biogeochemie, Jena. pp. 131, 2003.

Hewson, W.: ESA Climate Change Initiative (CCI) Product User Guide: University of Leicester full-physics XCO₂ retrieval algorithm for CRDP3–OCFPv6.0 for the Essential Climate Variable (ECV): Greenhouse Gases (GHG), Version 3, 25 February 2016, 2016.

Heymann, J., Schneising, O., Reuter, M., et al., SCIAMACHY WFM-DOAS XCO₂: comparison with CarbonTracker XCO₂ focusing on aerosols and thin clouds, *Atmos. Meas. Tech.*, 5, 1935–1952, 2012.

Holben, B., Eck, T. F., Slutsker, I., Tanre, D., Buis, J. P., Setzer, A., Vermote, E., Reagan, J. A., Kaufman, Y. J., Nakajima, T., Lavenue, F., Jankowiak, I., and Smirnov, A.: AERONET – A Federated Instrument Network and Data Archive for Aerosol Characterization, *Remote Sens. Environ.*, 66, 1–16, 1998.


Hourdin, F., et al.: The LMDZ4 general circulation model: climate performance and sensitivity to parametrized physics with emphasis on tropical convection, *Climate Dynamics*, 27, 787–813, doi:10.1007/s00382-006-0158-0, 2006.

Houweling, S., et al.: The importance of transport model uncertainties for the estimation of CO₂ sources and sinks using satellite measurements. *Atmos. Chem. Phys.*, 10, 9981–9992, doi:10.5194/acp-10-9981-2010, 2010.

Houweling, S., M. Krol, P. Bergamaschi, C. Frankenberg, E. J. Dlugokencky, I. Morino, J. Notholt, V. Sherlock, D. Wunch, V. Beck, C. Gerbig, H. Chen, E. A. Kort, T. Röckmann and I. Aben, A multi-year methane inversion using SCIAMACHY, accounting for systematic errors using TCCON measurements, *Atmos. Chem. Phys.*, 14, 3991–4012, doi:10.5194/acp-14-3991-2014, 2014.

Houweling, S., D. Baker, S. Basu, H. Boesch, A. Butz, F. Chevallier, F. Deng, E. Dlugokencky, L. Feng, A. Ganshin, O. P. Hasekamp, D. Jones, S. Maksyutov, J. Marshall, T. Oda, C. O'Dell, S. Oshchepkov, P. Paul, P. Peylin, Z. Poussi, F. Reum, H. Takagi, Y. Yoshida, R. Zhuravlev, An inter-comparison of inverse models for estimating sources and sinks of CO₂ using GOSAT measurements. *J. Geophys. Res. Atmos.*, 120, 5253–5266, doi:10.1002/2014JD022962, 2015.

Jacobson, A. R., Fletcher, S. E. M., Gruber, N., Sarmiento, J. L., and Gloor, M.: A joint atmosphere-ocean inversion for surface fluxes of carbon dioxide: 1. Methods and global-scale fluxes, *Global Biogeochem. Cy.*, 21(1), GB1020, doi:10.1029/2006GB002703, 2007.

	ESA Climate Change Initiative (CCI) Climate Assessment Report (CAR) for the Essential Climate Variable (ECV) Greenhouse Gases (GHG)	Page 90
		Version 4 (final)
		28 March 2017

Jung, M., et al.: Global patterns of land-atmosphere fluxes of carbon dioxide, latent heat, and sensible heat derived from eddy covariance, satellite, and meteorological observations, *J. Geophys. Res.*, 116, G00J07, doi:10.1029/2010JG001566. 2011.

Kaminski, T., W. Knorr, P. Rayner, and M. Heimann.: Assimilating atmospheric data into a terrestrial biosphere model: A case study of the seasonal cycle. *Global Biogeochemical Cycles*, 16(4):14-1-14-16, 2002.

Kaminski, T. and P. Rayner. Assimilation and Network Design. H. Dolman, A Freibauer, and R. Valentini, editors, *Observing the continental scale Greenhouse Gas Balance of Europe. Ecological Studies Series*. Springer. 2008.

Kaminski, T., M. Scholze, and S. Houweling. Quantifying the Benefit of A-SCOPE Data for Reducing Uncertainties in Terrestrial Carbon Fluxes in CCDAS. *Tellus B*, 62(5):784-796, 2010.

Kaminski, T., P. J. Rayner, M. Voßbeck, M. Scholze, and E. Koffi. Observing the continental-scale carbon balance: assessment of sampling complementarity and redundancy in a terrestrial assimilation system by means of quantitative network design. *Atmospheric Chemistry and Physics*, 12(16):7867-7879, 2012.

Kaminski, T., W. Knorr, G. Schürmann, M. Scholze, P. J. Rayner, S. Zaehle, S. Blessing, W. Dorigo, V. Gayler, R. Giering, N. Gobron, J. P. Grant, M. Heimann, A. Hooker-Strout, S. Houweling, T. Kato, J. Kattge, D. Kelley, S. Kemp, E. N. Koffi, C. Köstler, P.P. Mathieu, B. Pinty, C. H. Reick, C. Rödenbeck, R. Schnur, K. Scipal, C. Sebal, T. Stacke, A. Terwisscha van Scheltinga, M. Vossbeck, H. Widmann, and T. Ziehn: The BETHY/JSBACH Carbon Cycle Data Assimilation System: experiences and challenges. *J. Geophys. Res.*, 118:doi:10.1002/jgrg.20118, 2013.


Kaminski, T., B. Pinty, M. Voßbeck, M. Lopatka, N. Gobron, and M. Robustelli, Consistent EO Land Surface Products including Uncertainty Estimates, *Biogeosciences Discussions*, 2016, 1–28, doi:10.5194/bg-2016-310, 2016.

Keeling, C., S. Piper, and Scripps Institution of Oceanography, Exchanges of Atmospheric CO₂ and 13CO₂ with the Terrestrial Biosphere and Oceans from 1978 to 2000, SIO reference, Scripps Institution of Oceanography, University of California, San Diego, 2001.

Kicklighter, D. W., Bondeau, A., Schloss, A. L., Kaduk, J., Mcguire, A. D. et al., Comparing global models of terrestrial net primary productivity (NPP): global pattern and differentiation by major biomes. *Global Change Biology*, 5: 16–24. doi:10.1046/j.1365-2486.1999.00003.x, 1999.

Kirschke, S., Bousquet, P., Ciais, P., et al., Three decades of global methane sources and sinks, *Nat. Geosci.*, 6, 813–823, doi:10.1038/ngeo1955, 2013.

Knorr, W., and M. Heimann: Impact of drought stress and other factors on seasonal land biosphere CO₂ exchange studied through an atmospheric tracer transport model. *Tellus*, Ser. B, 47(4):471–489, 1995.

	ESA Climate Change Initiative (CCI)	Page 91
	Climate Assessment Report (CAR)	
	for the Essential Climate Variable (ECV) Greenhouse Gases (GHG)	Version 4 (final)
		28 March 2017

Knorr, W. Annual and interannual CO₂ exchanges of the terrestrial biosphere: process based simulations and uncertainties. *Glob. Ecol. and Biogeogr.* 9, 225–252. 2000.

Knorr, W., Kaminski, T., Arneth, A., and Weber, U.: Impact of human population density on fire frequency at the global scale, *Biogeosciences*, 11, 1085-1102, doi:10.5194/bg-11-1085-2014, 2014.

Kort, E. A., Frankenberg, C., Costigan, K. R., et al., Four corners: The largest US methane anomaly viewed from space, *Geophys. Res. Lett.*, 41, doi:10.1002/2014GL061503, 2014.

Krol, M. C., S. Houweling, B. Bregman, M. van den Broek, A. Segers, P. van Velthoven, W. Peters, F. Dentener, and P. Bergamaschi, The two-way nested global chemistry-transport zoom model TM5: algorithm and applications, *Atmos. Chem. Phys.*, 5, 417-432, 2005.

Lindqvist, H., C. W. O'Dell, S. Basu, H. Boesch, F. Chevallier, N. Deutscher, L. Feng, B. Fisher, F. Hase, M. Inoue, R. Kivi, I. Morino, P. I. Palmer, R. Parker, M. Schneider, R. Sussmann, and Y. Yoshida, Does GOSAT capture the true seasonal cycle of carbon dioxide?, *Atmos. Chem. Phys.*, 15, 13023-13040, doi:10.5194/acp-15-13023-2015, 2015.

Ma, X., A. Huete, J. Cleverly, D. Eamus, F. Chevallier, J. Joiner, B. Poulter, Y. Zhang, L. Guanter, W. Meyer, Z. Xie, G. Ponce-Campos: Drought rapidly disseminates the 2011 large CO₂ uptake in semi-arid Australia. *Scientific Reports*, 6. doi: 10.1038/srep37747, 2016.

Mäder, J. A., J. Staehelin, D. Brunner, W. A. Stahel, I. Wohltmann, and T. Peter, Statistical modeling of total ozone: Selection of appropriate explanatory variables, *J. Geophys. Res.*, 112, D11108, doi:10.1029/2006JD007694, 2007.


Meirink, J. F., P. Bergamaschi, and M. Krol: Four-dimensional variational data assimilation for inverse modelling of atmospheric methane emissions: Method and comparison with synthesis inversion, *Atmos. Chem. Phys.*, 8, 6341–6353, 2008.

Mikaloff Fletcher, S. E., Gruber, N., Jacobson, A. R., Doney, S. C., Dutkiewicz, S., and co-authors: Inverse estimates of anthropogenic CO₂ uptake, transport, and storage by the ocean, *Global Biogeochem. Cy.*, 20(2), GB2002, doi:10.1029/2005GB002530, 2006.

Mikaloff Fletcher, S. E., Gruber, N., Jacobson, A. R., Gloor, M., Doney, S. C., and co-authors: Inverse estimates of the oceanic sources and sinks of natural CO₂ and the implied oceanic carbon transport, *Global Biogeochem. Cy.*, 21(1), GB1010, doi:10.1029/2006GB002751, 2007.

Monteil, G., Houweling, S., Butz, A., et al., Comparison of CH₄ inversions based on 15 months of GOSAT and SCIAMACHY observations, *J. Geophys. Res.*, doi: 10.1002/2013JD019760, Vol 118, Issue 20, 11807-11823, 2013.

Notholt, J., et al.: Product Validation and Intercomparison Report (PVIR), ESA Climate Change Initiative (CCI) GHG-CCI project, v2.0, 4 Nov. 2013, 2013. http://www.esa-ghg-cci.org/index.php?q=webfm_send/152

	ESA Climate Change Initiative (CCI)	Page 92
	Climate Assessment Report (CAR)	
	for the Essential Climate Variable (ECV) Greenhouse Gases (GHG)	Version 4 (final)
		28 March 2017

O'Dell, C. W., Connor, B., Bösch, H., O'Brien, D., Frankenberg, C., Castano, R., Christi, M., Eldering, D., Fisher, B., Gunson, M., McDuffie, J., Miller, C. E., Natraj, V., Oyafuso, F., Polonsky, I., Smyth, M., Taylor, T., Toon, G. C., Wennberg, P. O., and Wunch, D.: The ACOS CO₂ retrieval algorithm – Part 1: Description and validation against synthetic observations, *Atmos. Meas. Tech.*, 5, 99–121, doi:10.5194/amt-5-99-2012, 2012.

O'Neill, N. T., T. F., Eck, A., Smirnov, B. N., Holben, S., Thulasiraman, Spectral discrimination of coarse and fine mode optical depth, *J. Geophys. Res.*, 108, D17, 4559–4573, doi:10.1029/2002JD002975, 2003.

Oda, T., and Maksyutov, S.: A very high-resolution (1 km×1 km) global fossil fuel CO₂ emission inventory derived using a point source database and satellite observations of nighttime lights, *Atmos. Chem. Phys.*, 11, 543–556, doi:10.5194/acp-11-543-2011, 2011.

Olivier, J. G. J., van Aardenne, J. A., Dentener, F., Ganzeveld, L., and Peters, J. A. H. W.: Recent trends in global greenhouse gas emissions: regional trends and spatial distribution of key sources, in: Non-CO₂ Greenhouse Gases (NCGG-4), edited by: van Amstel, A., Millpress, Rotterdam, 325–330, 2005.

Olivier, J. G. J., Janssens-Maenhout, G., and Peters, J. A. H. W., Trends in global CO₂ emissions, 2012 Report, PBL Netherlands Environmental Assessment Agency, The Hague, Joint Research Centre, Ispra, ISBN 978-92-79-25381-2, 2012.

Olsen, S. C. and Randerson, J. T.: Differences between surface and column atmospheric CO₂ and implications for carbon cycle research, *J. Geophys. Res.*, 109, D02301, doi:10.1029/2003JD003968, 2004.


Oshchepkov, S., A. Bril, T. Yokota, et al., Effects of atmospheric light scattering on spectroscopic observations of greenhouse gases from space. Part 2: Algorithm intercomparison in the GOSAT data processing for CO₂ retrievals over TCCON sites, *J. Geophys. Res.*, 118, 1493–1512, doi:10.1002/jgrd.50146, 2013.

Pan, Y., et al.: A large and persistent carbon sink in the world's forests, *Science*, 333, 988–993, 2011.

Pandey, S., Houweling, S., Krol, M., Aben, I., Chevallier, F., Dlugokencky, E. J., Gatti, L. V., Gloor, M., Miller, J. B., Detmers, R., Machida, T., and Röckmann, T.: Inverse modeling of GOSAT-retrieved ratios of total column CH₄ and CO₂ for 2009 and 2010, *Atmos. Chem. Phys. Discuss.*, doi:10.5194/acp-2016-77, in review, 2016.

Parazoo, N. C., Bowman, K., Frankenberg, C., et al., Interpreting seasonal changes in the carbon balance of southern Amazonia using measurements of XCO₂ and chlorophyll fluorescence from GOSAT, *Geophys. Res. Lett.*, 40, 2829–2833, doi:10.1002/grl.50452, 2013.

Parker, R., Boesch, H., Cogan, A., et al., Methane Observations from the Greenhouse gases Observing SATellite: Comparison to ground-based TCCON data and Model Calculations, *Geophys. Res. Lett.*, doi:10.1029/2011GL047871, 2011.

	ESA Climate Change Initiative (CCI)		Page 93
	Climate Assessment Report (CAR)		
	for the Essential Climate Variable (ECV) Greenhouse Gases (GHG)		Version 4 (final)
			28 March 2017

Peters, W., Jacobson, A. R., Sweeney, C., et al.: An atmospheric perspective on North American carbon dioxide exchange: CarbonTracker, *Proceedings of the National Academy of Sciences (PNAS)* of the United States of America, 27 Nov. 2007, 104(48), 18925-18930, 2007.

Peylin, P., Law, R. M., Gurney, et al., Global atmospheric carbon budget: results from an ensemble of atmospheric CO₂ inversions, *Biogeosciences*, 10, 6699–6720, doi:10.5194/bg-10-6699-2013, URL <http://www.biogeosciences.net/10/6699/2013/>, 2013.

Pinty, B., T. Lavergne, M. Voßbeck, T. Kaminski, O. Aussedat, R. Giering, N. Gobron, M. Taberner, M. M. Verstraete, and J.-L. Widlowski, Retrieving surface parameters for climate models from MODIS-MISR albedo products. *J. Geophys. Res.*, 112, 2007.

Pinty, B., M. Clerici, I. Andredakis, T. Kaminski, M. Taberner, M. M. Verstraete, N. Gobron, S. Plummer, and J. L. Widlowski. Exploiting the MODIS albedos with the Two-stream Inversion Package (JRC-TIP): 2. Fractions of transmitted and absorbed fluxes in the vegetation and soil layers. *J. Geophys. Res.*, 116:15 PP, 2011.

Poulter, B., Frank, D., Ciais, P., Myneni, R. B., Andela, N., Bi, J., Broquet, G. Canadell, J.G. Chevallier, F. Liu, Y. Y., Running, S. W., Sitch, S., and van der Werf, G. R.: Contribution of semi-arid ecosystems to interannual variability of the global carbon cycle. *Nature*, doi:10.1038/nature13376, 2014.

PSDv3, Product Specification Document (PSD) for the Essential Climate Variable (ECV) Greenhouse Gases (GHG) - Description of Common Parameters for core (ECA) products, Version 3, 6 June 2014. http://www.esa-ghg-cci.org/index.php?q=webfm_send/160


Rayner, P.J., M. Scholze, W. Knorr, T. Kaminski and R. Giering: Two decades of terrestrial Carbon fluxes from a Carbon Cycle Data Assimilation System (CCDAS). *Global Biogeochemical Cycles*, 19, doi:10.1029/2004GB002254, 2005.

Reuter, M., Bovensmann, H., Buchwitz, M., et al., Retrieval of atmospheric CO₂ with enhanced accuracy and precision from SCIAMACHY: Validation with FTS measurements and comparison with model results, *J. Geophys. Res.*, 116, D04301, doi:10.1029/2010JD015047, 2011.

Reuter, M., Boesch, H., Bovensmann, H., et al., A joint effort to deliver satellite retrieved atmospheric CO₂ concentrations for surface flux inversions: the ensemble median algorithm EMMA, *Atmos. Chem. Phys.*, 13, 1771-1780, 2013.

Reuter, M., M. Buchwitz, M. Hilker, et al., Satellite-inferred European carbon sink larger than expected, *Atmos. Chem. Phys.*, 14, 13739-13753, doi:10.5194/acp-14-13739-2014, 2014a.

Reuter, M., M. Buchwitz, A. Hilboll, et al., Decreasing emissions of NO_x relative to CO₂ in East Asia inferred from satellite observations, *Nature Geoscience*, 28 Sept. 2014, doi:10.1038/ngeo2257, pp.4, 2014b.

	ESA Climate Change Initiative (CCI)	Page 94
	Climate Assessment Report (CAR)	
	for the Essential Climate Variable (ECV) Greenhouse Gases (GHG)	Version 4 (final)
		28 March 2017

Reuter, M.: ESA Climate Change Initiative (CCI) Product User Guide version 4 (PUGv4) for the XCO₂ SCIAMACHY Data Product BESD for the Essential Climate Variable (ECV): Greenhouse Gases (GHG), 31 August 2016, 2016a.

Reuter, M., M. Hilker, O. Schneising, M. Buchwitz, J. Heymann ESA Climate Change Initiative (CCI) Comprehensive Error Characterisation Report: BESD full-physics retrieval algorithm for XCO₂ for the Essential Climate Variable (ECV) Greenhouse Gases (GHG) Version 2.0, revision 1. 2016b.

Reuter, M., M. Buchwitz, M. Hilker, J. Heymann, H. Bovensmann, J. P. Burrows, S. Houweling, Y. Y. Liu, R. Nassar, F. Chevallier, et al., How much CO₂ is taken up by the European terrestrial biosphere?, *Bulletin of the American Meteorological Society*, 0(0), doi:10.1175/BAMS-D-15-00310.1, 2016c.

M. Reuter, O. Schneising, M. Buchwitz, J. Heymann: Comprehensive Error Characterisation Report Version 3: BESD full-physics retrieval algorithm for XCO₂ for the Essential Climate Variable (ECV) Greenhouse Gases (GHG), http://www.esa-ghg-cci.org/webfm_send/346, 2017

Rödenbeck, C.: Estimating CO₂ sources and sinks from atmospheric mixing ratio measurements using a global inversion of atmospheric transport, Tech. Rep. 6, Max Planck Institute for Biogeochemistry, Jena, Germany, 2005.

Ross, A. N., Wooster, M. J., Boesch, H., Parker, R., First satellite measurements of carbon dioxide and methane emission ratios in wildfire plumes, *Geophys. Res. Lett.*, 40, 1-5, doi:10.1002/grl.50733, 2013.

Scarle, J. D., Studies in astronomical time series analysis. III. Fourier transforms, autocorrelation functions and cross-correlation functions of unevenly spaced data. *Astrophys. J.*, 343, 874–887, 1989.


Schneising, O., Buchwitz, M., Reuter, M., et al., Long-term analysis of carbon dioxide and methane column-averaged mole fractions retrieved from SCIAMACHY, *Atmos. Chem. Phys.*, 11, 2881-2892, 2011.

Schneising, O., J. Heymann, M. Buchwitz, M. Reuter, H. Bovensmann, and J. P. Burrows, Anthropogenic carbon dioxide source areas observed from space: assessment of regional enhancements and trends, *Atmos. Chem. Phys.*, 13, 2445-2454, 2013.

Schneising, O., M. Reuter, M. Buchwitz, J. Heymann, H. Bovensmann, and J. P. Burrows, Terrestrial carbon sink observed from space: variation of growth rates and seasonal cycle amplitudes in response to interannual surface temperature variability, *Atmos. Chem. Phys.*, 14, 133-141, 2014a.

Schneising, O., J. P. Burrows, R. R. Dickerson, M. Buchwitz, M. Reuter, H. Bovensmann, Remote sensing of fugitive methane emissions from oil and gas production in North American tight geologic formations, *Earth's Future*, 2, DOI: 10.1002/2014EF000265, pp. 11, 2014b.

Scholze, M., T. Kaminski, P. Rayner, W. Knorr, and R. Giering. Propagating uncertainty through prognostic CCDAS simulations. *J. Geophys. Res.*, 112:doi:10.1029/2007JD008642, 2007.

	ESA Climate Change Initiative (CCI)		Page 95
	Climate Assessment Report (CAR)		
	for the Essential Climate Variable (ECV) Greenhouse Gases (GHG)		Version 4 (final)
			28 March 2017

Schulze, E. D., Luyssaert, S., Ciais, P., Freibauer, A., Janssens, I. A., Soussana, J. F., Smith, P., Grace, J., Levin, I., Tiruchittampalam, B., Heimann, M., Dolman, A. J., Valentini, R., Bousquet, P., Peylin, P., Peters, W., Rodenbeck, C., Etiope, G., Vuichard, N., Wattenbach, M., Nabuurs, G. J., Poussi, Z., Nieschulze, J., Gash, J. H., and Team, C.: Importance of methane and nitrous oxide emissions for Europe's terrestrial greenhouse gas balance, *Nat. Geosci.*, 2, 842–850, 2009.

Shindell, D. T., O. Pechony, A. Voulgarakis, et al., Interactive ozone and methane chemistry in GISS-E2 historical and future climate simulations, *Atmos. Chem. Phys.*, 13, 2653–2689, doi:10.5194/acp-13-2653-2013, 2013.

Somkuti, P.: ESA Climate Change Initiative (CCI) Product User Guide version 4.0 (PUGv4.0) for the University of Leicester full-physics XCO₂ GOSAT data product (CO₂_GOS_OCFP version 7) for the Essential Climate Variable (ECV): Greenhouse Gases (GHG), 31 August 2016, 2016.

Sussmann, R., Forster, F., Rettinger, M., and Bousquet, P.: Renewed methane increase for five years (2007–2011) observed by solar FTIR spectrometry, *Atmos. Chem. Phys.*, 12, 4885–4891, doi:10.5194/acp-12-4885-2012, 2012.


Takahashi, T., Sutherland, S. C., Sweeney, C., Poisson, A., Metzl, N., Tilbrook, B., Bates, N., Wanninkhof, R., Feely, R. A., Sabine, C., Olafsson, J., and Nojiri, Y.: Global sea-air CO₂ flux based on climatological surface ocean pCO₂, and seasonal biological and temperature effects, *Deep Sea Res. II*, 49, 1601–1623, 2002.

Takahashi, T., Sutherland, S. C., Wanninkhof, R., et al., Climatological mean and decadal changes in surface ocean pCO₂, and net sea-air CO₂ flux over the global oceans, *Deep-Sea Res. Pt. II*, 56, 554–577, doi:10.1016/j.dsr2.2008.12.009, 2009.

Turner, A. J., Jacob, D. J., Wecht, K. J., Maasakkers, J. D., Lundgren, E., Andrews, A. E., Biraud, S. C., Boesch, H., Bowman, K. W., Deutscher, N. M., Dubey, M. K., Griffith, D. W. T., Hase, F., Kuze, A., Notholt, J., Ohyama, H., Parker, R., Payne, V. H., Sussmann, R., Sweeney, C., Velazco, V. A., Warneke, T., Wennberg, P. O., and Wunch, D.: Estimating global and North American methane emissions with high spatial resolution using GOSAT satellite data, *Atmos. Chem. Phys.*, 15, 7049–7069, doi:10.5194/acp-15-7049-2015, 2015.

Wanninkhof, R., Park, G. -H., Takahashi, T., Sweeney, C., Feely, R., Nojiri, Y., Gruber, N., Doney, S. C., McKinley, G. A., Lenton, A., Le Quéré, C., Heinze, C., Schwinger, J., Graven, H., and Khatiwala, S.: Global ocean carbon uptake: magnitude, variability and trends, *Biogeosciences*, 10, 1983–2000, doi:10.5194/bg-10-1983-2013, 2013.

van der Werf, G. R., Randerson, J. T., Giglio, L., Collatz, G. J., Mu, M., Kasibhatla, P. S., Morton, D. C., DeFries, R. S., Jin, Y., and van Leeuwen, T. T.: Global fire emissions and the contribution of deforestation, savanna, forest, agricultural, and peat fires (1997–2009), *Atmos. Chem. Phys.*, 10, 11707–11735, doi:10.5194/acp-10-11707-2010, 2010.

	ESA Climate Change Initiative (CCI)		Page 96
	Climate Assessment Report (CAR)		
	for the Essential Climate Variable (ECV) Greenhouse Gases (GHG)		Version 4 (final)
			28 March 2017

Wecht, K. J., D. J. Jacob, C. Frankenberg, Z. Jiang, and D. R. Blake (2014), Mapping of North American methane emissions with high spatial resolution by inversion of SCIAMACHY satellite data, *J. Geophys. Res. Atmos.*, 119, 7741–7756, doi:10.1002/2014JD021551.

Wunch, D., Toon, G. C., Blavier, J.-F., et al., The Total Carbon Column Observing Network, *Phil. Trans. R. Soc. A*, 369, 2087–2112, doi:10.1098/rsta.2010.0240, 2011.

Wunch, D., Wennberg, P. O., Toon, G. C. et al., A method for evaluating bias in global measurements of CO₂ total columns from space. *Atmos. Chem. Phys.*, 11, 12317–12337, 2011.

York, D., Evensen, N., Martinez, M., and Delgado, J.: Unified equations for the slope, intercept, and standard errors of the best straight line. *Am. J. Phys.*, 72(3), 367–375, 2004.

Yoshida, Y., Kikuchi, N., Morino, I., et al., Improvement of the retrieval algorithm for GOSAT SWIR XCO₂ and XCH₄ and their validation using TCCON data, *Atmos. Meas. Tech.*, 6, 1533–1547, doi:10.5194/amt-6-1533-2013, 2013.

END OF DOCUMENT